Growth and Characterization of Transition Metal Oxide Heterostructures with a Tailored Work Function

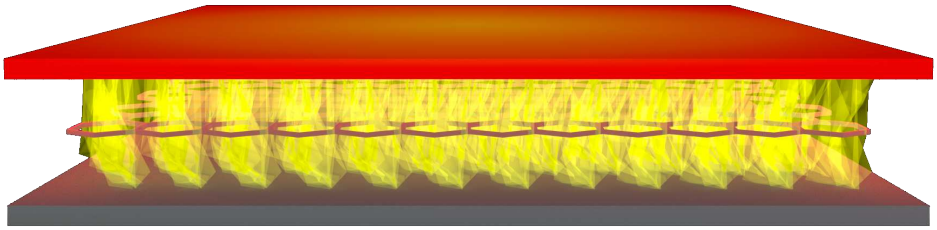

Ph. D. Thesis of

Iman Rastegar Alam

Department of Solid State Quantum Electronics

Max Planck Institute for Solid State Research, Stuttgart

2018

University of Stuttgart
Germany

Max Planck Institute
for Solid State Research

Growth and Characterization of Transition Metal Oxide Heterostructures with a Tailored Work Function

Von der Fakultät Mathematik und Physik der Universität Stuttgart
zur Erlangung der Würde eines Doktors der Naturwissenschaften
(Dr. rer. nat.) genehmigte Abhandlung

Vorgelegt von

Iman Rastegar Alam

aus Teheran, Iran

Hauptberichter: Prof. Dr. Jochen Mannhart
Mitberichter: Prof. Dr. Jörg Wrachtrup

Tag der mündlichen Prüfung: 09. Mai 2018

Vorsitzender der Prüfung: Prof. Dr. Hans Peter Büchler

Max-Planck-Institut für Festkörperforschung

2018

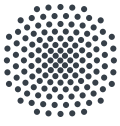

Universität Stuttgart
mathematik physik fakultät8

Max-Planck-Institut
für Festkörperforschung

For My Father

Contents

List of terms and abbreviations

AFM	Atomic force microscopy
CAD	Computer-aided design
CF flange	Conflat® flange
CNT	Carbon Nanotube
FWHM	Full width at half maximum of a Gaussian peak
HWHM	Half of the full-width at half maximum
ITO	Indium-Tin-Oxide
PETE	Photon-enhanced thermionic emission
PITE	Photon-induced thermionic emission
PLD	Pulsed laser deposition
Polycrys.	Polycrystalline material
RGA	Residual gas analysis
RGS	Residual gas spectrum
SEM	Scanning electron microscopy
SMU	Source-measure unit

STEM	Scanning transmission electron microscopy
TMO	Transition metal oxide
UHV	Ultra high vacuum

List of most used symbols

a	Lattice constant
A_{em}	Emission Area
A_{RD}	Richardson constant, $\approxeq 120.2\,\mathrm{A\,cm^{-2}\,K^{-2}}$
E_{vac}	Vacuum level energy
$\mathrm{e}V_{\Phi}$	Band-alignment voltage of the collector
$\mathrm{e}V_{\Delta\Phi}$	Band-alignment potential difference of two materials
I_{cl}	Collector current
I_{em}	Emitter current
I_{fil}	Filament current
I_{gr}	Grid current
J_{cl}	Current density of collector
J_{em}	Current density of emitter
J_{gr}	Current density of grid
k_{B}	Boltzmann constant, $\approxeq 8.617\,330\,3 \times 10^{-5}\,\mathrm{eV}$
λ	Wavelength of a light source
$\vec{\mu}$	Electrostatic dipole moment
μ_e	Bulk electrochemical potential
$\bar{\mu}_e$	Contribution of the bulk electrochemical potential to the work function
P_{fil}	Filament Power
ϕ_{surf}	Surface potential

T_{cl}	Temperature of collector
T_{em}	Temperature of emitter
V_{cl}	Potential applied to the collector
V_{em}	Potential applied to the emitter
V_{fil}	Filament voltage
V_{gr}	Potential applied to the grid
V^{int}	Applied voltage by an SMU to compensate the potential drop due to wiring resistance
V_{TC}	Thermocouple voltage
Φ_{WF}	Work function of a specific material
ϕ_{cl}	Work function of collector
ϕ_{em}	Work function of emitter
$\phi_{\mathrm{em}}^{\mathrm{eff}}$	Effective work function of the emitter
ϕ_{gr}	Work function of grid
w_{gr}	Grid mesh size
x	Position

Zusammenfassung

Die Austrittsarbeit ist eine fundamentale Materialeigenschaft, die eine große bedeutende Rolle in der Festkörperphysik spielt. Zum ersten Mal wurde das Wort "work function"(zu Deutsch: Austrittsarbeit) 1916 von Lester benutzt [1, 2], der damit die Energie beschrieb, die ein Elektron benötigt, um einen Festkörper zu verlassen. Die Austrittsarbeit spielt sowohl bei Oberflächeneffekten wie Katalyse und Elektronenemission als auch bei Grenzflächenphänomene eine wichtige Rolle. Materialien mit optimierter Austrittsarbeit sind deshalb erforderlich, um die Effizienz und die Funktionalität von oberflächen- und grenzflächenbasierten elektrischen Bauelementen zu verbessern.

Diese Arbeit beschäftigt sich mit der Messung von Austrittsarbeiten und zeigt, wie diese grundlegende Materialeigenschaft für verschiedene Anwendungen geziehlt verändert, bzw. optimiert werden kann. Dies wird mittels Heteroepitaxie dünnster Schichten demonstriert. Eine genaue Beschreibung der verwendeten Messmethoden und der Theorie zu Austrittsarbeiten ist in Kapitel 2 dargestellt.

Die Dünnschichtmaterialien in dieser Arbeit sind in einer Laserablationsanlage hergestellt und ihre Oberflächeneigenschaften *in-situ* in einer Ultrahochvakuumanlage untersucht worden. Diese Messanlage wurde im Rahmen dieser Arbeit entworfen und aufgebaut. Die Messmethode basiert auf dem Konzept eines thermoelektronischen Energiekonverters [3]. Solche Konverter ermöglichen

den verlustfreien Transport von thermionisch emittierten Elektronen von einer Kathode (Emitter) zu einer Anode (Kollektor). Ein positiv geladenes Gitter beschleunigt die emittierten Elektronen und verhindert so eine Raumladung. Somit erfahren die Elektronen nominell keine Änderung ihrer Energie, wenn sie den Kollektor erreichen. Um den Einfang von Elektronen durch das Gitter zu reduzieren, wird zusätzlich ein Magnetfeld parallel zur Elektronenbewegung angelegt. Die Messapparatur und ihre Eigenschaften sind in Kapitel 3 detailliert beschrieben.

Die Messgenauigkeit der Anlage und das Modell zur Datenanalyse wurden mit einer Serie von Blindversuchen überprüft. In diesen Versuchsreihen wurden Austrittsarbeiten verschiedener Materialien, die dem Experimentator unbekannt waren, bestimmt. Anschließend erfolgte der Vergleich mit Werten aus der Literatur. Die Resultate der Blindversuche (Molybdän und Platin) sowie die Messungen an einkristallinem Nb:$SrTiO_3$ und einer LaB_6 Dünnschicht ergaben eine Messgenauigkeit von weniger als 100 meV im Vergleich zu Literaturwerten.

Derzeit sind die Austrittsarbeiten von Übergangsmetalloxiden noch wenig erforscht. Die Austrittsarbeit von ABO_3-Perowskiten wird in dieser Arbeit beispielhaft an $SrRuO_3$ Dünnschichten, welche epitaktisch auf Nb:$SrTiO_3$ gewachsen wurden, untersucht. Die Ergebnisse sind in Kapitel 4 zusammengefasst und zeigen, dass die Austrittsarbeiten dieser Materialien stark temperaturabhängig sind. Desweiteren konnte gezeigt werden, dass durch Oberflächenrelaxation die Austrittsarbeit von $SrRuO_3$ Dünnschichten um etwa 17 % reduziert werden kann.

Das Kernthema dieser Arbeit ist die gezielte Veränderung der Austrittsarbeiten, insbesondere von Perowskiten, durch Heteroepitaxie. Kapitel 4.4 beschreibt die Veränderung der Austrittsarbeit von $SrRuO_3$ durch vier verschiedene epitaktisch gewachsene Monolagen. Diese Monolagen sind $BaTiO_3$, $SrTiO_3$, $LaAlO_3$, und $BaZrO_3$. Die Ablationsparameter dieser Deckschichten wurden möglichst gleich gehalten um qualitativ vergleichbare Ergebnisse zu bekommen. Dafür wurde der Sauerstoffhintergrunddruck während des Wachstums von $SrRuO_3$ Dünnschichten und den darauffolgenden Deckschichten

gleich gehalten, da $SrRuO_3$ sehr empfindlich auf die Änderung dieses Parameters reagiert. Zusätzlich wurde die Wachstumstemperatur für die Monolagen gleich gehalten. Lediglich die Fluenz des Ablationslasers wurde auf die epitaktischen Wachstumsbedingungen abgestimmt und optimiert. Somit konnte sichergestellt werden, dass die Monolagen unter denselben Bedingungen auf $SrRuO_3$ Dünnschichten gewachsen wurden.

Die Austrittsarbeit von $SrRuO_3$ wurde durch $BaTiO_3$ und $SrTiO_3$ Monolagen verringert und durch $BaZrO_3$ und $LaAlO_3$ erhöht. Die größte Veränderung wurde durch eine Monolage $LaAlO_3$ erreicht; sie beträgt $+7.4\,\%$ im relaxierten und $+23\,\%$ im unrelaxierten Zustand. Diese Erkenntnisse können genutzt werden um für Anwendungen gezielt geforderte Austrittsarbeiten an Grenz- oder Oberflächen einzustellen.

Die Ergebnisse der gewachsenen Monolagen auf $SrRuO_3$ Dünnschichten zeigen, dass die Austrittsarbeit von Perowskiten, sowie ihre Modifikation, stark von dem *B*-Atom der letzten Atomlage abhängt. Dies wird durch den Vergleich der Ergebnisse der verschiedenen Deckschichten deutlich. Die $BaTiO_3$ und $SrTiO_3$ Deckschichten reduzieren beide die Austrittsarbeit von $SrRuO_3$, wohingegen die $BaZrO_3$ Schicht diese erhöht. Da $BaTiO_3$ und $SrTiO_3$ das gleiche Übergangsmetall auf ihrer *B*-Seite haben und $BaTiO_3$ und $BaZrO_3$ das gleiche *A*-Ion, deuten die Ergebnisse auf eine BO_2-Terminierung für diese Heterostrukturen hin. Diese Beobachtung ist in Übereinstimmung mit den Ergebnissen der unbeschichteten $SrRuO_3$ Dünnschichten, deren Messergebnisse auch auf eine BO_2-Terminierung hindeuten.

Die Messungen der $BaTiO_3$ und $SrTiO_3$ Monolagen auf $SrRuO_3$ Dünnschichten deuten auf eine unvollständige Oberflächenabdeckung hin. Dieses Ergebnis ist überraschend, da mit RHEED kein Hinweis darauf möglich war. Dies wurde durch STEM-Aufnahmen von mehreren Monolagen $BaTiO_3$ auf $SrRuO_3$ bestätigt. Die Bilder zeigen Inselwachstum der $BaTiO_3$ Schicht auf der $SrRuO_3$ Dünnschicht, die dem Wachstumsmodus von Stranski-Krastanov zu folgen scheint. Dies überrascht, da die Gitterfehlanpassung von $BaTiO_3$ zu $SrRuO_3$ $1.7\,\%$ beträgt und von $LaAlO_3$ zu $SrRuO_3$ $4\,\%$, obwohl welche Ergebnisse auf eine geschlossene Monolage hindeuten. Diese Übereinstimmung zwischen den

Ergebnissen der Austrittsarbeitmessungen und den STEM-Bildern zeigt, dass diese Messungen der Austrittsarbei qualitative und detaillierte Informationen über die Oberflächenstruktur liefern, die mit anderen Charakterisierungsmethoden wie RHEED schwer erreicht werden können.

Schließlich wird in Kapitel 5 dieser Arbeit die durch Photonen induzierte thermionische Emission (PITE) an Kohlenstoffnanoröhren untersucht. Eines der Probleme mit solchen Strukturen ist die Verringerung des Emissionsstroms mit der Zeit. In dieser Arbeit konnte gezeigt werden, dass dies mit den hohen Temperaturen der sogenannten Wärmefallen ("Heat-Traps") zusammenhängt. Diese führen zu Sublimation und Veränderung der Kohlenstoffnanostrukturen und damit zu einer verringerten Emission. Es konnte zusätzlich experimentell demonstriert werden, dass PITE mit thermoelektronischen Konvertern kompatibel ist und dadurch die Raumladung unterdrückt wird. Diese Untersuchungen sind für die Realisierung effizienter PITE Energieumwandler wichtig.

Chapter 1

Introduction

The history of thermionic emission and the concept of the work-function barrier are bound together. The term "work function" was, apparently, first used by Lester in 1916 to describe the constant in the exponent of the first Richardson equation [1, 2]. However, the search for materials with a low work function had started since the very beginning of the 20th century. Wehnelt reported on the emission enhancement of platinum by coating it with BaO and CaO layers in 1904 [4, 5]. His observation gave rise to oxide cathodes that could operate at lower temperatures and demonstrate higher current densities than refractory metals. These cathodes revolutionized cathode-ray-tube (CRT) technologies, and are still the cathode of choice in these devices today [5, 6].

The investigations of Lang and Kohn provide our current understanding of the work function and its characteristics. They employed density-functional-theory (DFT) to calculate the surface states and charge density at several metal surfaces [7, 8]. Their pioneering work explained not only the anisotropic nature of the work function, but also provided the basis for the qualitative work-function calculations performed today. Recent calculations explain the work function enhancement in oxide cathodes by the modification of the surface dipoles induced by the dielectric layer [9, 10, 11]. Interestingly, these calculations suggest that just one monolayer of a dielectric coating can drastically increase or decrease the work function of metals.

The work function is not limited to vacuum electronics in today's science. This energy barrier is an essential material property for various applications, such as catalytic processes [12], solid-state devices [13], and thermionic energy converters [3, 14, 15, 16]. For instance, the work function determines the efficiency of thermionic energy converters, and the Schottky barrier height at the interface of a metal-semiconductor junction, *e.g.*, in photovoltaic devices. Hence, materials with optimized work functions are needed to further enhance these processes and devices.

The recent advances in deposition techniques and heteroepitaxy open new opportunities for materials and compounds with "*tailored*" and optimized work functions. Deposition techniques such as pulsed laser deposition (PLD) can be used with atomic precision to obtain heterostructures with new functionalities at surfaces or interfaces. Susaki *et al.*, have shown that the deposition of a single unit cell of MgO on an Nb:$SrTiO_3$ substrate reduces the work function by about 0.8 eV [17]. This tailoring of the work function has also been recently employed for adjusting the Schottky barrier height at the interfaces of oxide heterostructures [18].

This thesis investigates the work function of transition metal oxides (TMO) and explores the tunability of their work function by heteroepitaxy. This investigation is important because the work function of these materials has not yet been extensively explored. Moreover, correlated materials, such as many of the ABO_3 perovskites and their heterostructures, demonstrate unique physical properties that are promising for future electronic devices [19, 20, 21, 22].

This investigation is pursued using epitaxially grown $SrRuO_3$ thin films as a model material. These films are grown by PLD on Nb:$SrTiO_3$ substrates. The tunability of its work function is explored by capping layers of $SrTiO_3$, $BaTiO_3$, or $BaZrO_3$ with thickness of one-unit-cell, all grown epitaxially. These capping layers are chosen to substitute the atomic layers on the surface, *i.e.*, exchanging the A-atom and B-atom separately in this ABO_3 perovskite. Additionally, the effect of a polar capping layer is investigated using a one-unit-cell thick layer of $LaAlO_3$, *i.e.*, the fourth employed layer throughout this work. These investigations can provide an understanding of the complex science at the surface, as well as at the interface of these materials.

The measurements presented in this thesis are performed *in-situ* in a custom-built ultra-high-vacuum system, which is based on the concept of thermoelectronic converters [3, 23]. These converters realize the space-charge free transport of electrons, and demonstrate the characteristics of an ideal vacuum diode. Consequently, the energy levels are well defined, which allows the extraction of work-function values from their current-voltage characteristics. Hence, the measurements are performed on large surface areas and at elevated temperatures, *i.e.*, at the operating condition of thermionic devices. The *in-situ* determination of the work function is vital in this work, as impurities and contaminants on the surface will modify the surface dipoles and deceive the experimental findings.

Outline

Chapter 2 addresses two central parts of this thesis. First, it provides a detailed description of the work function and discusses how a dielectric coating can alter it. Second, it examines and formulates the current-voltage characteristics of thermoelectronic converters, and shows how work-function values can be extracted from them. The chapter closes by demonstrating a measurement example of a material having two different work functions.

The experimental bases and technical descriptions of the techniques performed in this thesis are discussed in Ch. 3. This chapter provides an overview of the epitaxial growth system and the techniques used for sample fabrication. Further, it demonstrates the measurement apparatus and its components, and presents its characteristics. This chapter closes by reporting proof-of-concept measurements performed on a series of blind tests, which demonstrate a measurement accuracy of $<100\,\mathrm{meV}$.

Chapter 4 presents the experimental findings on novel material systems. These start with LaB_6 thin films prepared by PLD and continue with the ABO_3 perovskites and their fabricated heterostructures. The results show that a single monolayer of a dielectric can either increase or decrease work functions. Moreover, they suggest that other mechanisms, such as surface relaxation or distortion may alter work functions by up to 1 eV. These

results are in good agreement with model calculations and demonstrate the complexity of the work function in TMO.

Chapter 5 investigates the photon induced thermionic emission (PITE) of carbon-nanotube forests. First, their emission characteristics are examined, and possible reasons for the observed current decay of these devices are provided. Moreover, it illustrates the compatibility of PITE with the concept of thermoelectronic converters for space-charge suppression. This chapter closes with an outlook on solar PITE devices and discusses the challenges to realize such converters.

Chapter 6 provides a summary and conclusion of the experimental findings.

Chapter 2

Background Knowledge and Measurement Concept

This chapter focuses on the definition of the work function, how a coating layer can alter it, and moreover discusses the complexity of this material property in transition metal oxides. This discussion is highly influenced by the book of Hölzl and Schulte [24] that provides a detailed look at this matter. The second section focuses on the measurement concept and the $I(V)$ characteristics of thermoelectronic converters, and demonstrates how work function values can be extracted from these characteristics. At the end, an example measurement is provided for the work-function determination of a platinum coating on a bulk molybdenum sample.

2.1 Work Function

The physics of electron emission is governed by the fundamental material property, the work function. This material property is usually oversimplified and defined as "The minimum energy required to extract one electron from the electrochemical potential of a material, to the vacuum level."[24, 25] The energy of the vacuum level (E_{vac}) is defined as the energy of an electron at rest, at a distance where the image charge of the bulk is negligible. However, this distance needs to be small such that the surface energy barriers (E_{surf}) of the different crystal facets can be distinguished (see Ch. 2 in Ref. [24]). The definition of the work function mentioned above seems to be insufficient to explain the observed anisotropic characteristics of the work function [24, 26]. Throughout this thesis, the work function is specified in the following manner:

> The energy required to remove one electron with an energy of the electrochemical potential, through a well-defined and uniform surface to the vacuum level.

This definition of the work function emphasizes that the work function of a material highly depends on the surface from which an electron is removed. This anisotropy results from the possibly different surface dipoles emerging at the different crystal facets as the atomic distances change in different crystal orientations (see Fig. 2.1b). Moreover, this definition differentiates the contribution of the bulk properties (electrochemical potential, μ_{e}), with the surface energies (E_{surf}) resulting from the surface dipoles. Thus, the work function should be considered in the following way:

$$\Phi_{\text{WF}} = E_{\text{vac}} - (E_{\text{surf}} + \bar{\mu}_e), \tag{2.1}$$

where E_{vac} is the vacuum level potential, E_{surf} the surface potentials at a specific surface, and $\bar{\mu}_e$ the contribution of μ_e to the work function. Figure 2.1a illustrates the potential levels in a solid for an electron leaving the bulk. The electric dipoles resulting from the image charge at the different crystal

facets can drastically change E_{surf} and thus the work function of a material. Nieuwenhuys *et al.* have investigated the various facets of platinum and report on a work function anisotropy of more than 0.5 eV [27]. Table 2.1 compares some of the reported work function values for the different crystal facets of platinum found in the literature.

The dipole layers on the surface of a metal can be modified to alter and tune its work function. Indeed, it has been reported that dielectric coatings can change the electron emission behavior of metals. The change of the work function in oxide coated, or impregnated cathodes have been investigated since the early studies of thermionic emission, as J. P. Blewett reviewed the effect of BaO and SrO coatings on tungsten in 1939 [35]. Recently, it has been reported that the combination of BaO with Sc_2O_3 can reduce the work function of tungsten ($\Phi_{\text{WF}}^{\text{Polycr.–W}} \approx 4.55\,\text{eV}$, [33]) to values as low as 1.32 eV in a dispenser cathode [11]. Separately, current densities as high as $1\,\text{A}\,\text{cm}^{-2}$ at a temperature of about 1290 K have been reported for such cathodes [36]. Although most reports are focused on work function reduction, not all dielectric layers would necessarily reduce the work function of a metal.

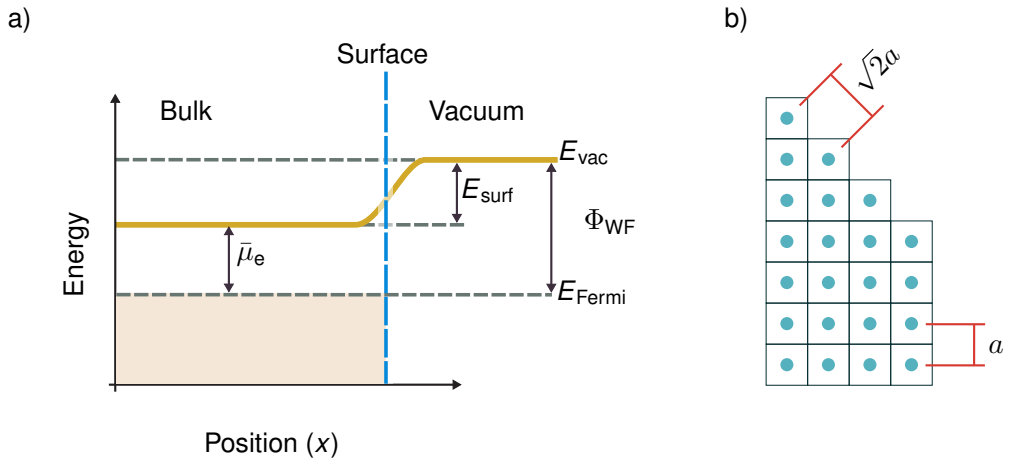

Figure 2.1: Schematic of a) energy levels close to the metal surface for defining the work function after Ref. [28], and b) different facets of a single crystal metal after Ref. [26]. The anisotropy of the work function results from the different surface dipoles emerging on the different crystal facets that consequently alter E_{surf} and result in a different work function. Note that in panel a) $\mu_e = E_{\text{Fermi}}$.

Table 2.1: Some of the reported work function values of several facets of platinum crystals and polycrystalline samples.

Crystal orientation	$\Phi_{\mathrm{WF}}^{\mathrm{Pt}}$ (eV)	Measurement method	Ref.
(111)	5.93	Field emission	[27]
	6.08 ± 0.15	Photoemission	[29]
	5.69	Model calculation	[30]
(100)	5.84	Field emission	[27]
	5.82 ± 0.15	Photoemission	[29]
	5.66	Model calculation	[30]
(110)	5.35 ± 0.05	Field emission	[31]
	5.26	Model calculation	[30]
(320)	5.22	Field emission	[27]
(331)	5.12	Field emission	[27]
Polycrystalline	5.32	Photoemission	[27]
	5.64	Photoemission	[32]
	5.65	Photoemission	[33]
	5.8	Thermionic	[34]

Density functional theory (DFT) model calculations suggest that a single monolayer of TiO_2 can increase the work function of Mo (100) by about 0.76 eV [9]. Model calculations explain the change of the work function by a dielectric coating by the change of the surface dipoles that consequently alters E_{surf} of the metal. This change can result from the charge transfer at the interface (ϕ^{CT}), electrostatic compressive effects (ϕ^{Comp}), and surface relaxations of both the metal and the dielectric (ϕ^{SR}). Thus, the work function change of a metal by a dielectric coating can be written as [10]:

$$\Delta\Phi_{\mathrm{WF}} = \Delta\phi^{\mathrm{CT}} + \Delta\phi^{\mathrm{Comp}} + \Delta\phi^{\mathrm{SR}}. \tag{2.2}$$

A schematic visualization of the effects of $\Delta\phi^{\mathrm{CT}}$ and $\Delta\phi^{\mathrm{Comp}}$ induced by a dielectric layer on the work function of a metal is illustrated in Fig. 2.2. Although the discussion here is mainly focused on the surface properties, this outcome has also been reported for Schottky barrier heights, as the barrier height is increased by the insertion of a polar dielectric layer at the interface of a metal-insulator junction [18]. The work function of pure metals has been extensively investigated in the past, and the effects of dielectric coatings have been widely reported. For novel materials, work functions have only been explored marginally, however.

The work function of correlated material systems such as the transition-metal oxides (TMO) and heterostructures have not been adequately studied, according to the literature. According to model calculations for the cubic perovskites (ABO_3) [37, 38], these materials offer a broad range of work function values. Figure 2.3a shows a sketch of a cubic ABO_3 perovskite unit cell. Considering a (001) crystal direction, these compounds consist of stacked layers of an AO, and BO_2 oxide layers, in which A and B are both metal ions. The last oxide layer on the surface defines the termination of the material that can alter both the surface and the interface properties of these materials and their heterostructures, respectively [17, 39]. These calculations suggest that in a BO_2 terminated crystal just by altering the transition metal on the B site, the work function can drastically change. For example, by exchanging

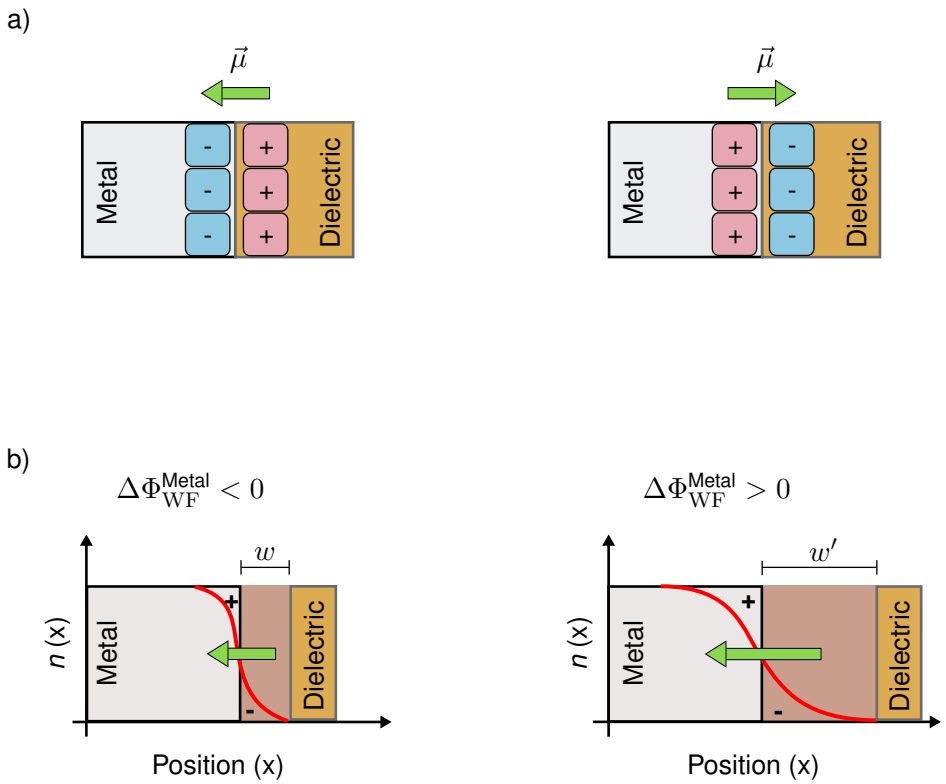

Figure 2.2: Schematic showing how a dielectric layer can affect the work function of a metal ($\Phi_{\mathrm{WF}}^{\mathrm{Metal}}$). Panel a) shows two different cases for the charge transfer in a metal-dielectric junction. Depending on the density-of-states and the band-alignments of the dielectric and metal, the charge transfer results in a modified surface dipole at the metal surface that modifies E_{surf} and consequently $\Phi_{\mathrm{WF}}^{\mathrm{Metal}}$. The electric dipole ($\vec{\mu}$, shown in green) on the left reduces $\Phi_{\mathrm{WF}}^{\mathrm{Metal}}$, and on the right increases it. Panel b) shows how $\Phi_{\mathrm{WF}}^{\mathrm{Metal}}$ changes depending on the interface distance between a metal and a dielectric coating layer. Left, the dielectric layer compresses the electron density profile (n(x), red line) at the metal surface ($\Delta\Phi_{\mathrm{WF}}^{\mathrm{Metal}} < 0$). On the right side, the large interface distance extends n(x) that results in a larger surface dipole ($\Delta\Phi_{\mathrm{WF}}^{\mathrm{Metal}} > 0$). For instance, the calculated charge transfer for BaO and MgO on Au is found to be similar, but their interface distance with Au results in 2.59 Å and 2.73 Å, respectively [10]. Consequently, $\Delta\Phi_{\mathrm{WF}}^{\mathrm{Au}}$ is computed to be -2.8 eV for the BaO, and -1.6 eV for the MgO capping layers, respectively [9, 10]. The "+" sign represents the image charge. Figures from Ref. [10] with permission.

the Ti atom with Ru in $SrBO_3$, the work function increases by about 0.5 eV (see Fig. 2.3b). Moreover, the work functions of these materials strongly depend on their termination. Interestingly, these calculation imply that all AO-terminated perovskites lead to a lower work function when compared to their BO_2-terminated surface. This difference might result from the fact that the AO layer on top acts similar to a dielectric coating layer as previously discussed, and has been so far experimentally observed for $SrTiO_3$ [17]. Figure 2.3b presents the results of the model calculations of Z. Zhong and P. Hansmann for $SrBO_3$ materials.

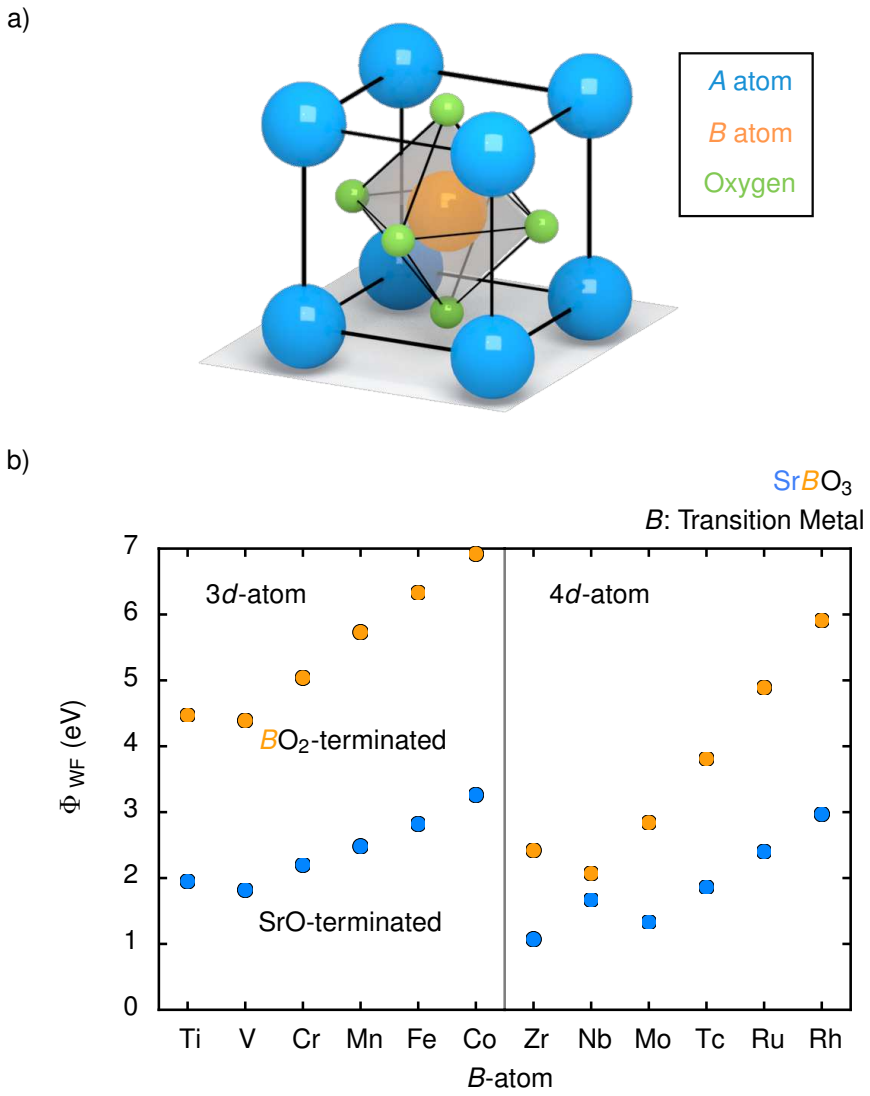

Figure 2.3: a) Schematic of a cubic ABO_3 perovskite unit cell. The A-atom is located at the corners and the B-atom is at the center. The oxygen atoms form an octahedron enclosing the transition metal at the center. The atomic sizes and distances are arbitrary and do not represent physical values. b) DFT calculations of the work function for strontium based perovskites, $SrBO_3$ (001), reproduced from Ref. [37] with permission. The panels compare the various work function values for the different $3d$-metal atoms (left), and $4d$-metals (right). The data points in orange are computed values for the BO_2 termination, and in blue for the SrO termination.

2.2 Measurement Concept and Data Analysis Method

The work function measurements in this work have been conducted using a thermoelectronic converter [3] by the retarding potential method [24, 40, 41]. In this method, the sample material is used as collector (anode) in a vacuum diode or triode and its work function is determined with respect to the work function of the emitter, or an additional reference material. In the following discussion, we examine this method by the $I(V)$ characteristics of an ideal space-charge free vacuum diode, based on Ref. [1, 14, 40, 41]. Hence, we assume an infinite wide planes for the emitter and collector and that the electrons are ballistically transported to the collector material without their energy being altered. In this ideal case, phenomena such as the reflection of the electrons from the collector surface, or electron emission from the collector (back emission) are neglected. Afterwards, the discussion is extended to thermoelectronic converters, as these devices realize space-charge free conditions. This section closes with the demonstration of a measurement example, in which the investigated sample has two different work functions.

The characteristics of thermionic-based devices are dictated by the emission properties of their emitter. Thermionic emission is a process in which the electrons are thermally excited to overcome the emitter work function barrier at the surface. The Richardson-Dushman equation defines the saturation current density of a thermionic emitter as [42, 43]:

$$J_{\mathrm{em}} = A_{\mathrm{RD}} \cdot T_{\mathrm{em}}^2 \cdot \exp(-\frac{\phi_{\mathrm{em}}}{k_{\mathrm{B}} T_{\mathrm{em}}}), \tag{2.3}$$

where T_{em} is the temperature of the emitter, k_{B} the Boltzmann constant, ϕ_{em} the emitter work function in electron volts, and A_{RD} the Richardson constant which equals:

$$A_{\mathrm{RD}} = \frac{4\,\pi\, m_{\mathrm{e}}\, k_{\mathrm{B}}^2\, e}{h^3} \approxeq 120.2\,\frac{\mathrm{A}}{\mathrm{K}^2\,\mathrm{cm}^2}, \tag{2.4}$$

with h being the Planck constant, m_e the electron mass, and e the electric charge. Equation 2.3 results from the fact that at elevated temperatures the Fermi distribution function can be approximated by Boltzmann statistics. Thus, the current will increase exponentially as either the work function of the emitter decreases or the temperature rises. In numerous reports, the pre-exponential factor has been found to vary from the derived Richardson constant and correction factors have been suggested to be included in Eq. 2.3 [1, 40]. This deviation is attributed to a non-uniform metal surface, and the applied electric fields to obtain a saturation current [1]. Shelton suggested that these deviations originate from the measurement geometry used to determine the emission constants [44]. Anywise, the emission constants of the emitter remain the essential characteristics of a thermionic device, as they determine the operating temperature and the saturation current. Similar to Eq. 2.3, the current of the collector depends on its work function, but additionally on the applied collector potential (eV_{cl}). The collector current in an ideal, space-charge free vacuum diode with a uniform emitter and collector surface can be characterized as [14, 41]:

$$J_{cl} = \begin{cases} 0 & : \quad \phi_{em} \ll eV_{cl} + \phi_{cl} \\ A_{cl} \cdot T_{em}^2 \cdot \exp\left(-\frac{\phi_{cl}+eV_{cl}}{k_B\, T_{em}}\right) & : \phi_{em} \leq eV_{cl} + \phi_{cl} \leq \phi_{em} + \phi_{cl} \\ J_{em}^{sat} & : \quad eV_{cl} + \phi_{cl} < \phi_{em} \end{cases} \tag{2.5}$$

where ϕ_{cl} is the collector work function and eV_{cl} the potential applied to the collector both in electron volts, A_{cl} a geometrical factor of the collector with the same unit as A_{RD}, and $J_{em}^{sat.}$ the effective saturation current density of the emitter. If the barrier at the collector is so high, that the emitted electrons do not find available states, no current will flow into the collector (retarding regime). As the applied potential starts to align the vacuum levels of the emitter and collector, the current increases exponentially (accelerating regime), and saturates when these energy levels have been fully aligned (saturation regime). Figure 2.4 illustrates the different cases of Eq. 2.5 in an ideal space-charge free vacuum diode. Note that in Eq. 2.5 high potentials that could lead

in other emission types, such as Schottky or field emission behavior of the emitter are neglected. Thus, the potential required for aligning the vacuum levels of the emitter and collector corresponds to the work function difference of these materials. Nevertheless, in thermionic-based energy converters, this potential is referred as the maximum output voltage ($eV_{\mathrm{load}} = \phi_{\mathrm{em}} - \phi_{\mathrm{cl}}$) [23].

As a result, the work function of the collector can be determined by the electric potential needed to obtain a saturation current from an emitter with a known work function. The onset potential at which the collector current starts to increase exponentially or enters the saturation regime is found not to be as sharp as Eq. 2.5 suggests. This uncertainty results from the tail of the Fermi function at elevated temperatures that results in a not well-defined energy of the emitted electrons. Additionally, if the surface of the emitter or collector is not uniform and well defined, this transition point would become even more unclear. For example, at high emitter temperatures the work functions of the different facets of a polycrystalline silver sample might be indistinguishable as a collector, as the anisotropy of the (100) and (110) facets is 80 meV [45]. Consequently, Eq. 2.5 can be extended to the case in which the collector surface has different work functions, *i.e.*, materials or facets where the band alignment for each material occurs at a separate collector voltage (eV_{Φ}). Based on the previous discussion, the collector current can be generalized for a collector consisting of a surface with n different work functions by:

$$J_{\mathrm{cl}}^{\mathrm{sat}} = \sum_{i=1}^{n} A_i \cdot T_{\mathrm{em}}^2 \cdot \exp\left(-\frac{\phi_{\mathrm{cl}}^i + eV_{\Phi}^i}{k_{\mathrm{B}}\, T_{\mathrm{em}}}\right) \tag{2.6}$$

where eV_{Φ}^i is the minimum potential required for the band alignment of the area proportional to A_i of the collector surface, with a work function of ϕ_{cl}^i. Indeed Eq. 2.6 requires that the work function differences of the collector lie sufficiently far apart from each other, such that the previously discussed uncertainty of the experiments is less than the work function differences. Since the work function measurements are performed on large surface areas, this allows one to determine the surface potentials of the entire surface qualitatively. So far, the discussion was based on an ideal vacuum diode, with

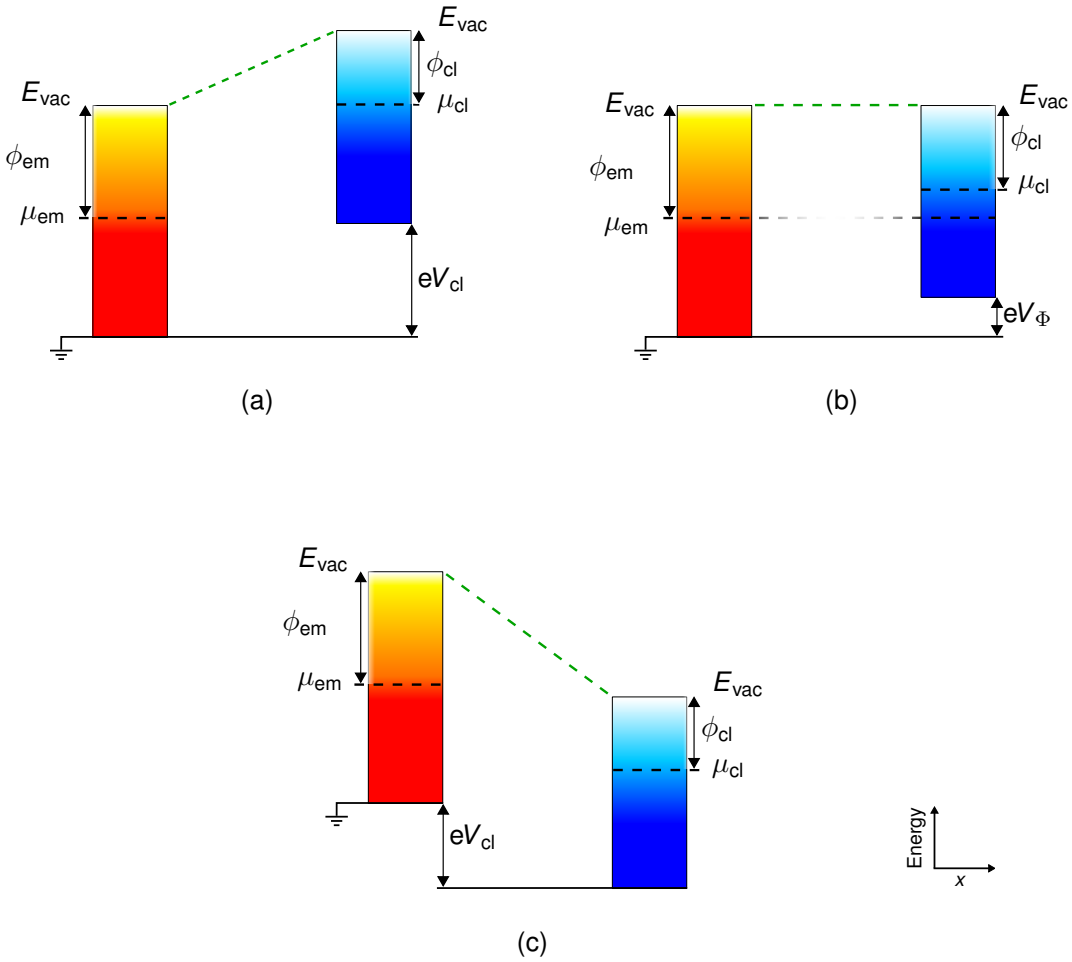

Figure 2.4: Schematic visualization of the different cases of Eq. 2.5, for an ideal, space-charge free vacuum diode assuming $\phi_{\mathrm{em}} > \phi_{\mathrm{cl}}$. In panel (a) The potential applied to the collector does not allow a current to flow and the device is in the retarding regime ($J_{\mathrm{cl}} = 0$). From panel (a) to (b), the current increases exponentially as the vacuum levels align at $eV_{\Phi} = \Delta\phi$, and (c) saturates afterwards. In all panels, the emitter is kept on the reference potential ($eV_{\mathrm{em}} = \mathrm{Ground}$).

the energy of the electrons being not altered. However, in experiments, such a condition is hardly achieved as sub-1 µm distance between the electrodes is required for a space-charge free emission [46, 47].

Thermoelectronic converters are a particular case of vacuum triodes, in which the space charge is suppressed and the energy of the emitted and arriving electrons are similar. In these devices, thermally excited electrons are accelerated by a positively charged grid to move to the collector surface. Furthermore, a magnetic field is applied perpendicular to the emission surface that reduces the electron absorption by the grid and keeps them on straight trajectories. Therefore, the accelerated electrons will decelerate after passing through the grid and reach their initial energy. Figure 2.5 shows the schematic band-diagram of thermoelectronic converters. As a consequence, the space charge is suppressed, and ideally, the electrons arrive with the same energy as they were emitted at the collector surface. Hence, the current-voltage characteristics of these devices follow the ideal case of a vacuum diode described so far, but by considering the electron absorption of the grid. Similar to Eq. 2.6, the emitter current in a thermoelectronic converter with a uniform emitter and grid surfaces can be written in the following way:

$$J_{\mathrm{em}}^{\mathrm{sat}} = \overbrace{\sum_{i=1}^{n} A_i \cdot T_{\mathrm{em}}^2 \cdot \exp\left(-\frac{\phi_{\mathrm{cl}}^i + eV_{\Phi}^i}{k_{\mathrm{B}}\, T_{\mathrm{em}}}\right)}^{J^{\dagger}_{\text{em-cl}}} + \overbrace{A_{\mathrm{gr}} \cdot T_{\mathrm{em}}^2 \cdot \exp\left(-\frac{\phi_{\mathrm{gr}} + eV_{\mathrm{gr}}}{k_{\mathrm{B}}\, T_{\mathrm{em}}}\right)}^{J^{\dagger}_{\text{em-gr}}} \quad (2.7)$$

with $J^{\dagger}_{\text{em-}}$ being the effective saturation current density of the collector or grid, ϕ_{gr} the grid work function in electron volts, and eV_{gr} the minimum grid potential needed to suppress the space-charge and align its vacuum level with respect to the emitter. Here again, potentials that could lead to other emission types are neglected. Thus, the different work functions of a collector surface can be measured in these devices, similar to an ideal vacuum diode.

It follows from Eq. 2.6 and 2.7 that a reference material with a known work function can be incorporated on the collector surface for calibrating the measurements. Hence, by using such a technique the unknown part of

the collector work function can be determined from the potential difference between the band-alignment voltages of the known and unknown parts of the collector ($eV_{\Delta\Phi}$). This method is advantageous as it does not rely on the emitter characteristics and can be used independently. In the discussion below, we will demonstrate an experiment for the work function determination of an evaporated platinum thin film independently from the emitter characteristics. This thin film is evaporated on a bulk molybdenum sample and is partially covering its surface.

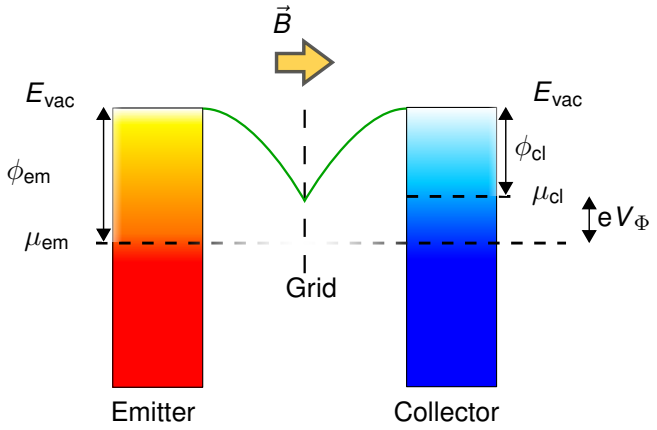

Figure 2.5: Sketch of the working principle of thermoelectronic converters. The emitted electrons are accelerated towards the collector (blue) by the grid. After the electrons pass through the grid, they are decelerated and reach their initial energy at the surface of the collector. The green line depicts the potential line of the electrons.

Figure 2.6 shows the $I_{cl}(V_{cl})$ curves of a polycrystalline molybdenum sample, with its surface being partially coated with platinum. Here, the collector current exhibits the previously discussed behavior, from the retarding regime to the saturation regime by varying the applied potential with respect to the emitter. However, the accelerating regime consists of two independent parts, as the logarithmic and the differential conductance plots indicate (Fig. 2.6b and 2.6c). The difference of the potential needed for the band alignments of these two materials ($eV_{\Delta\Phi}$), can either be extracted from a linear approximation of the Log-plot, or by the peak analysis of the dI_{cl}/dV_{cl} curve. In this example, both methods exhibit the same result, indicating a

work function difference of $eV_{\Delta\Phi} = 0.65\,\mathrm{eV}$ between the molybdenum and the platinum coating of the collector surface. As the work function of this particular molybdenum sample was determined to be 4.59 eV (see Sec. 3.3), the work function measurement of this platinum coating results in $\Phi_{\mathrm{WF}}^{\mathrm{Pt}} = 5.24\,\mathrm{eV}$. This value is in good agreement with the reported values for polycrystalline platinum (see table 2.1).

As shown above, the work function differences between the various collector materials ($eV_{\Delta\Phi}$) follow from both the logarithmic plot and the differential-conductance analysis to the same value. Although in both methods their differences coincide, the individual values for the band alignment of each material (eV_{Φ}), are underestimated from the peak of the $\mathrm{d}I_{\mathrm{cl}} / \mathrm{d}V_{\mathrm{cl}}$ curve. As discussed before, this is because of the unsharp transition from the accelerating regime to the saturation regime. As the linear approximation of the logarithmic plot considers such a transition, it is used for work function determinations concerning an emitter with a known work function ($eV_{\Phi} = \phi_{\mathrm{em}} - \phi_{\mathrm{cl}}$).[1]

Such a calibration technique can be essential, as the effective work function of the emitter might deviate from its actual value in experiments due to space-charge effects, or change over time as the emitting material degrades at the elevated temperatures. Furthermore, this method provides additional information for characterizing materials, whose work function has not been reported in the literature so far. In this work, a platinum stripe is evaporated *in-situ* on the surface of the samples to have a reference material for the work function determination of such materials. The noble properties of platinum, such as being chemically resistant, having a high melting temperature, and more importantly not forming an oxide layer are essential properties that make it a useful reference material. Additionally, the work function of the different facets of platinum are widely investigated, which makes it a reliable reference material to verify the outcome of the experiments.

[1] The band-alignment voltage can also be determined from the $\mathrm{d}I_{\mathrm{cl}} / \mathrm{d}V_{\mathrm{cl}}$ curves, by $eV_{\Phi} = x_{\mathrm{c}} + \frac{\mathrm{HWHM}}{2}$, with x_{c} being the position of the peak, which is also the lower limit of the work function. Consequently, $x_{\mathrm{c}} + \frac{\mathrm{FWHM}}{2}$ is the upper limit. However, this method is not actively practiced in this thesis.

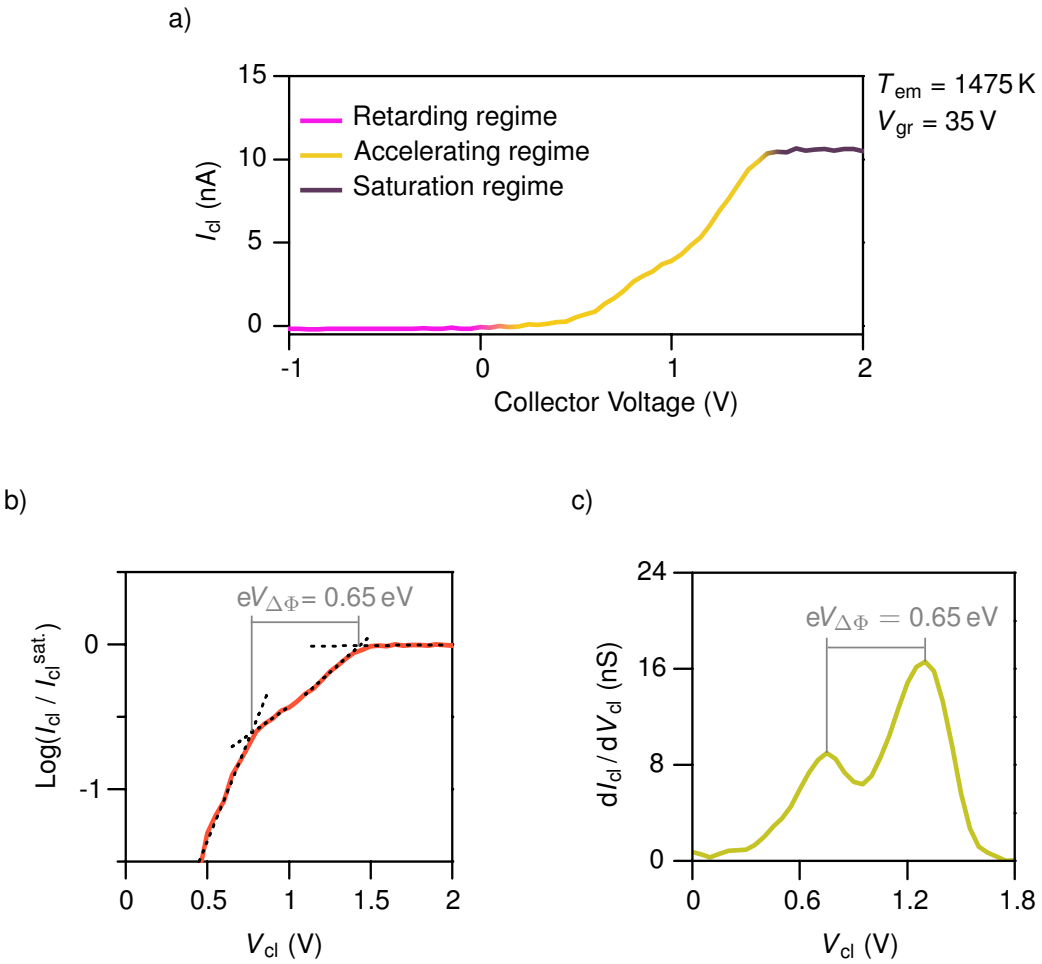

Figure 2.6: Work function determination of an *in-situ* evaporated platinum thin film, partially covering a polycrystalline molybdenum bulk sample ($\Phi_{\mathrm{WF}}^{\mathrm{Mo}} = 4.59\,\mathrm{eV}$, see Sec. 3.3). Panel a) shows the obtained $I_{\mathrm{cl}}(V_{\mathrm{cl}})$ curve that follows Eq. 2.5, with the different regimes being labeled. The band-alignment voltage difference from both b) the logarithmic-plot and c) the differential conductance plot of the $I_{\mathrm{cl}}(V_{\mathrm{cl}})$ curve results in 0.65 eV. Emitter and grid currents are not shown for clarity.

Chapter 3

Design of the Experimental Setup and System Characteristics

This chapter provides a brief overview of the epitaxial system and the thin film deposition technique used in this work, followed by a more in-detail look at the custom-built measurement apparatus which was designed and constructed to carry out the experimental goals. The measurement apparatus is based on the concept of thermoelectronic conversion [3, 23] and optimized for precise work function measurements performed *in-situ*. A full description of the complete technical details is beyond the scope of this writing, and here we mainly address the most important aspects of the design. These aspects are the concept of *in-situ* sample loading while ensuring a parallel plane configuration, the design of the sample holder, the magnetic yoke, and the heating mechanism which has achieved temperatures of more than 1950 K. Special care was taken to make the system compatible with photon enhanced and photon induced thermionic emission, the latter of which will be demonstrated separately in Ch. 5. This chapter closes on reporting three blind tests performed as proof of concept measurements.

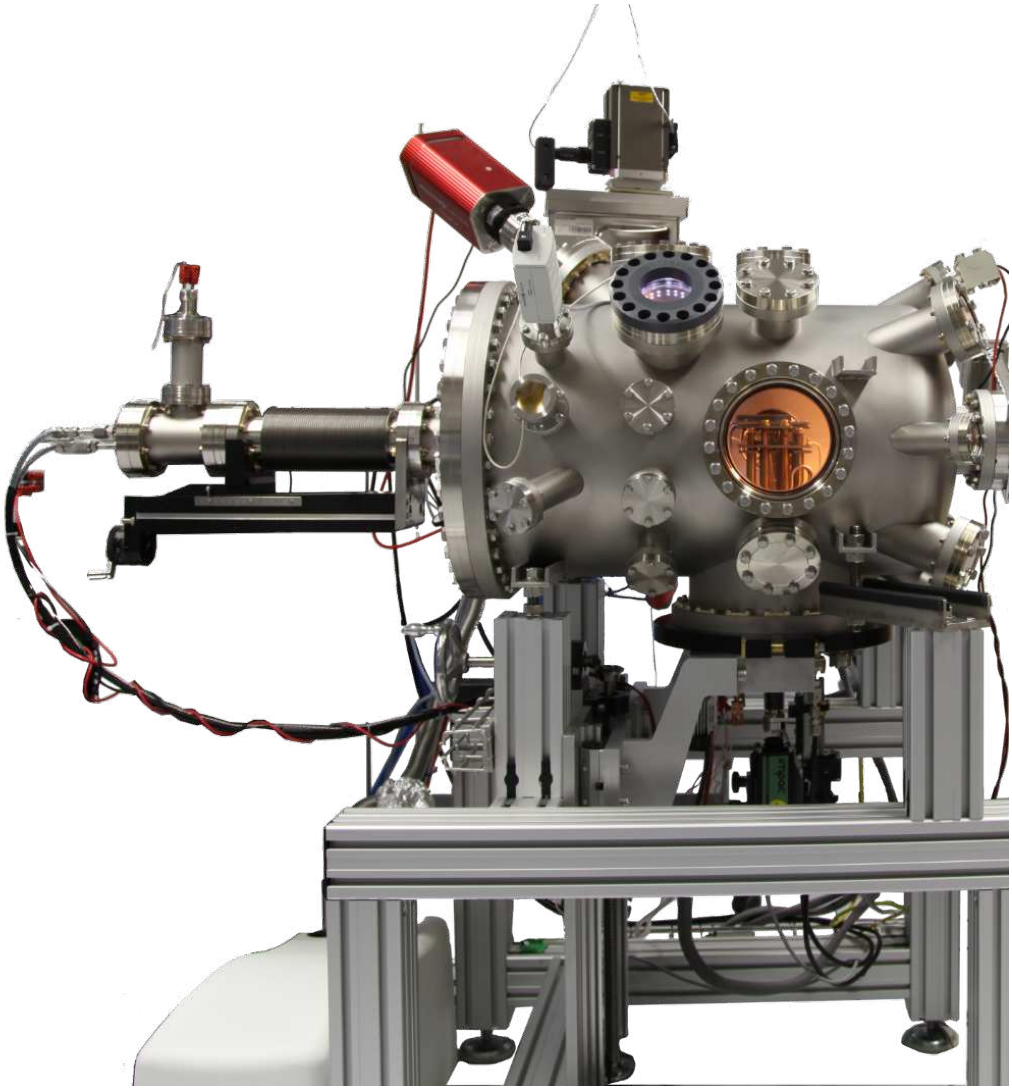

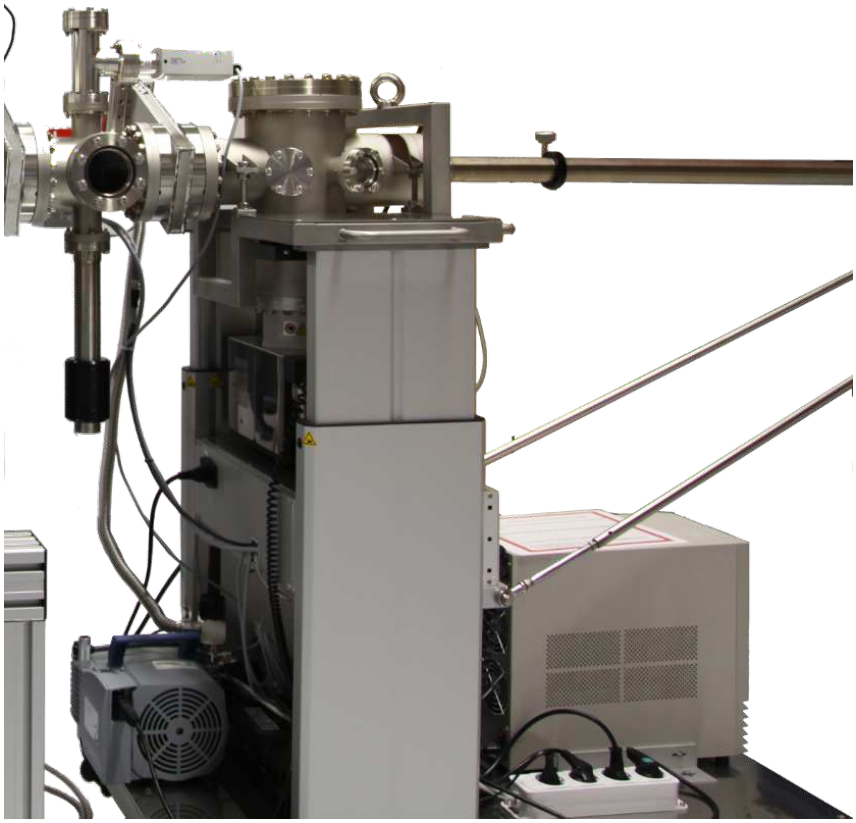

Figure 3.1: Split photograph of the measurement apparatus built for the work function measurements. On the left page, the measurement system is shown and the vacuum suitcase for the *in-situ* sample transport on the right page. The different components are labeled in Fig. 3.4.

3.1 Epitaxial Growth System

The samples investigated in this work were prepared and fabricated using an advanced epitaxial machine consisting of multiple fabrication and processing units. The primary units employed here include two pulsed laser deposition (PLD) systems, a sputtering system, and an electron beam evaporator. Figure 3.2a shows a rendered CAD model of the epitaxial system from above, with the corresponding units highlighted in red. In this system, all processing units are connected to each other by vacuum tunnels equipped with multiple ion pumps from *Agilent Technologies* [48], maintaining a pressure better than 3×10^{-8} mbar in every section. Substrates are prepared and installed in gloveboxes containing nitrogen gas, nominally free from water and oxygen, and loaded directly into the epitaxial system. The epitaxial growth is performed by PLD as laser pulses with an energy of more than $1\,\mathrm{J\,cm^{-2}}$ ablate a stoichiometric target material. This ablation process results in a plasma plume with the target material being partially ionized. The ablated species hit a heated substrate, and consequently epitaxially align themselves if the growth conditions are satisfied. Figure 3.2b shows an image of a pulsed laser deposition process.

During the ablation the growth and surface reconstructions are monitored by an integrated high-pressure reflection high-energy electron diffraction (*RHEED*) system. This tool consists of an electron source, a high-potential grid system for accelerating the electrons, and an electron-optic system for adjusting the electron beam. The resulting electron beam is focused onto the substrate surface with an incident angle typically below 5°, such that the electrons scatter from the topmost layer(s) of the surface. This grazing incident angle is crucial for obtaining atomically sensitive measurements of the surface. Figure 3.2b shows the locations of the sample, the RHEED gun and the camera during a high-temperature deposition. The RHEED system used in this work operates at an accelerating voltage of 30 kV with a nominal incident angle of about 3° with respect to the substrate surface.

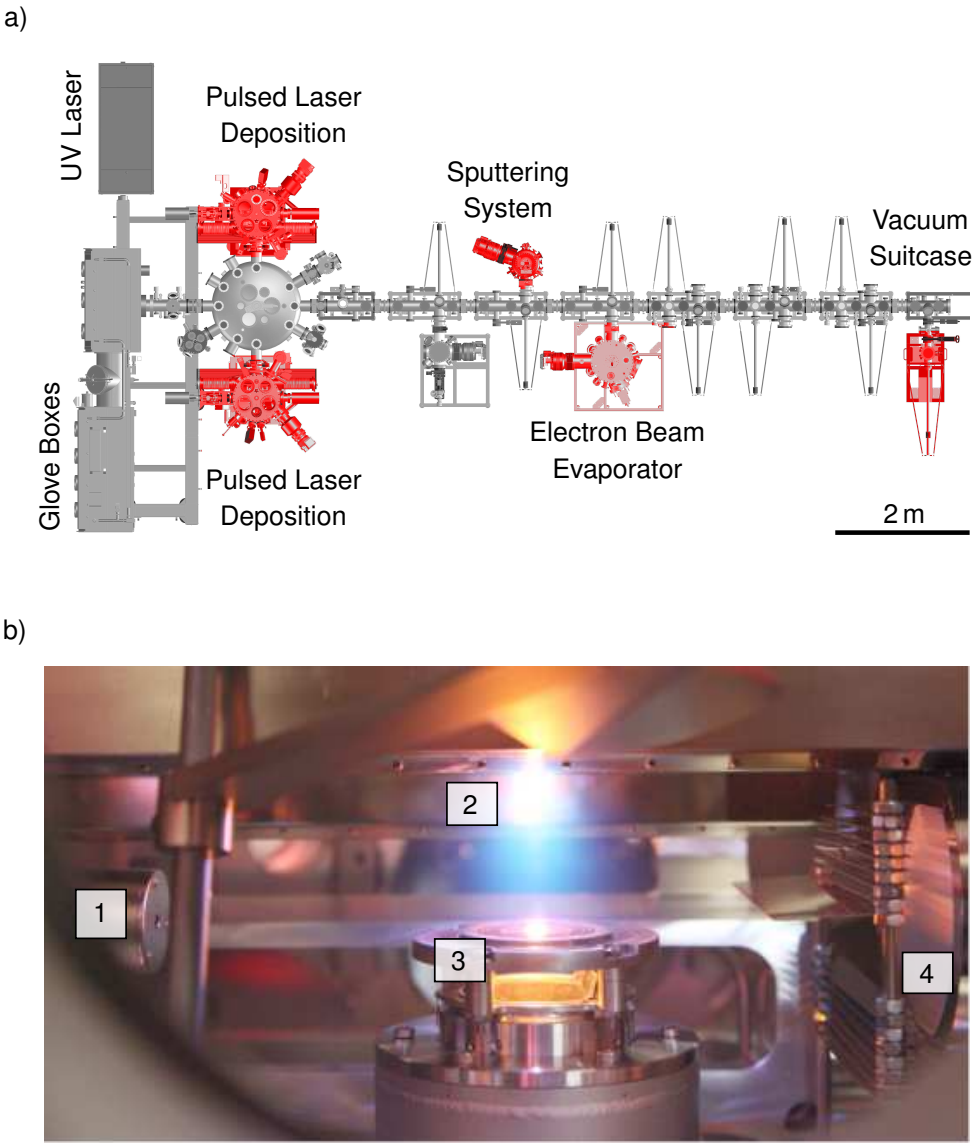

Figure 3.2: a) Rendered CAD model of the epitaxial growth system used for sample fabrication with the relevant units highlighted in red. The epitaxial growth is performed by pulsed laser deposition, platinum stripes are deposited by the electron beam evaporator. After fabrication, the samples are loaded into the vacuum suitcase and transported to the measurement apparatus. Image courtesy of Manfred Schmidt and Ingo Hagel. b) Photograph of a high-temperature deposition of $LaAlO_3$ on a $SrTiO_3$ substrate. (1) shows the position of the RHEED gun at an angle of $<3°$ with respect to the substrate surface, (2) the plasma plume during the ablation, (3) the sample glowing at a temperature of more than 1000 °C and (4) the position of the phosphorous screen. Image courtesy of Ali Teker.

The scattered electrons from the surface need to satisfy the diffraction condition [49]:

$$\vec{k'} - \vec{k_0} = \vec{G} \tag{3.1}$$

where $\vec{k'}$ and $\vec{k_0}$ are the diffracted and incident wave vectors respectively, and $\vec{G}$ is the reciprocal lattice vector. As shown in figure 3.3b, when the diffraction conditions are satisfied, the diffraction spots can be seen on a phosphorous screen. Based on the step-density model [50, 51], when the deposition begins the surface becomes rough as the arriving atoms start to align themselves through nucleation and island-formation processes. As a consequence, the scattering becomes more diffusive and the intensities of the diffraction spots decay. As soon as the quantity of arriving material is sufficient and the ionized species have epitaxially aligned themselves, the growth of the first atomic layer is supposedly complete. As a result, the intensities of the diffraction spots start to rise again as the diffraction conditions are once again met. This process repeats for the growth of every unit cell and results in oscillations of the recorded intensities with each oscillation indicating the successful growth of one unit cell. Figure 3.3a shows the RHEED oscillations during the growth of $SrRuO_3$ on a Nb:$SrTiO_3$ (0.5 wt.%) substrate at an oxygen background pressure of 0.1 mbar.

The growth of oxides typically requires an oxygen atmosphere to prevent oxygen reduction of the arriving species, as well as of the heated oxide substrate. On the other hand, the electron source of a RHEED system requires low pressures for operation. These two different pressure regimes are realized by a differential pumping system [52] consisting of two turbomolecular pumps between the electron source and the deposition chamber. By this, the pressure of the RHEED system is secured in the lower 10^{-7} mbar, while the deposition can be carried out at pressures exceeding 0.1 mbar.

The electron beam evaporator is another important unit of the epitaxial system (see Fig. 3.2a). This unit was used for the deposition of platinum stripes after the epitaxial growthn . The stripes are defined by shadow masks. As discussed in the previous chapter, this reference material is used for the work

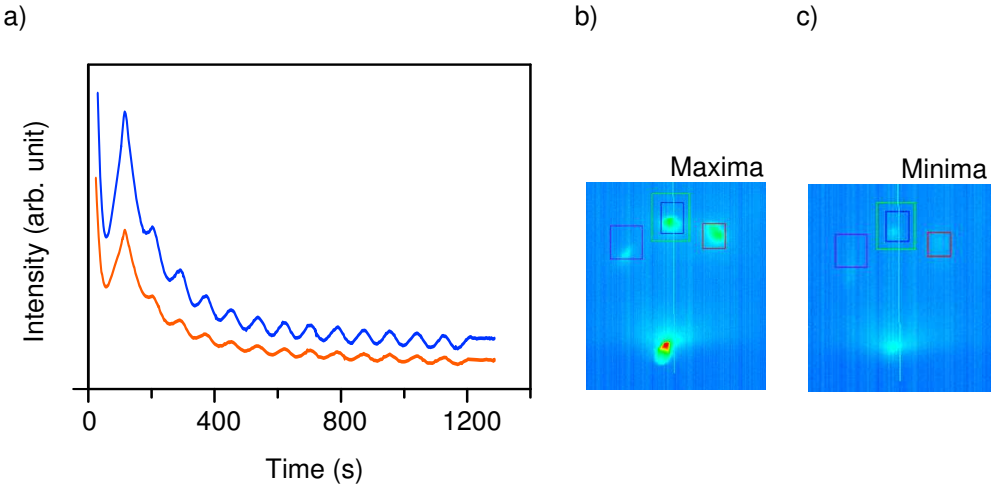

Figure 3.3: Growth monitoring during pulsed laser deposition by high-pressure, reflection high-energy electron diffraction (RHEED). The low incident-angle electrons scattered from the surface of the substrate create a diffraction pattern depicted by a phosphorous screen (b and c). The intensities of the diffraction spots are monitored during the growth. c) As the surface becomes rough during the deposition, the intensities start to decay, and b) increase again as soon as the diffraction conditions are established again (see text). Every oscillation indicates the completion of one unit cell. The oscillations presented here have been measured during the growth of $SrRuO_3$ on a Nb:$SrTiO_3$ (0.5 wt. %) substrate at a pressure of 0.1 mbar.

function measurements of materials for which no literature values are available. Platinum was chosen due to its inert and high-temperature properties and availability as a source in the evaporator unit. Since the different units of the epitaxial system are connected with vacuum tunnels with pressures of $<3 \times 10^{-8}$ mbar, this evaporation is an *in-situ* deposition. The thickness of these stripes is about 50 nm, evaporated at an acceleration voltage of 8 kV and a current of >250 mA. Eventually, the samples are transferred to the vacuum suitcase and consequently transported to the measurement apparatus.

During the sample fabrication and transport process the samples are either in a controlled atmosphere for deposition or a clean vacuum environment with a base pressure better than 5×10^{-8} mbar. Hence, the *in-situ* measurements are conducted with as little contaminants on the sample surfaces as possible.

3.2 The Measurement System and system characteristics

For the work function measurements, an ultra-high vacuum measurement apparatus was designed and constructed to perform precise measurements under operating conditions of a thermoelectronic energy converter. The technical drawings were done using the *PTC Creo Elements Modeling* [53] software. The apparatus is a thermoelectronic converter with the emitter and grid embedded in the instrument. The samples fabricated in the previously discussed epitaxial system are loaded *in-situ* and used as the collector. The work function of these *in-situ* loaded materials is investigated by the method discussed in chapter 2.2. The following discussion provides technical details and describes the concepts and conponents developed in this work. These include the heating mechanism of the emitter, the sample holder of the collector, and the thermoelectronic components.

Vacuum chamber and components

Figure 3.4 shows a rendered CAD model of the measurement apparatus designed in this work with connected vacuum suitcase. The design of the chamber is based on a molecular beam epitaxy system and consists of 8 ports for effusion sources, a 2°-off port for a RHEED gun with a 2 cm shifted port for the phosphorous screen and a DN400 CF port for a cooling shroud. The chamber was built by *VAb GmbH* [54] and is made from stainless steel. The surface of the chamber was blasted with glass beads and annealed at 300 °C to be free from contaminants and to obtain a low magnetic permeability.

The vacuum chamber is evacuated using a turbomolecular pump in combination with a Roots pump. Moreover, the apparatus is equipped with a mass spectrometer to detect possible contaminants and to monitor the residual gases during the experiments. The magnetic yoke is mounted on a linear feedthrough so that the experiments can also be conducted without a magnetic field. Furthermore, this movement allows the temperature of the collector to be measured by a pyrometer.

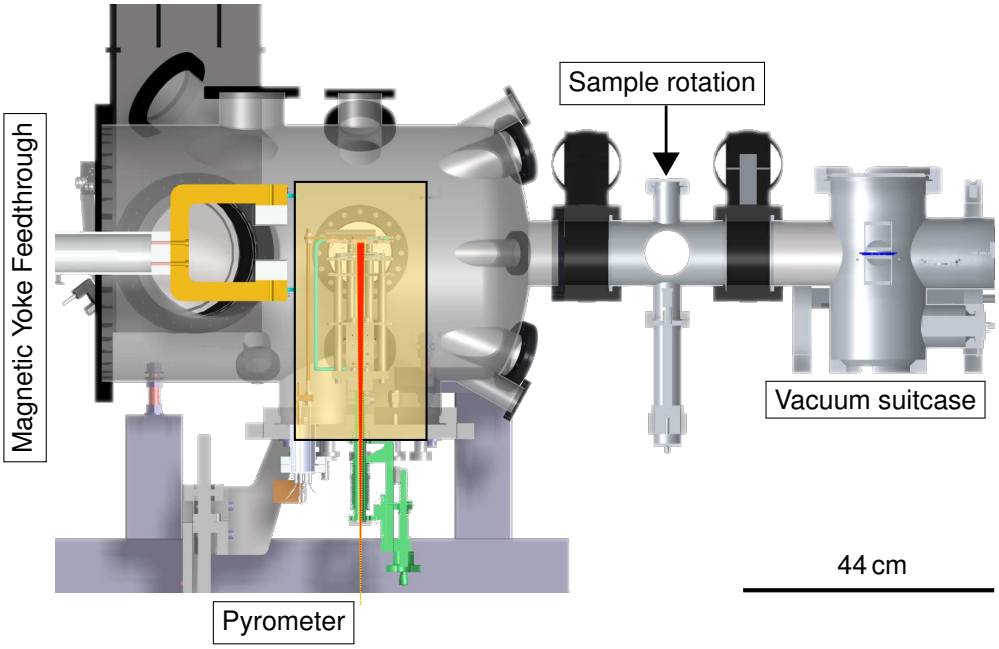

Figure 3.4: Rendered CAD model of the measurement apparatus and its components. The vacuum suitcase is connected to the chamber via a load-lock chamber, which separates the sample location and the measurement apparatus with two gate valves (shown in black). A wobble stick is used to rotate and align the samples before inserting them into the measurement stage. The measurement components, except for the magnetic yoke, are located on a DN250 CF flange on the bottom (highlighted in yellow). These components are shown in Fig. 3.5. The center of this flange coincides with the center of the samples, enabling a centered optical path for the experiments (shown in red). This path can be used for temperature measurements by a pyrometer.

The experimental design is based on a three stacked-parallel plane configuration and the movable magnetic yoke. Each plane consist of a base metal-sheet as shown in Fig. 3.5:

- **Fixed emitter plane**: In this plane, the emitter and the grid are in fixed positions on the metal sheet. The base plate is water cooled as the emitter is heated by the thermal radiation of a resistive heater. The metal sheet of this plane is shown in red in Fig. 3.5.
- **Movable collector plane**: This plane consists of an electrically isolated stage, where the sample holder is loaded from the vacuum shuttle. This stage is shown in blue in Fig. 3.5.
- **Movable plane**: The metal sheet of this plane shifts the collector plane into the measurement position by a linear shifter. This plane is designed to hold a resistive heater, light emitting diode or liquid nitrogen cooling for the collector. This plane is labeled in Fig. 3.5.

The base metal-sheets of each plane were ordered from *WHS GmbH* [55] and made from molybdenum to withstand the high temperatures required for the measurements. In the next section, an overview is given about the different components that are crucial for this work.

Heating method and spacing of components

The emitter is heated by the thermal radiation of a resistive heater made from tantalum. Tantalum foils were chosen due to their availability down to a thickness of 5 µm, their high melting temperature, mechanical stability after cooling down and because they have a vapor pressure comparable to tungsten. However, at elevated temperatures some evaporation of the filament is inevitable. Due to this, the high work function emitter used in this work was chosen from the same material, to reduce contamination. The temperature of the emitter is measured by a type-C thermocouple, touching the back side of it. The emitter temperature is regulated by a Eurotherm 3504 PID controller [56] that adjusts the current-source unit of the resistive heater. Before every

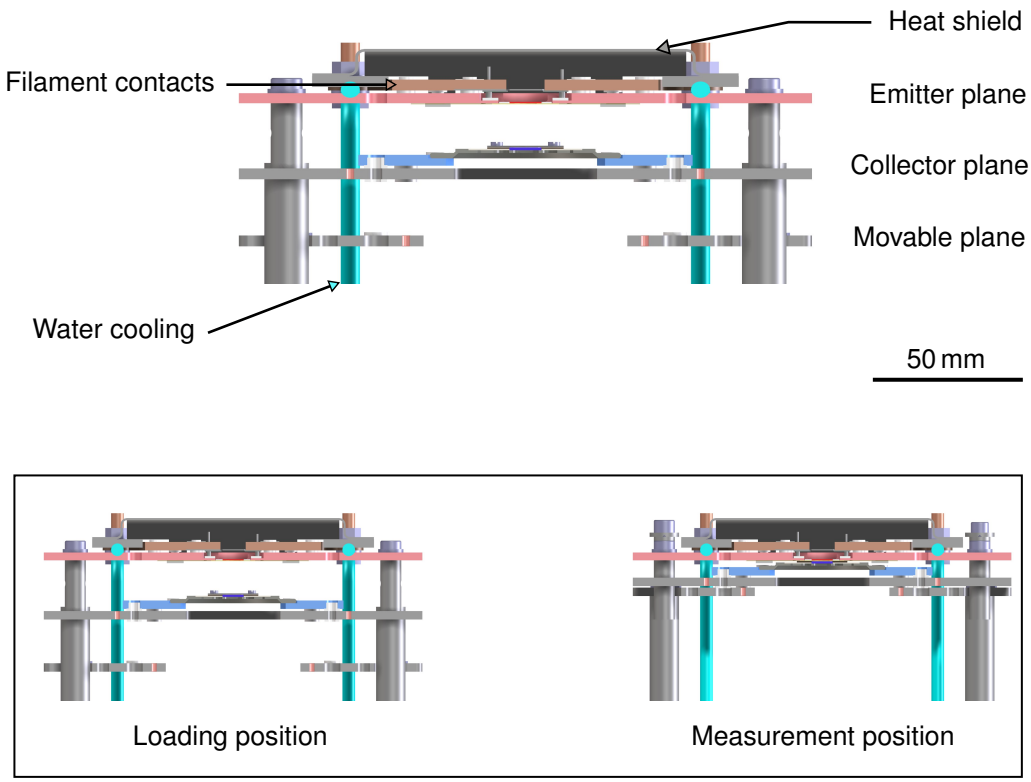

Figure 3.5: Rendered CAD models of the measurement planes. The emitter and grid are located and fixed onto the emitter plane, which is water cooled. The *in-situ* transported samples are loaded onto the collector stage, which is electrically isolated from collector plane. The movable plane takes the collector plane into the measurement position by a linear shifter, shown in green in Fig. 3.2. The inset below depicts the arrangement of the planes for loading samples on the left, and the measurement position where the planes are contracted on the right.

measurement, the contact of the thermocouple wires to the emitter is checked using a multimeter.

The distance between the emitter-grid-collector is constant and determined by the thickness of the spacers used in between of them. These spacers are made from pyrolytic boron nitride films, grown by chemical vapor deposition with a thickness of 250 µm, and ordered from *CVT GmbH* [57]. The advantage of these films is that they are capable of withstanding temperatures up to 1500 K without decomposing [58], are chemically resistant [59], mechanically

flexible, machinable, and have a moderate in-plane and a low out-of-plane thermal conductivity [60]. Nevertheless, these films have a high optical transparency in the near infrared regime [61, 62], allowing the heat radiation to pass through them. The emission area is defined by a circular hole on the spacer between the emitter and grid, that has a diameter of 7 mm. The distance between the grid and collector is determined similarly, but the spacers are fixed on the sample holder.

Design of the sample holder

The design of the sample holder is a crucial point in this work, due to temperature and electrical requirements, and due to the mechanical limitations during the *in-situ* transport process. It needs to be capable of handling high temperatures during the depositions that are performed in an oxygen environment, and must be a good electrical conductor for the electrical measurements. The latter requirement results from the fact that the sample holder is the actual electrical contact to the samples for the electrical measurements. Therefore, a sample holder was designed and made from Haynes® 25 metal alloy [63] to meet the high-temperature requirements, and coated with 500 nm of platinum to prevent it from oxidizing during the growth and ensuring a good electrical contact.

The transport process of the samples from the PLD chambers to the other sections of the epitaxial system (Fig. 3.2) inevitably involves a flip mechanism that orients the surface of the samples facing downwards. Due to this, the samples were mechanically fixed to the sample holder by boron nitride films of the same thickness as the spacer used for the emitter and grid. With this, the distance between the collector and grid is the same as the emitter to the grid, and the samples are kept in place during transport. Furthermore, this mechanical stabilization was designed such that the surface area of the samples were not hindered for monitoring the epitaxial growth by RHEED. Thus, the sample holder allows a glancing incident angle for the electron beam, with a $\pm 45°$ rotation of the holder in the XY-plane for RHEED alignments. Figure 3.6 shows rendered CAD models of the sample holder with the boron

nitride spacers.

Before each deposition and measurement, the spacers are cleaned and etched in a diluted aqua regia solution ($HCl:HNO_3$, molar ratio of 3:1) in an ultrasonic bath at 40 °C and afterward rinsed with deionized water. The surface of the holder is subsequently coated with 100 nm of platinum to ensure a good electrical conductivity. The design of the sample holder stage itself (Fig. 3.6c) is inspired by the Kelvin clamp mechanism [64], which allows a $\pm 2°$ tilt option of the individual stages supporting the sample holder on the collector plane. By this, the sample holder can align itself parallel to the fixed emitter plane when the sample holder is placed into the measurement position (see Fig. 3.5).

Magnetic yoke and grid

The key thermoelectronic components are the magnetic yoke and the laser-cut metal grids. The magnetic yoke is made from pure iron with a galvanic coating of gold to protect it from oxidation. The field is generated by stacked NdFeB permanent magnets ordered from *IBS Magnets* [65], each with a nominal strength of 1 Tesla. The dimensions of the yoke were optimized by finite element method simulations of the magnetic field using FEMM [66] in order to ensure a homogeneous field at the center of the grid over the entire emission area. The result of these simulations is shown in Fig. 3.7a. The magnetic field at the center of the grid was measured to be 280 mT to 300 mT and reasonably homogeneous, in agreement with the simulation results.

By embedded water pipes the magnetic yoke is cooled. Heatshields made of tantalum sheets protect the stacked magnets from the thermal radiation (not shown here). A type-C thermocouple continuously monitors the temperature of the magnets. As a result, the temperature did not exceed 35 °C.

The grids used in this work are laser cut tungsten and tantalum foils, as presented in Fig. 3.7c-d. The tungsten grid is made with a large mesh size of about of about 1 mm, suitable for photon-induced thermionic emission experiments, because laser light can be focused through its holes as demonstrated in chapter 5. Nevertheless, this grid was also used for the proof-of-concept

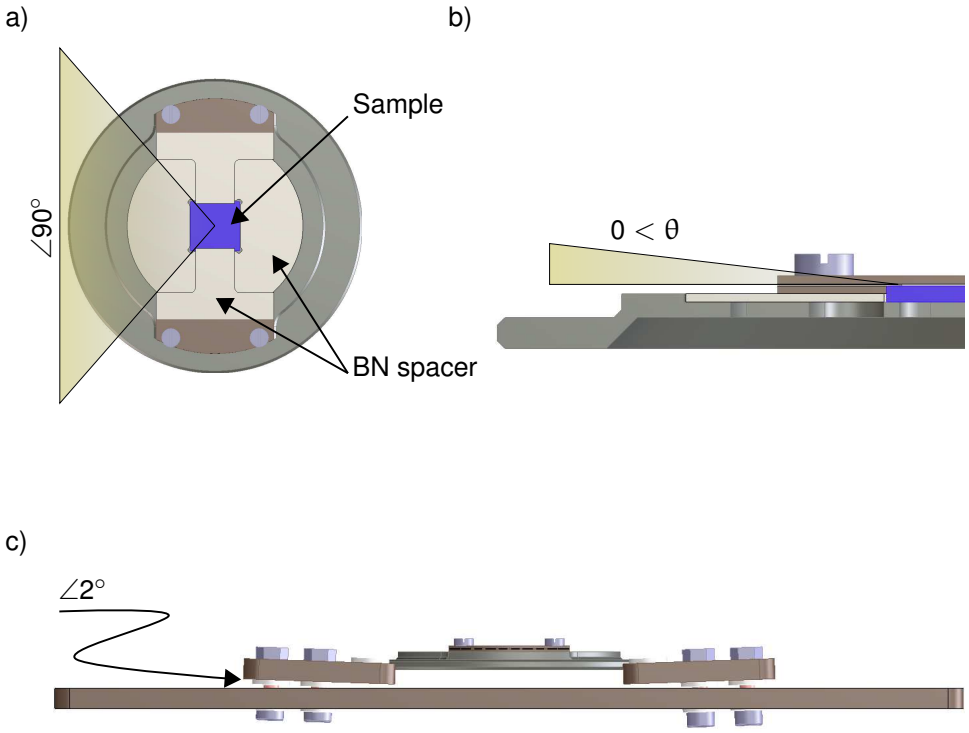

Figure 3.6: Rendered CAD model of the sample holder showing a) the possibility of rotation in the XY-plane for RHEED alignments, and b) grazing incident angles of the electron beam of the RHEED. Panel c) Shows the flexibility of the collector stage for ensuring a parallel configuration at the measurement position. The diameter of the sample holder is 60 mm, optimized for samples with dimensions of 10 mm × 10 mm × 0.5 mm. The yellow highlighted areas are a visual representation of the discussed angles.

measurements discussed in the next section and demonstrated reliable results. The tantalum grid was designed during this work to optimize the homogeneity of the electrostatic field, and also to improve the thermal shielding of the collector from the filament radiation, passing through the boron nitride spacers.

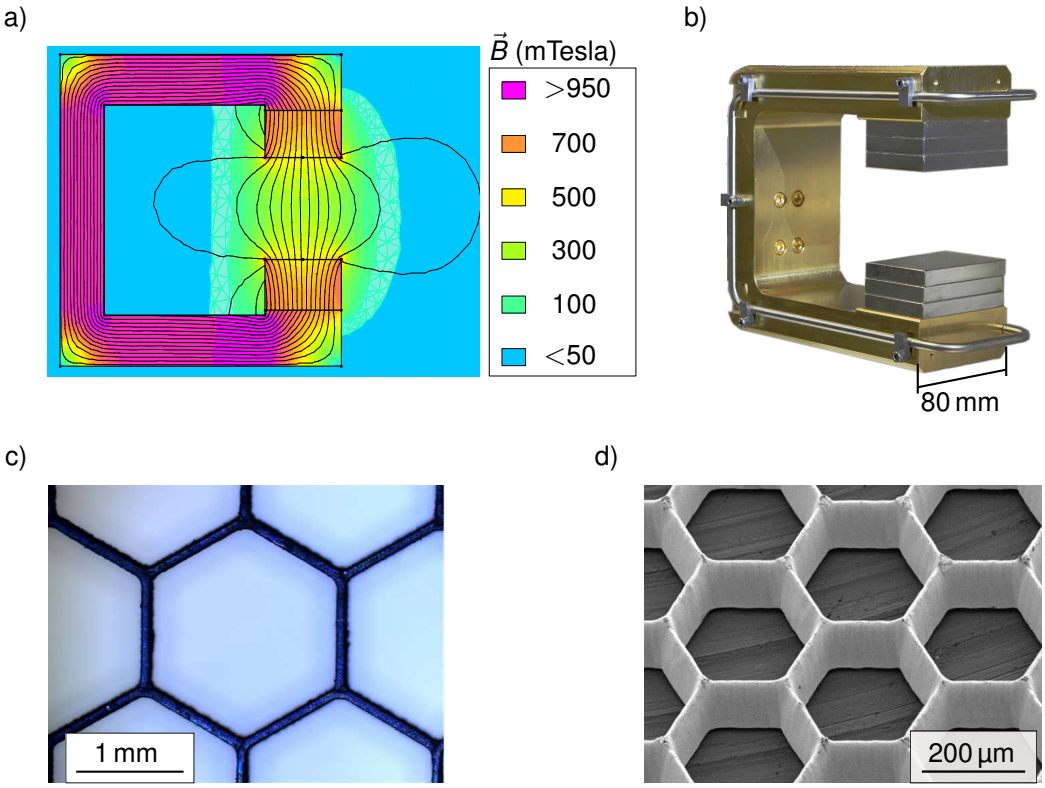

Figure 3.7: Thermoelectronic components used in this thesis. Panel a) Shows the simulation of the magnetic field using FEMM [66], next to b) a photograph of the magnetic yoke. The yoke is coated with a thin layer of gold to prevent oxidation, and has cooling-water pipes embedded. c) Optical microscope image of the tungsten grid with a large mesh size of ≈1.65 mm used for photon-induced thermionic emissions and d) SEM image of laser-cut tantalum grid with a fine mesh size of ≈240 µm.

Electrical diagram

The diagram of the electric circuits used for the experiments is shown in Fig. 3.8. The source measure units (SMUs) are all Keithley 2602B series [67]. These devices offer the specifications required for the experiments, such as a relatively high resolution in the nA regime, and fast voltage measurements with µV resolution. These devices communicate through Ethernet protocols, which is advantageous as compared to the historical GBIP communication protocol. By taking advantage of the 4-wire-mode settings, the potential drop due to the wiring resistance is measured and compensated by the SMUs for both the grid and the collector. However, the wiring resistance was measured to be less than $5\,\Omega$ for the collector and below $2\,\Omega$ for the grid. Therefore, considering the currents used in the experiments, the potential drop due to the wiring resistance is negligible as it is below the resolution of the measurement apparatus. Nevertheless, these contacts can be used alternatively to control *in-situ* the functionality of the electrical contacts to the grid and collector without opening the chamber, and in the case of a broken contact, a backup-contact will be available.

The voltage-sweep measurements are carried out in the following order:

- first the emitter is set to the reference potential, and a constant voltage is applied to the grid,
- the voltage of the collector is applied (or changed), and then
- the current values of the emitter (I_{em}), grid (I_{gr}), and collector (I_{cl}) are recorded.

For data acquisition, a software program was developed using the *National Instruments LabView*™. This software is capable of recording the measurement data, monitoring the system pressure, the temperatures of the different parts of the apparatus, and communicates with the PID controller to regulate the emitter temperature.

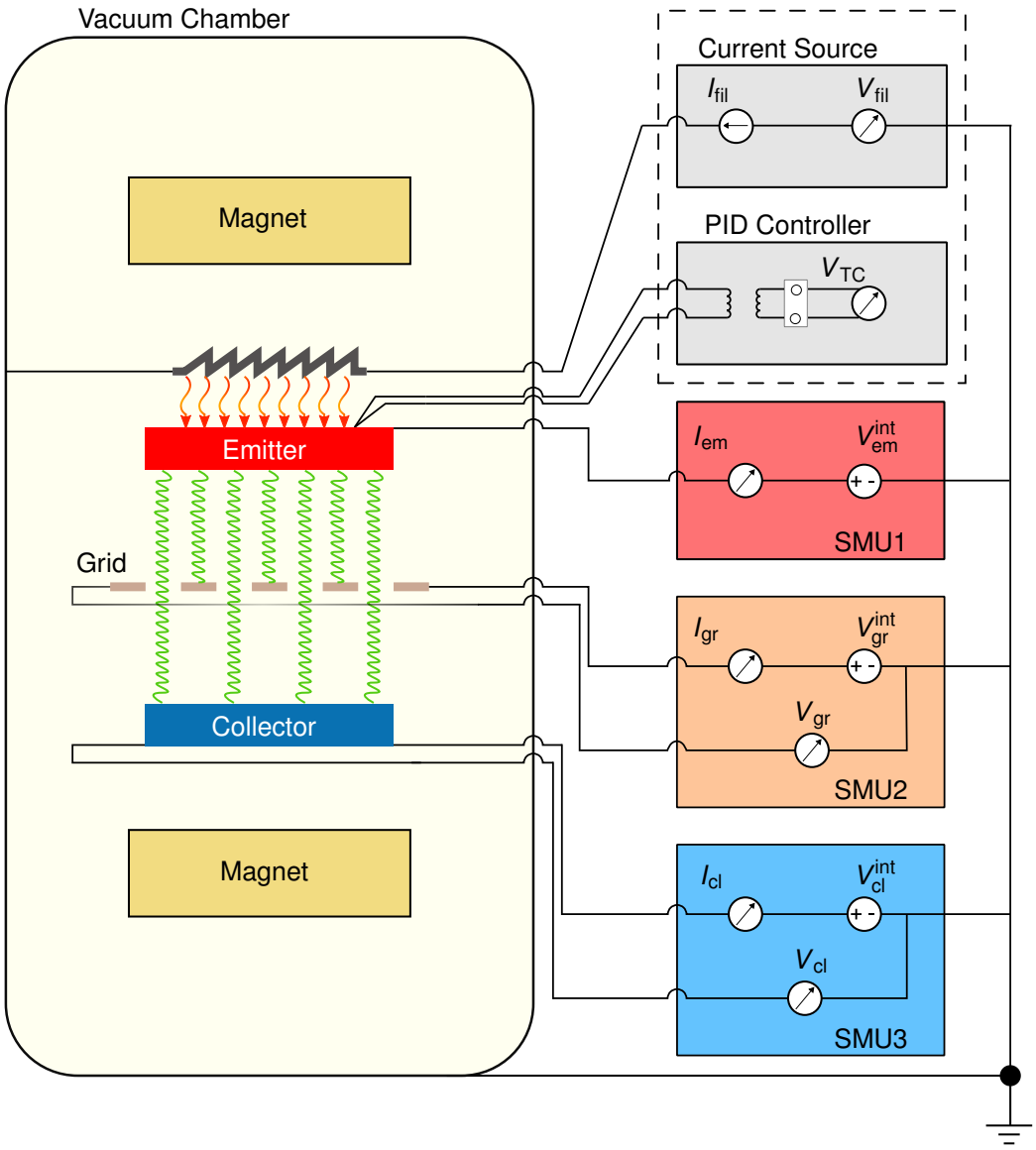

Figure 3.8: Sketch of the electrical wiring diagram of the measurements. A thin tantalum foil is used as a resistive heater, while a type-C thermocouple measures the temperature of the emitter. This temperature is adjusted using a PID controller, which regulates the current of the resistive heater. The voltage of the emitter is set to the reference potential ($V_{em} = 0\,V$), and the grid and collector voltage is applied in a 4-wire mode for accuracy and monitoring the functionality of the contacts. The electrical isolation of the cables inside the vacuum chamber is accomplished by aluminum oxide ceramic tubes, beads, and washers. The green spiral-lines are a schematic representation of the emission current.

3.2.1 System characteristics

Residual gas spectrum

Since the experiments are highly sensitive to surface contaminants, special care has been taken to establish and maintain a clean measurement environment. The chamber is equipped with a large area tantalum heater to anneal the system components inside the system. However, some contaminants could not be removed by this heating procedure. Therefor an argon-oxygen plasma was ignited to remove them [68]. As a result, contaminants were removed to a large extent, and by a sufficiently long pumping period, base pressures as low as 3×10^{-9} mbar were obtained. Figure 3.9 shows a residual mass spectrum of the measurement apparatus.

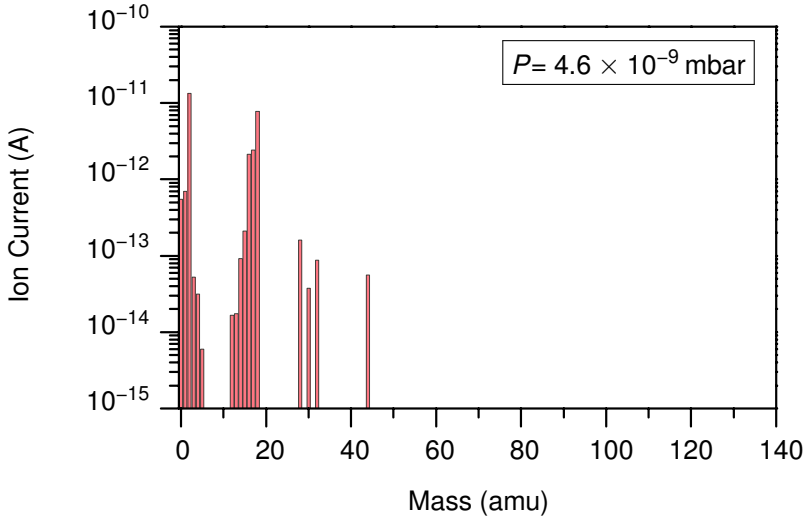

Figure 3.9: Mass spectrum of the measurement apparatus in an idle state (room temperature), after a long pumping period. The majority of the residual gas belongs to water (H_2O= 18 u, OH= 17 u, ...). This is due to the fact that the chamber is not baked out and the pre-vacuum pump line is typically at a pressure of 1×10^{-1} mbar. The coexistence of the carbon dioxide and monoxide (CO_2= 44 u, CO= 28 u) peaks indicates a possible virtual leak in the system. The low base pressure and the mass spectrum indicate a clean environment for the purpose of this work.

Emitter characteristics

As mentioned earlier, the emitter is heated by the thermal radiation of a resistive heater, while emission currents are recorded using a source measurement unit. By optimizing the shape of the filament, its angle, and most importantly its distance to the emitter[1], temperatures above 1950 K were achieved. The temperature of the emitter is described as a function of the input power of the filament (P_{fil}) by the following equation:

$$P_{\text{fil}} = C_0 T_{\text{em}}^4 + C_1 T_{\text{em}} + C_2. \tag{3.2}$$

The first term is due to radiation, and the second term due to thermal conductivity. This behavior is illustrated in Fig. 3.10a. However, note that the temperature is measured on the backside of the emitter and does not correspond to the temperature of the surface. Thus, the temperature of the emitter surface is expected to be lower than the actual measured value.

Since the temperature and the emission current of the emitter can be precisely measured, the emitter work function can be determined *in-situ* by the Richardson-Dushman equation (see Eq. 2.3). Figure 3.10b shows the work function measurement of a tantalum emitter by this method. This measurement was performed in a standard thermionic approach, without applying a magnetic field. For the space-charge suppression, a potential of 40 V was applied to the grid to accelerate and attract the electrons, while the collector voltage was set to −10 V to ensure that the grid absorbs all electrons. From the fit of Eq. 2.3 to the total emission current, the work function of tantalum was determined to be 4.28 eV, with a Richardson constant of 154 $\text{A K}^{-2}\,\text{cm}^{-2}$ (see Fig. 3.10b). These values are in good agreement with the reported values for tantalum (see table 3.1).

[1] The distance between the foil and the emitter is important due to view factor, discussed in detail in reference [69].

Table 3.1: Comparison of the thermionic constants of tantalum.

$\Phi_{\mathrm{WF}}^{\mathrm{Ta}}$ (eV)	A_{RD} $(\frac{\mathrm{A}}{\mathrm{K^2\,cm^2}})$	Method	Crystal Orientation	Ref.
4.28 ± 0.04	154 ± 37	Thermionic	Polycrystalline	This work
4.16-4.24	122	Retarding field	100	[70]
4.35	120	Thermionic	211	[44]
4.25	-	Retarding field	211 (70%)	[34]

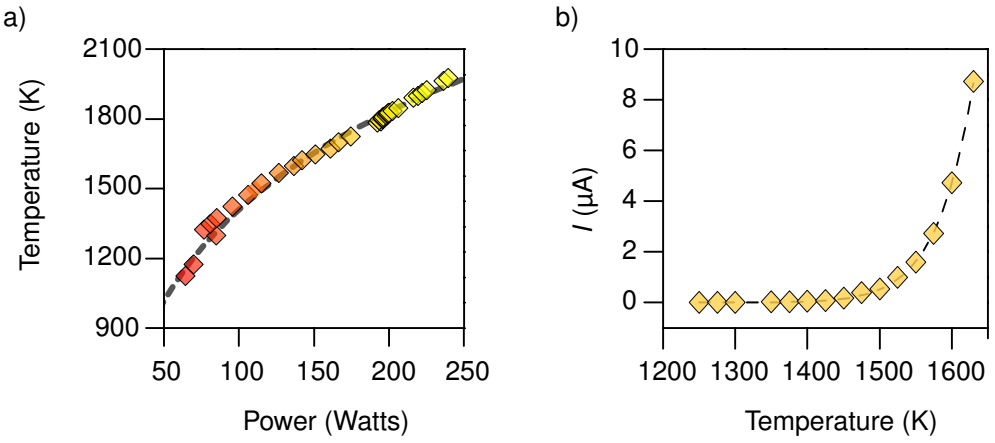

Figure 3.10: Temperature and electron emission characteristics of a tantalum emitter. a) The measured emitter temperature follows nominally Eq. 3.2, which is represented by the dashed line. b) The total emission current of the tantalum emitter as a function of temperature. The fit to the Richardson equation (dashed line, see Eq. 2.3) yields in a work function of $4.28 \pm 0.04\,\mathrm{eV}$ and a Richardson constant of $154\,\mathrm{A\,K^{-2}\,cm^{-2}}$.

3.2.2 Space-charge suppression in thermoelectronic converters

The measurement concept described in Sec. 2.2 is based on the assumption of a space-charge free transport of the emitted electrons to the collector surface. In a thermoelectronic converter, the space-charge is suppressed by a positively-charged grid that accelerates the electrons towards the surface of the collector. The applied magnetic field keeps the electrons on nominally straight trajectories [3]. The measurement apparatus built in this work demonstrates the characteristics of a thermoelectronic converter, as Fig. 3.11 illustrates. Here, the grid voltage is kept constant at $V_{\mathrm{gr}} = 15\,\mathrm{V}$ and the magnetic field is switched (*i.e.*, enabled/disabled). As discussed in Sec. 2.2, by applying the magnetic field, the collector current increases exponentially and becomes constant after the vacuum levels have aligned. Moreover, the total current arriving at the collector exceeds 80% of the total emitted current at moderate grid voltages. Similar behavior has been demonstrated by S. Meir [3]. Thus, Fig. 3.11 demonstrates that the designed apparatus meets the fundamental characteristics of a thermoelectronic converter. However, this apparatus is not optimized for efficient energy conversion, but rather precise $I(V)$ characterization of its components, such as the collector. This is demonstrated and discussed in the next section by a series of "blind tests," which provided the proof-of-concept measurements.

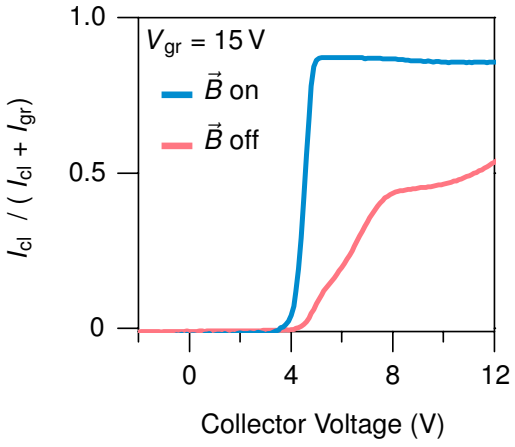

Figure 3.11: Space-charge suppression in the designed thermoelectronic converter at $T_{\mathrm{em}} = 1500\,\mathrm{K}$. By applying a magnetic field, the current increases exponentially and saturates afterward. The collector in this experiment is a Nb:$SrTiO_3$ (0.1 wt. %) single crystal sample, after several hours.

3.3 Proof-of-concept and Blind Tests

Three "blind test" measurements verified the measurement concept, the analysis method, and the precision of the measurements. For these measurements, samples which were unknown to the author were prepared and provided for work function characterization. As literature values for the work function of these materials are widely available, the outcome of these experiments could be used to asses the measurement concept. Two of the samples were elemental metals while one was an oxide heterostructure deposited and fabricated by pulsed laser deposition. In the following discussion, these measurements are presented.

3.3.1 Test one

The first sample of this series was a metal. It was cleaned using acetone, isopropanol and deionized water in an ultrasonic bath for 10 minutes in every step. Furthermore, the sample was annealed at a nominal temperature of 450 °C at a pressure of 5×10^{-8} mbar and subsequently transported to the measurement apparatus using the UHV suitcase. Before the measurement, the work function of the emitter was measured by the Richardson method, and found to be 3.22 eV. This change of the emitter work function was due to measurements carried out beforehand, where the samples were not stable at elevated temperatures and contaminated the surface of the emitter.

The $I(V)$ curves obtained for this sample are shown in Fig. 3.12 at an emitter temperature of 1475 K and a grid voltage of 28 V. For this sample, no reference material was used for calibration and the work function was directly estimated in reference to the emitter. The linear approximation of the logarithmic plot of the current as a function of collector voltage indicates that the band alignment occurs at eV_Φ =1.37 eV above the vacuum level of the emitter. In addition, the full width at half maximum (FWHM) of $\mathrm{d}I_{\mathrm{cl}} / \mathrm{d}V_{\mathrm{cl}}$ is about ±0.23 eV, which hints at a polycrystalline sample. Because the work function of the emitter was determined to be 3.22 eV, the work function of this sample results in 4.59 eV.

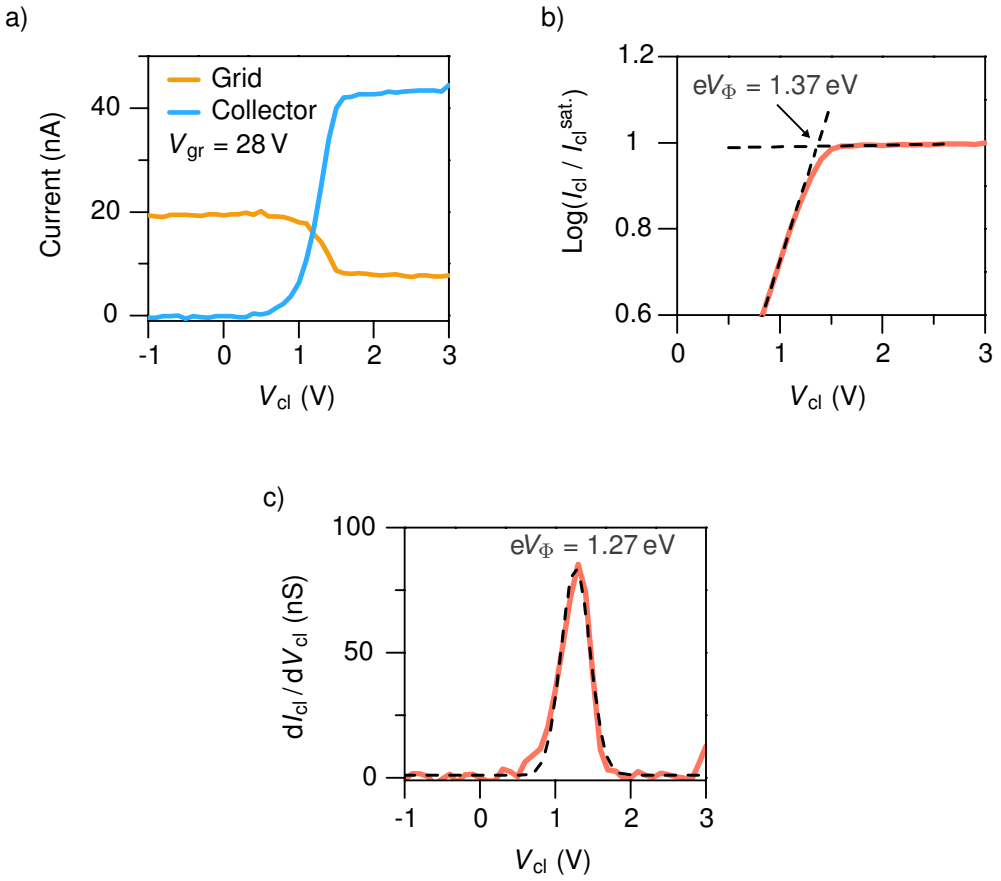

Figure 3.12: a) $I(V)$ curve of "Blind Test 1" at $T_{em} = 1475\,\mathrm{K}$ and $V_{gr} = 28\,\mathrm{eV}$. b) From the log-analysis the band alignment takes place at $eV_\Phi = 1.37\,\mathrm{eV}$. The work function of the emitter was determined to be 3.22 eV by the Richardson method. Thus, the work function of this sample is measured to be 4.59 eV. c) The large FWHM of the $\mathrm{d}I_{cl}\,/\,\mathrm{d}\,V_{cl}$ curve is $\pm 0.23\,\mathrm{eV}$ that suggests a polycrystalline sample.

It was then revealed that the sample was a pure piece of molybdenum. The work function of molybdenum is reported to be 4.55 eV for the (111), and 4.53 eV for the (100) orientation [33]. Moreover, for a polycrystalline molybdenum sample, the reported value is found to be 4.6 eV [33], in excellent agreement with the value measured here.

3.3.2 Test two

The second sample investigated in this series was fabricated by pulsed laser deposition. The sample was handed over in its sample holder inside the epitaxial system (see Fig. 3.2), ready to be transported to the measurement apparatus. As discussed in chapter 2.2, in this experiment we took advantage of a platinum stripe as a reference material deposited *in-situ* by electron beam evaporation.

Figure 3.13 summarizes the measurement results for this sample. Unfortunately, the sample was not stable at the measurement conditions and began to contaminate the system at the emitter surface. Figure 3.14 shows the residual mass spectrum of some selected elements and the pressure of the chamber during the measurements. Due to the strong outgassing of the sample, the pressure exceeded 7.5×10^{-7} mbar during the experiments. Due to this unstable behavior, the work function of the emitter varied drastically as the band-alignment position of the platinum stripe at +0.16 eV reveals. Hence, the work function of this sample can only be estimated from the reference platinum stripe.

The work function of polycrystalline platinum on molybdenum resulted in $\Phi_{\mathrm{WF}}^{\mathrm{Pt}} = 5.24\,\mathrm{eV}$, as demonstrated in chapter 2.2. Furthermore, the band-alignment voltage of the actual sample occurs at about $-0.27\,\mathrm{eV}$, where, interestingly, the converter produces power. Based on these, the work function of this sample is estimated to be 4.8 eV. However, since the source of the contamination is unknown, the obtained value must be considered with care. The contamination might originate from the sample itself, due to decomposition during the measurements, or from a contaminated sample holder. In addition, the contaminants might form a residue on the reference platinum stripe and alter its work function. Thus the reported value here is not conclusive.

It was revealed that the sample was a $SrVO_3$ thin film, deposited on an undoped $SrTiO_3$ substrate. This substrate was annealed at a temperature of >1300 °C in UHV environment to obtain an oxygen-deficient, and hence conductive, substrate. It appears that the high-temperature treatment of the

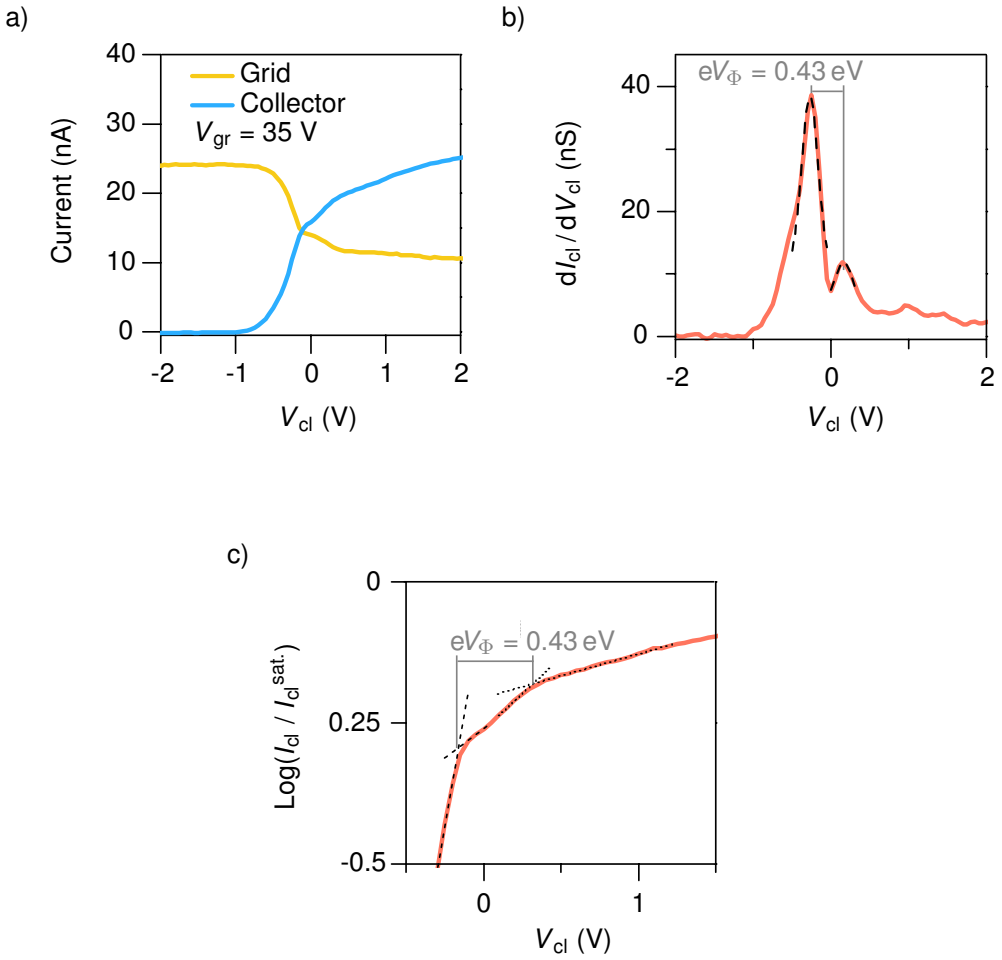

Figure 3.13: a) $I(V)$ curve of "Blind Test 2" at $T_{em} = 1350\,\mathrm{K}$ and $V_{gr} = 35\,\mathrm{eV}$. From b) the $\mathrm{d}I_{cl} / \mathrm{d}V_{cl}$ analysis and c) the logarithmic plot, the band alignment position for the sample and the platinum differ by $eV_{\Delta\Phi} = 0.43\,\mathrm{eV}$. However, the sample was not stable under the measurement conditions and eV_Φ varied rapidly over time, in addition to the substantial reduction of the current (see text).

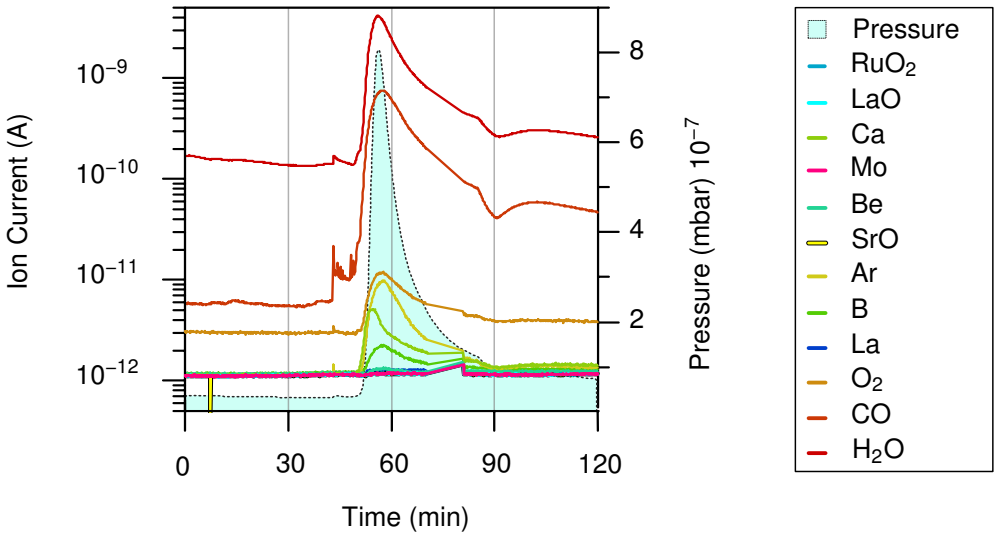

Figure 3.14: Mass spectrum of selected compounds and elements plotted alongside pressure during "Blind Test 2". After the very first voltage sweeps, the residual gas spectrum shows an increase of many contaminants while the pressure reaches 8×10^{-7} mbar during the measurements. Typical pressures during an experiment is below 1×10^{-7} mbar for a clean sample, where most of the increase is due to water.

substrate caused strong contamination during the fabrication process. The contamination might occur from the sample holder itself, which inevitably heats up to extreme temperatures during this process. Unfortunately, no experimental values are currently available for $SrVO_3$ thin films to either confirm or dispute the outcome of this experiment.

3.3.3 Test three

The sample of the third "blind test" was a pure metal, like the first one. The sample was delivered clean and in a glove box atmosphere, and no additional cleaning procedures were taken. Still, the sample was annealed in UHV conditions at a nominal temperature of 450 °C for more than 30 min. A platinum stripe was subsequently deposited for calibration purposes.

Before the measurements, the emitter was annealed for several hours at temperatures exceeding 1550 K to clean the emitter as well as the grid from the contamination of the previous measurement. After this annealing process, the work function of the emitter was determined by a 100 nm thick platinum coated sample to be 4.65 eV, which is about 1.5 eV higher when compared to "Blind Test 1" (see Fig. 3.12). Although the system could not be fully recovered, it exhibited a stable behavior to proceed with the next test.

The measurement results of "Blind Test 3" are presented in Fig. 3.15. All measurement curves indicate that the work function of the sample and the platinum stripe are identical within the resolution limit of the measurement system. Thus, the work function of this sample is estimated directly from the emitter work function. The $I(V)$ curve presents a smooth behavior, and the differential conductance plot shows no additional peak as well. The linear fits to the logarithmic plot of the $I_{\mathrm{cl}}(V_{\mathrm{cl}})$ curves estimates the band-alignment position at +0.68 eV. Moreover, the large FWHM of the $\mathrm{d}I_{\mathrm{cl}}/\mathrm{d}V_{\mathrm{cl}}$ plot indicates a polycrystalline sample. Based on these, the work function of "Blind Test 3" is estimated to be ≈5.33 eV, assuming a constant and stable work function of the emitter throughout the course of the measurement.

It was revealed that the sample was pure platinum, in agreement with the results obtained here. The work function of platinum is reported to vary from 5.12 eV for the (311) orientation to 5.93 eV for the (111) orientation (see table 2.1). Nonetheless, the obtained value is in good agreement with the value obtained for a platinum thin film on a molybdenum sample in this work (5.24 eV, see Ch. 2.2), and in excellent agreement with the reported value for bulk polycrystalline samples by Nieuwenhuys *et al.* (5.32 eV) [27].

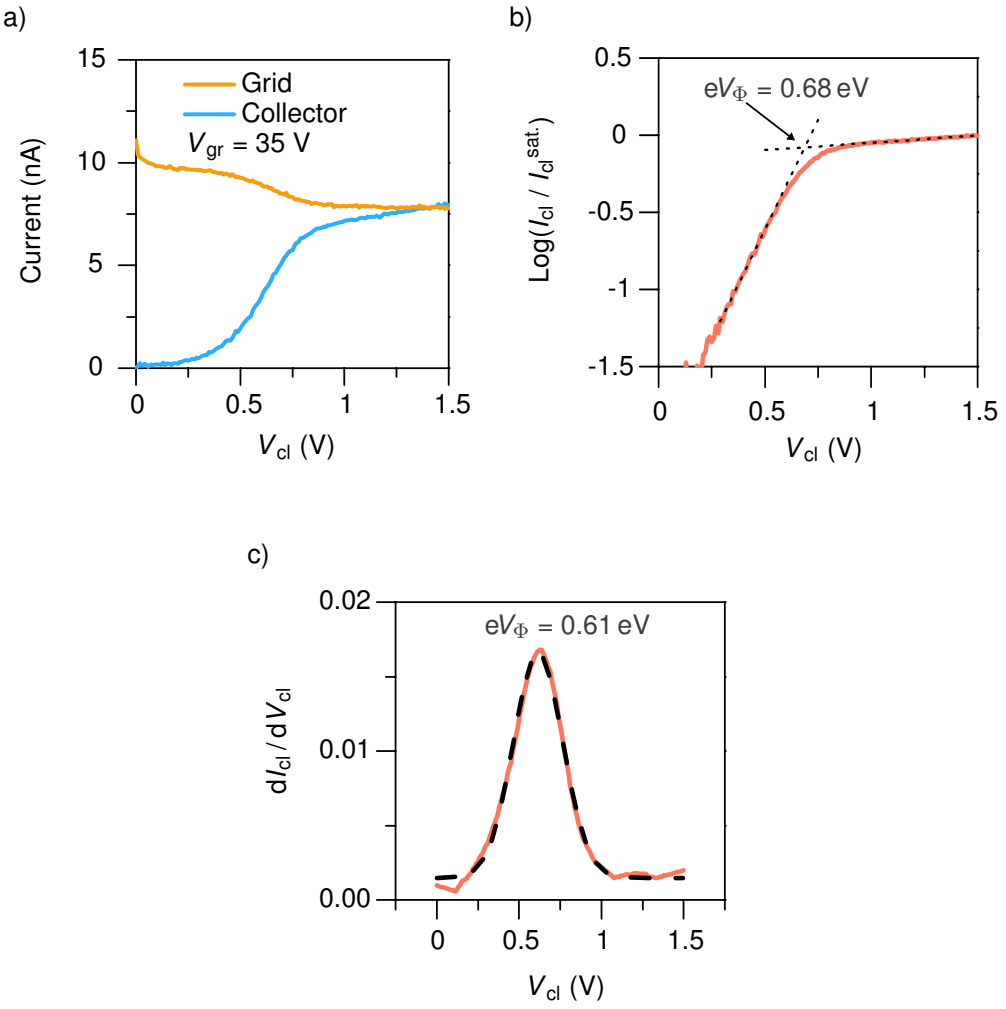

Figure 3.15: Measurement results of "Blind Test 3" at $T_{em} = 1450\,\mathrm{K}$ and $V_{gr} = 35\,\mathrm{V}$. a) The $I(V)$ curve shows no additional rise within the sweep range. b) The band alignment voltage is estimated from the logarithmic plot of the current, at $eV_\Phi = 0.68\,\mathrm{eV}$. By bearing into account the work function of the emitter to be 4.65 eV (see text), the work function of the sample is estimated to be $eV_\Phi = 5.33\,\mathrm{eV}$. c) the $\mathrm{d}I_{cl}\,/\,\mathrm{d}V_{cl}$ curve also does not indicate a difference between the sample and the platinum stripe within the measurement resolution of this experiment. The large FWHM of the $\mathrm{d}I_{cl}\,/\,\mathrm{d}V_{cl}$ is $\pm 0.18\,\mathrm{eV}$ that indicates a polycrystalline sample.

3.4 Summary of Blind Tests and measurement accuracy of the apparatus

The results of the bind test are compiled in table 3.2. The values obtained for "Blind Test 1" and "Blind Test 3" are in good agreement with reported values for polycrystalline samples. However, such values highly depend on the sample preparation methods. The outcome of "Blind Test 2" remains unclear as no experimental values are available for $SrVO_3$ thin films, nor for its uniquely prepared substrate. The system contaminations resulting from "Blind Test 2", emphasize the sensitivity of the measurements, in that they require careful sample preparation.

Moreover, these results indicate that the resolution of the experiments is influenced by the anisotropy of collector material, as previously discussed in chapter 1.2. This influence is evident by comparing the full width at half maximum (FWHM) of the peaks in $\mathrm{d}I_{\mathrm{cl}} / \mathrm{d}V_{\mathrm{cl}}$ plots of the different measurements. For instance, the FWHM of the polycrystalline sample "Blind Test 1" is two times larger than the one of the single crystal sample of the second test. Thus, these measurements can provide qualitative information about the sample structure and homogeneity.

In summary, the results obtained are in good agreement with the reported literature values and show that the designed measurement system and procedure allow for precise work function measurements. The accuracy of the measurements much depends on the anisotropy of the emitter, in addition to

Table 3.2: Summary of blind tests.

Blind Test No.	Material	ϕ_{WF} (eV)	Reported value (eV)	Orientation	Ref.
1	Mo	4.59 ± 0.06	4.6	Polycrys.	[33]
2	$SrVO_3$	4.80 ± 0.06	none	(001)	-
3	Pt	5.33 ± 0.09	5.3 - 5.64	Polycrys.	See table 2.1

the intrinsic uncertainty resulting from the tail of the Fermi-Dirac distribution at elevated temperatures, and the geometry of the grid. However, with the configuration used in this work, the measurement accuracy is expected to be better than 100 meV. This accuracy is also supported by measurements performed on LaB_6 and $SrTiO_3$ samples discussed in the next chapter.

Chapter 4

Work Function Measurements of Novel Materials

This chapter reports on the *in-situ* work-function measurements of polycrystalline LaB_6 thin films, single crystal Nb:$SrTiO_3$ (0.1 wt. %), and $SrRuO_3$ thin films and the heterostructures fabricated to explore the tunability of the work function of $SrRuO_3$. The measurements of LaB_6 thin films and Nb:$SrTiO_3$ have been conducted with a plane tantalum emitter and a grid with a mesh size of $w_{gr} \approx 1.65\,\text{mm}$ (see Fig. 3.7c), and their work functions are determined with respect to the work function of the emitter. However, for the measurements of $SrRuO_3$ thin films and the heterostructures an *in-situ* deposited platinum stripe is used to improve the measurement accuracy and to further calibrating the measurements, as discussed in Sec. 2.2. These measurements were conducted with a low work function emitter and a grid with a fine mesh size of $w_{gr} \approx 240\,\mu\text{m}$ (see Fig. 3.7d). The materials investigated in this chapter have been prepared and fabricated using the epitaxial system discussed in Ch. 3, with their growth parameters summarized in table 4.1. The summary at the end of this chapter focuses mainly on the results from the transition metal oxides and their heterostructures, as these demonstrate unique and previously unexplored properties.

4.1 LaB_6 Thin Films

Introduction

Hexaboride materials demonstrate unique physical properties, such as a Kondo insulating behavior in the case of SmB_6 [71], ferromagnetism in doped CaB_6 and SrB_6 [72, 73], and have a relatively low work function in almost all different compositions. Rare-earth hexaborides, such as LaB_6, are widely used as thermionic and field-emission electron sources. The intrinsically low work function of LaB_6, together with its high-temperature stability at the surface, outperform the thermionic properties of all other rare-earth hexaborides [74]. Doping can further reduce the work function of LaB_6, such as by samarium that is reported to reduce the work function to 1.67 eV [75]. Furthermore, it has been reported that $La_{0.31}Ba_{0.69}B_6$ has a thermionic work function of about 1 eV [76, 77]. Yet, this is disputable when compared to the data of

Table 4.1: PLD parameters of the thin films fabricated in this work. All transition metal oxides were deposited in an oxygen partial pressure of 0.1 mbar. The deposition of LaB_6 thin films was carried-out at $\approx 1 \times 10^{-7}$ mbar.

Material	Substrate	Laser Fluence ($J\,cm^{-2}$)	Temperature[(a)] (°C)
LaB_6	Ta (polycr.)	3.5	450
$SrRuO_3$	Nb:$SrTiO_3$[(b)]	1.2	610
Mono-Capping layer			
$SrTiO_3$	Nb:$SrTiO_3$[(b)]	2	720
$BaTiO_3$	Nb:$SrTiO_3$[(b)]	2	720
$BaZrO_3$	Nb:$SrTiO_3$[(b)]	2	720
$LaAlO_3$	Nb:$SrTiO_3$[(b)]	1.6	720

(*a*) Temperature values are nominal due to different emissivities.
(*b*) Single crystal, (001) orientation, Nb dopant concentration of 0.5 wt.%.

Futamoto [74], who also investigated the effect of Ba doping with a different concentration and reports on a work function of $2.99 \pm 0.03\,\mathrm{eV}$.

Results

Figure 4.1 shows the results obtained for the LaB_6 thin films prepared in this work. The emitter used in this experiment was a polycrystalline Ta metal emitter with a measured work function of 4.28 eV, as discussed in Sec. 3.2.1. The $I(V)$ curves indicate the occurrence of two band alignments during the voltage sweeps. From the logarithmic plot of the $I_{\mathrm{cl}}(V_{\mathrm{cl}})$ curve (Fig. 4.1b), the first band-alignment happens at $eV_{\Phi}^{1} = -1.52\,\mathrm{eV}$ and the second at $eV_{\Phi}^{2} = 0.54\,\mathrm{eV}$, which yields two work functions of 2.76 eV and 4.82 eV, respectively. Although the range where the first band-alignment takes place and the corresponding Φ_{WF} are in the expected range, the origin of the second current rise is not understood.

The work function resulting from the second band alignment does not correspond to pure lanthanum ($\Phi_{\mathrm{WF}}^{\mathrm{La}} = 3.3\,\mathrm{eV}$, [33]), and hardly matches the reported value for polycrystalline boron ($\Phi_{\mathrm{WF}}^{\mathrm{B}} = 4.45\,\mathrm{eV}$, [33]). However, as work function values for boron are not widely reported in the literature, a conclusive statement is not possible. Another possible explanation for this band alignment is the rise of the collector potential, as the total potential of the collector ($eV_{\mathrm{cl}} + \phi_{\mathrm{cl}}$) becomes comparable to the work function of the tungsten grid ($\Phi_{\mathrm{WF}}^{\mathrm{Polycr.–W}} \approx 4.55\,\mathrm{eV}$, [33]). As a result, more electrons would be attracted away from the grid, that could be additionally enhanced by the large mesh size (see Fig. 3.7c). However, more investigations are required for a conclusive statement.

Considering the above, the work function of LaB_6 thin films prepared in this work is found to be 2.76 eV. The crystal orientation of these thin films was determined by X-ray diffraction measurements. These measurements indicate a dominant (110) orientation, with (211) admixtures, as shown in Fig. 4.2. The intensity of the (211) peak is remarkably high when compared to the (110) peak by considering the structure factor of the compound. The work function of these two facets of LaB_6 are found to be similar in the

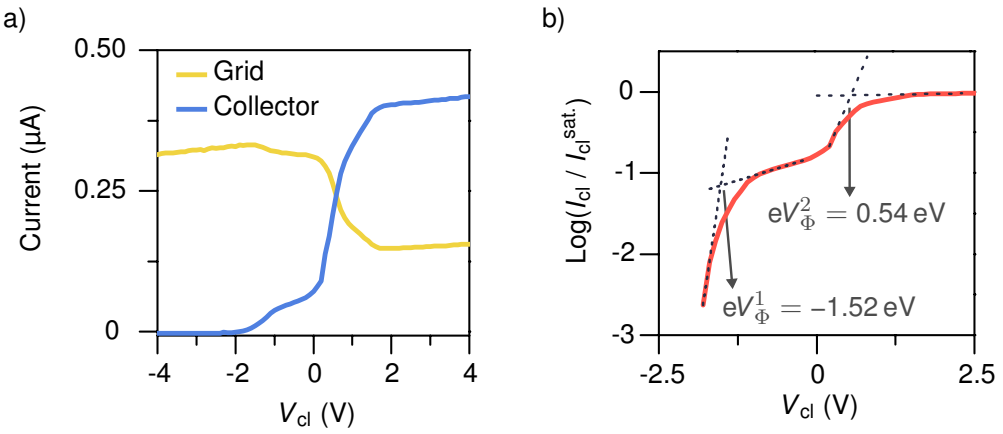

Figure 4.1: Measurement results of a LaB_6 thin film at $T_{em} = 1475\,K$ and $V_{gr} = 35\,V$. a) Grid and collector current as a function of the collector voltage. b) The logarithmic plot of $I_{cl}\,(V_{cl})$ for band-alignment voltage (eV_{Φ}) determination. The band-alignments takes place at $eV_{\Phi}^{1} = -1.52\,eV$ and $eV_{\Phi}^{2} = 0.54\,eV$. In this experiment a Ta emitter is used with $\Phi_{WF} = 4.28\,eV$.

experiments of H. Liu *et al.* ($\Delta\Phi_{WF}^{(110)-(211)} \leq 50\,meV$) [78].

Table 4.2 compares the obtained value with the reported ones found in the literature for the (110) and (211) orientations. The value obtained here is a good agreement with the literature. Nevertheless, this value is independently confirmed by the Richardson method by using these films as thermionic emitters. These measurements will be presented in the Ph.D. thesis of R. Wanke.

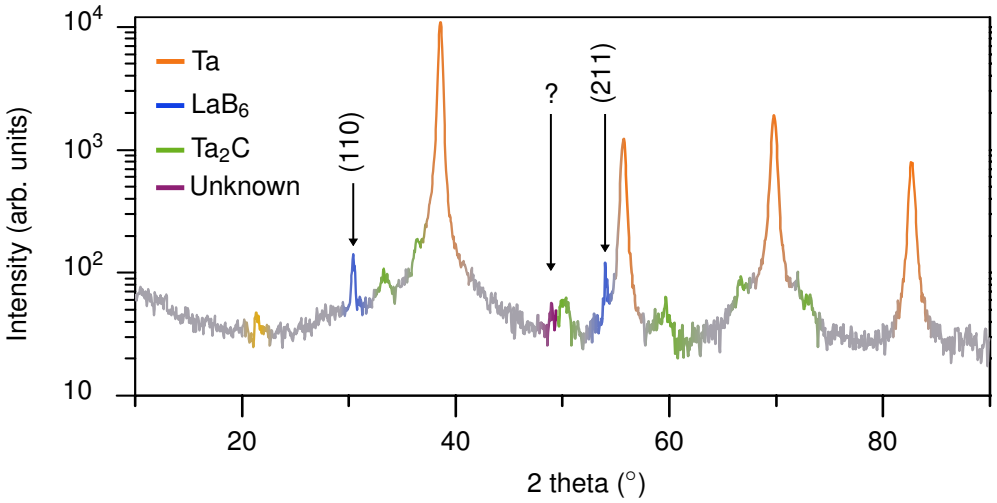

Figure 4.2: Grazing incidence diffractogram of a LaB_6 thin film grown by PLD on a polycrystalline Ta substrate. The peaks at $2\theta = 30.5°$ and $2\theta = 54°$ correspond to the (110) and (211) orientations of LaB_6, respectively (highlighted in blue). The peak corresponding to the (100) orientation would be expected at $2\theta = 21.4°$ (highlighted in yellow). The origin of the peak at $2\theta = 48.9°$ is unknown. The obtained diffractogram might not be conclusive as surface oxidation and the formation of La_2O_3 is likely due to the volatile nature of lanthanum and the deposition technique used for the growth [79].

Table 4.2: Comparison of work function values of LaB_6 obtained in this work with reported values found in literature.

$\Phi_{WF}^{LaB_6}$ (eV)	Method	Ref.	Orientation
2.76	Retarding field	This work	(110) & (211)
2.68	Thermionic	[80]	(110)
2.5	UPS	[81]	
2.73	Thermionic - Schottky emission	[78]	
2.94	Model calculation	[82]	
2.72	Thermionic - Schottky emission	[78]	(211)
2.8	Model calculation	[82]	
2.54	Model calculation	[78]	

4.2 Nb:$SrTiO_3$ (0.1 wt. %)

Introduction

$SrTiO_3$ is one of the most studied perovskites. This wide band-gap insulator demonstrates unique physical properties, such as superconductivity at 300 mK [83], and a two-dimensional electron system at its interface with $LaAlO_3$ [39] that is also a band insulator. Besides, $SrTiO_3$ has a lattice constant of 3.90 Å at room temperature that makes it a preferred substrate material for oxide electronics. This compound can be doped by metals such as niobium (Nb) or lanthanum (La) to obtain semi-metallic properties [84]. Here, we investigate the work function of a Nb:$SrTiO_3$ (0.1 wt. %) single crystal, with a (001) orientation. This investigation is essential since $SrTiO_3$ is the substrate of choice throughout this work. Furthermore, the results serve as a calibration measurement as the work function of this material is already reported in the literature.

Results

The single crystal Nb:$SrTiO_3$ (001) samples used in this work were etched with a buffered hydrofluoric (HF) acid solution to obtain a TiO_2 terminated surface [85]. The procedure used in this work is discussed in detail in Ref. [21]. Figure 4.3 shows a typical AFM image of a Nb:$SrTiO_3$ sample after this etching procedure. Before the work function measurements, the sample was annealed in the epitaxial system to ensure a clean surface, and afterwards transported *in-situ* to the measurement apparatus.

Annealing was done in an oxygen background pressure of $pO_2 \approx 0.1$ mbar, at a nominal temperature of 800 °C. During this process, the surface quality of the sample was monitored by RHEED. After 30 min the intensities of the diffraction spots saturated. The pressure during the entire sample transport process did not exceed 3×10^{-8} mbar for this sample.

The $I(V)$ curve of a single crystal Nb:$SrTiO_3$ (001) sample with a nominal dopant concentration of 0.1 wt. % is presented in Figure 4.4. From the logarith-

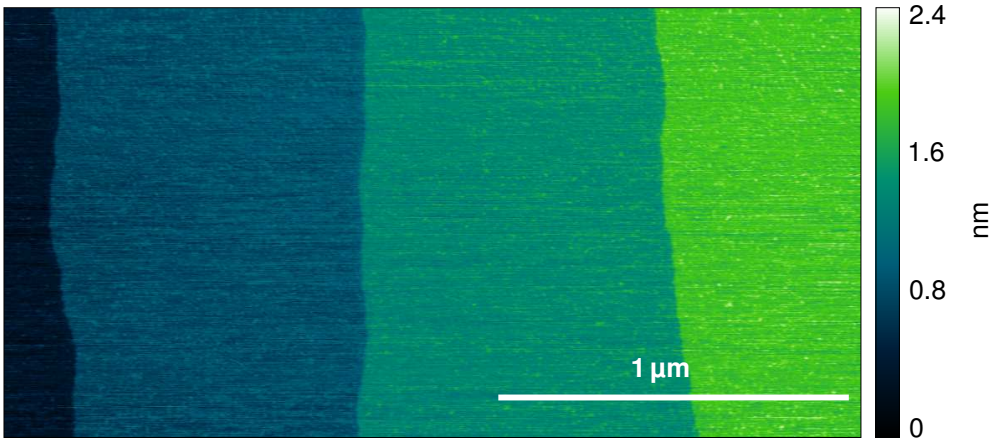

Figure 4.3: Typical AFM image of a single crystal Nb:$SrTiO_3$ (0.5 wt. %), with a (001) orientation after the etching procedure. This procedure is performed to obtain an atomically flat TiO_2 termination on the surface.

mic plot, the band alignment voltage is estimated to occur at $eV_\Phi = +0.13\,\text{eV}$. By taking into account the work function of the Ta emitter used for this measurement ($\Phi_{\text{WF}}^{\text{Ta}} = 4.28\,\text{eV}$, see Fig. 3.10), the work function of Nb:$SrTiO_3$ (0.1 wt. %) is determined to be 4.41 eV in this work.

Susaki *et al.* [17] have investigated the work function of Nb:$SrTiO_3$ *in-situ* by Kelvin probe measurements. Their measurements indicate that the work function of $SrTiO_3$ depends on the oxygen background pressure used during the annealing procedure. This dependency is shown in Fig. 4.4c. Additionally, they report on the value of the SrO-termination of $SrTiO_3$ that has a work function of about 2.4 eV. Furthermore, model calculations done by Zhong and Hansmann [37] predict similar values for both terminations of $SrTiO_3$, 4.48 eV for the TiO_2 and 1.92 eV for the SrO termination. Considering these, the value obtained here agrees well with both the model calculations and the *in-situ* Kelvin probe measurements.

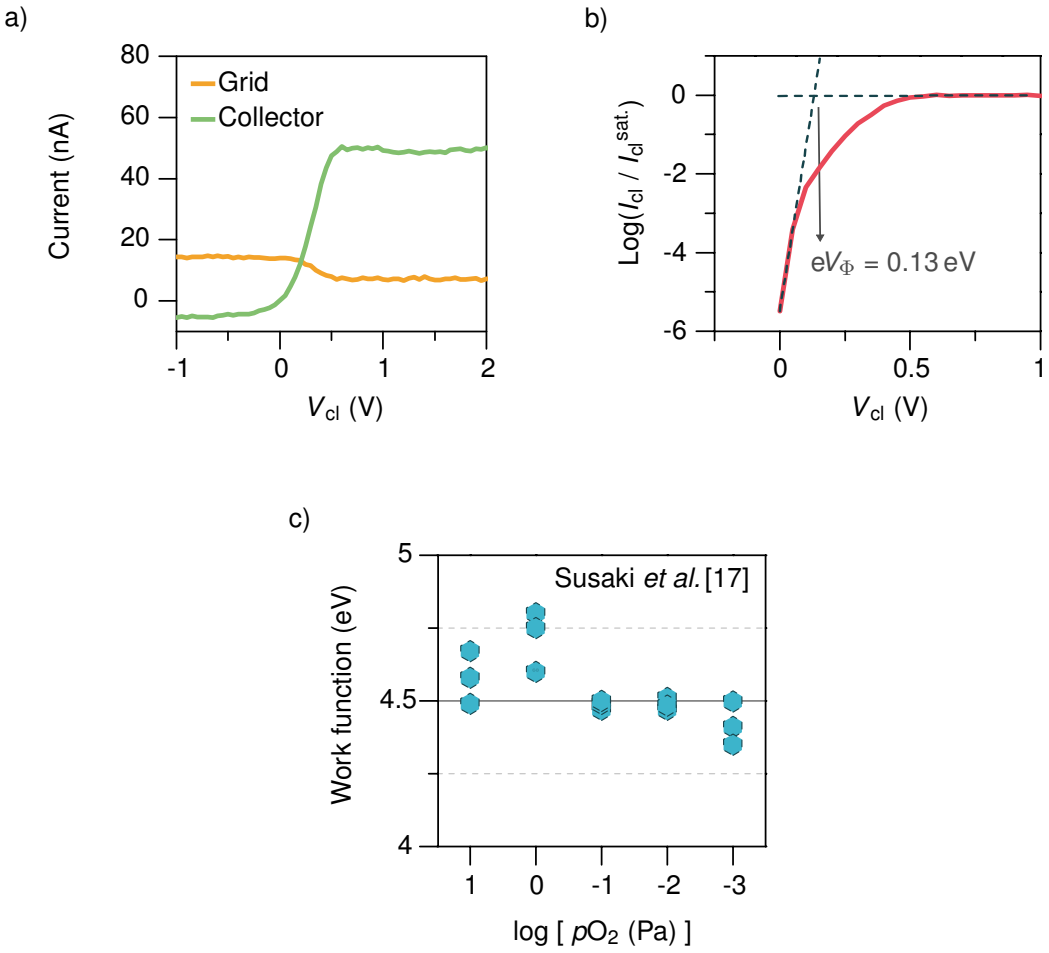

Figure 4.4: Work-function results of a TiO_2-terminated Nb:$SrTiO_3$ (0.1 wt. %) sample at $T_{em} = 1475\,K$ and $V_{gr} = 15\,V$. Panel a) shows the $I(V)$ curves obtained by varying the collector voltage. Panel b) shows the logarithmic plot of I_{cl} as a function of V_{cl}. The band alignment is found to occur at $eV_\Phi = +0.13\,eV$ corresponding to a work function of 4.41 eV ($\Phi_{WF}^{Ta} = 4.28\,eV$, see Fig. 3.10). Panel c) illustrates the Kelvin probe measurements of Susaki *et al.* for a TiO_2-terminated Nb:$SrTiO_3$, annealed at different oxygen partial pressures. Figure reproduced with permission.

4.3 $SrRuO_3$

Introduction

$SrRuO_3$ is a correlated material system with unique physical properties. It is highly metallic and has a lattice constant well-matching $SrTiO_3$. Due to these properties $SrRuO_3$ is frequently used as contact electrode in oxide electronics [84, 86]. Hence, investigating $SrRuO_3$ for its work function, next to its high-temperature properties in reducing conditions are essential tasks. The growth dynamics of $SrRuO_3$ on $SrTiO_3$ by PLD has been widely discussed as $SrRuO_3$ is highly sensitive to the growth conditions [87]. Figure 3.3 shows the RHEED oscillations obtained for $SrRuO_3$ in a layer-by-layer growth mode. The measurements presented below are conducted on a sample with a thickness of ∼24 unit cells unit cells.

Results

As mentioned at the beginning of this chapter, the *in-situ* work function measurements of the $SrRuO_3$ thin films are performed with a low work-function emitter and a grid with a fine mesh size ($w_{\mathrm{gr}} = 240\,\mu\mathrm{m}$, see Fig. 3.7d). The measurements described in the following have been performed at different temperatures starting from $T_{\mathrm{em}} = 1100\,\mathrm{K}$ to $T_{\mathrm{em}} = 1220\,\mathrm{K}$ to examine the behavior of these thin films at different temperatures. Moreover, by this temperature rise the effective work function of the emitter can directly be measured and used for the work function determination of the reference platinum stripe.

Figure 4.5 compares two of the obtained $I(V)$ curves, one at $T_{\mathrm{em}} = 1110\,\mathrm{K}$ from the initial measurements and the other at $T_{\mathrm{em}} = 1050\,\mathrm{K}$ that is the last measurement after cooling the emitter from 1220 K. The $I_{\mathrm{cl}}(V_{\mathrm{cl}})$ curves indicate the coexistence of two work functions arising from the platinum reference material and the $SrRuO_3$ thin film, evident from their relative current amplitudes. Surprisingly, it was found that with time and by increasing temperature, the band-alignment positions (eV_{Φ}) for both the reference

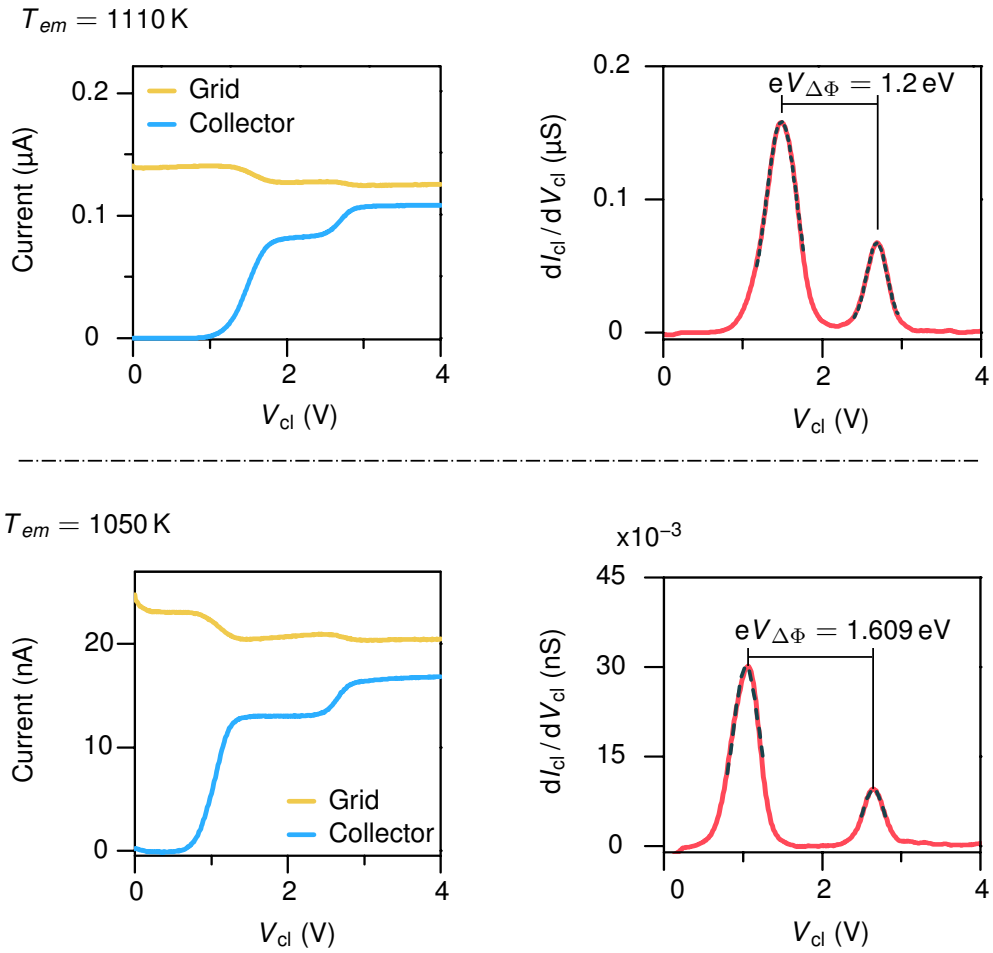

Figure 4.5: Example of two $I(V)$ curves obtained for a 24 unit cell $SrRuO_3$ sample grown on a Nb:$SrTiO_3$ (0.5 wt. %) substrate. The measurement on top is performed after ≈100 min, and the one on the bottom after ≈330 min after cooling down the emitter from $T_{em} = 1220$ K. In both measurements $V_{gr} = 35$ V. The temperature of the collector is measured by pyrometer to be <570 K

platinum stripe and the one of $SrRuO_3$ varied. The difference between the band-alignment voltage of the platinum reference material and the $SrRuO_3$ thin film ($eV_{\Delta\Phi}^{\mathrm{Pt–SrRuO_3}}$) is found to be 0.78 eV initially and increases gradually to 1.62 eV even after cooling the emitter to 1050 K. A summary of this change is shown in Fig. 4.6. The temperature of the $SrRuO_3$ thin films was measured using a pyrometer as $T_{\mathrm{cl}} < 570\,\mathrm{K}$ at the end of the measurements. However, this is considered to be the upper limit of T_{cl} as the error resulting from thermal radiations of the filament is inevitable. The reason for the variation of the band-alignment voltages is unclear, but we will discuss below possible effects that might influence this work-function reduction.

One possible scenario explaining the observed drift is the evaporation of contaminants from the surface, that alter the surface dipoles. However, this large and gradual change of the work function cannot be explained by this effect. This is reasoned by the relatively constant and small FWHM of the $SrRuO_3$ peaks in the obtained $\mathrm{d}I_{\mathrm{cl}} / \mathrm{d}V_{\mathrm{cl}}$ curves (see Fig. 4.5).

Another explanation might be the evaporation of RuO_2 that would result in a termination switch, *e.g.*, from RuO_2 to SrO or vice versa. However, no evidence of this is observed in the residual mass spectrum during the experiments, as shown in Fig. 4.7. Moreover, this change would neither be gradual nor constant over the entire sample surface. Also, the plateau at $T_{\mathrm{em}} = 1110\,\mathrm{K}$ where the band-alignment difference is comparatively constant over several measurements cannot be explained by the change of surface termination (see Fig. 4.6). Besides, AFM images of the measured samples are identical to fabricated samples and no change of the surface morphology is observed, as shown in Fig. 4.18b. Furthermore, surface reconstructions are unlikely as well as the temperature needed for such processes are relatively high, and would even less likely take place over the entire emission area at once ($A_{\mathrm{em}} > 38\,\mathrm{mm}^2$), considering the nonuniform temperature profile of the collector.

A more likely explanation is surface relaxation mechanism, considering the thermochemical properties of RuO_2. Model calculations performed by Z. Zhong and P. Hansmann [37] suggest that these mechanisms have a large impact on the work function of transition metal oxides and can indeed change

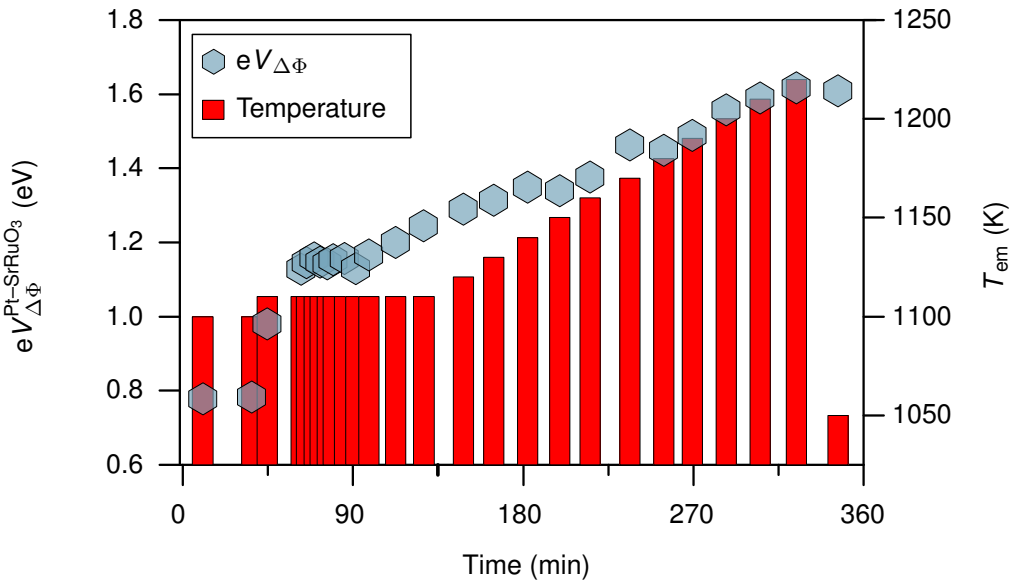

Figure 4.6: Evolution of the band-alignment voltage difference ($eV_{\Delta\Phi}$) during the measurements of a $SrRuO_3$ thin film with the reference platinum stripe as a function of time and increasing T_{em}. In all measurements $V_{gr} = 35\,V$.

it by about 1 eV. Indeed, this process could take place gradually over time and depends on temperature and time. Additionally, considering the reducing conditions in our measurements, this mechanism might be even enhanced. Considering these, we try to provide an absolute value for both the platinum reference stripe and the $SrRuO_3$ thin films below.

As the temperature of the emitter increases during the experiments in well-defined steps, its effective work function can be determined by the Richardson method, as shown in Fig. 4.8. The work function of the emitter is found to be $2.73 \pm 0.02\,eV$ with a remarkably small Richardson constant of $A_{RD} = 1.34\,A\,K^{-2}\,cm^{-2}$. Note that this estimation stems from the narrow temperature range and moderate voltages used during the experiments. Thus, we refer to this as an effective work function value of the emitter (ϕ_{em}^{eff}). As discussed in Sec. 2.2, the absolute values are determined from the ϕ_{em}^{eff} and the relative band-alignment position of the reference material. The eV_{Φ}^{Pt} is estimated from the repeating measurements at $T_{em} = 1110\,K$ to be $eV_{\Phi}^{Pt} = 2.90 \pm 0.01\,eV$, that corresponds to a work func-

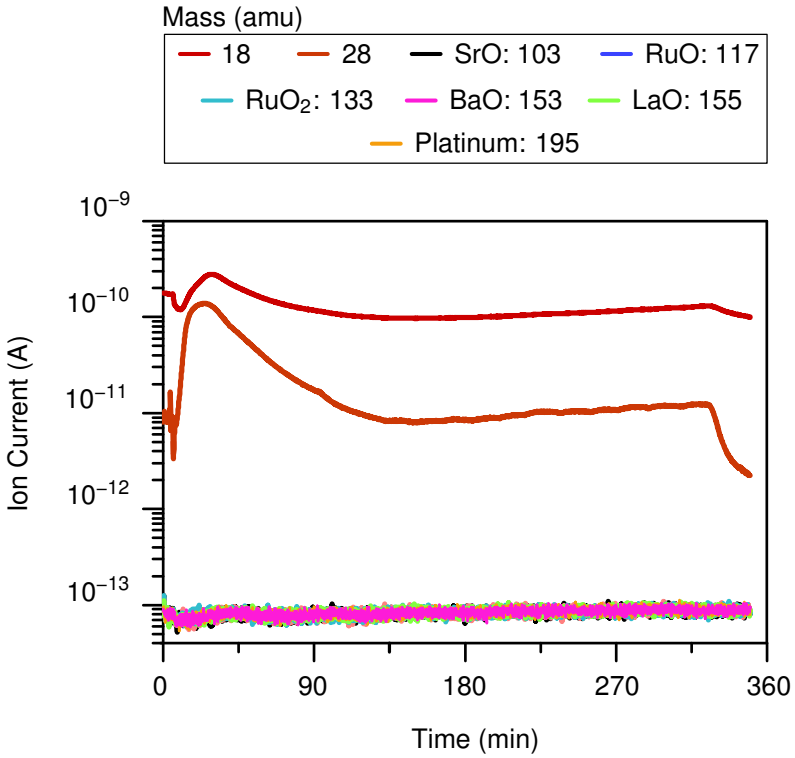

Figure 4.7: Residual mass spectrum during the measurement period of a $SrRuO_3$ thin film. No sign of the evaporation of RuO_2 or SrO is observed.

tion of $\Phi_{\mathrm{WF}}^{\mathrm{Pt}} = 5.63 \pm 0.03\,\mathrm{eV}$. In these experiments, we only consider the error margin for determining eV_{Φ}^{Pt} and ignore the effects of height adjustments during the experiments that alters all eV_{Φ}. The uncertainty in the determination of the individual peak positions in each measurement ($\mathrm{d}I_{\mathrm{cl}} / \mathrm{d}V_{\mathrm{cl}}$) is typically below 5 meV and is thus neglected. Thus we estimate here only the shift of eV_{Φ}^{Pt} in the individual measurements as our error margin.

For $SrRuO_3$, there are two ways to determine the absolute value of its work function: a) To estimate it relative to the platinum peak, and b) to estimate it directly from the emitter work function. Considering the previously discussed $eV_{\Delta\Phi}^{\mathrm{Pt\text{–}SrRuO_3}}$ that ranges from 0.78 eV to 1.62 eV, the work function of this $SrRuO_3$ thin film is $4.85 \pm 0.03\,\mathrm{eV}$, reducing over time and with temperature to $4.01 \pm 0.03\,\mathrm{eV}$. A direct estimate of its work function from $\phi_{\mathrm{em}}^{\mathrm{eff}}$ results in $\Phi_{\mathrm{WF}}^{\mathrm{SrRuO_3}} = 5.07 \pm 0.02\,\mathrm{eV}$ that reduces gradually to $4.03 \pm 0.02\,\mathrm{eV}$ over time. However, the direct estimation is disputable because the height adjustments

of the collector during the experiments alter the eV_Φ values but not ϕ_{em}^{eff}. Thus, we only consider the $\Phi_{WF}^{SrRuO_3}$ values that are calibrated using the reference platinum stripe.

Table 4.3 compares the obtained results with the one found in literature. Experimental values for the work function of $SrRuO_3$ are not widely reported at the time of this thesis. The value obtained here is close to the experimental results of Fang *et al.* (5.2 eV) [88] and the model calculations of Jacobs *et al.* (5.16 eV) [38], and in good agreement with the value of Zhong and Hansmann [37] (4.88 eV) for the RuO_2 termination of $SrRuO_3$. This general agreement with the model calculations suggest a BO_2 termination for these $SrRuO_3$ thin films. This is surprising as it contradicts the RHEED analysis by Rijnders *et al.* that predict a SrO-termination for $SrRuO_3$ thin films fabricated by PLD [87]. This information about the termination of these $SrRuO_3$ thin films is helpful to explore tunability of its work function by the various capping layers, as presented in the next section.

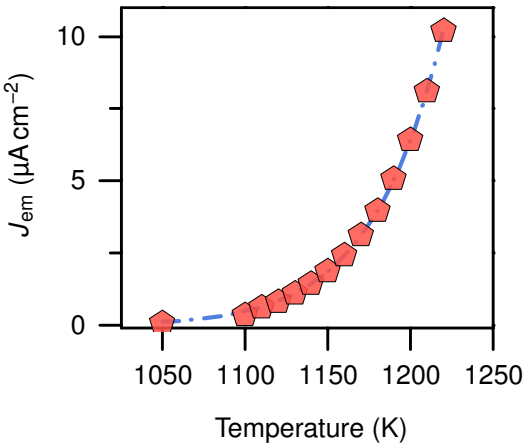

Figure 4.8: Total emission current of the emitter at different temperatures, obtained during the $SrRuO_3$ thin film measurement. The fit to the Richardson equation (dashed blue curve, see Eq. 2.3) results in $\phi_{em} = 2.73 \pm 0.02$ eV.

Table 4.3: Comparison of the reported work function values of (001) $SrRuO_3$ with values obtained in this work.

$\Phi_{WF}^{SrRuO_3}$ (eV)	Method	Termination	Ref.
4.85 to 4.01	Retarding potential	BO_2	This work
5.2	Electrical	Unknown	[88]
5.16	DFT model calculations	BO_2	[38]
2.55	DFT model calculations	AO	[38]
4.88	DFT model calculations	BO_2, Relaxed	[37]
3.9	DFT model calculations	BO_2, Unrelaxed	[37]
2.39	DFT model calculations	AO, Relaxed	[37]
1.3	DFT model calculations	AO, Unrelaxed	[37]

4.4 Work Function Tailoring by Monolayers of Perovskites

Introduction

The tunability of the work function of $SrRuO_3$ thin films are explored in this section using several epitaxial capping-layers with a thickness of one-unit-cell. All capping layers investigated here are insulators with a band gap of more than 3 eV and a lattice constant suitable for epitaxial growth on $SrRuO_3$. The lattice constants of these perovskites are compared in table 4.4. These capping layers were chosen to substitute the atoms of the last unit cell on the $SrRuO_3$ surface. Figure 4.9 shows a schematic of the different heterostructures examined in this section.

Considering the results of the previous section that hint to a BO_2-termination for the $SrRuO_3$ thin films, the $SrTiO_3$ exchanges ruthenium with titanium on the last layer, similar to the $BaTiO_3$ capping layer. However, the $BaTiO_3$ capping layer additionally exchanges Sr with Ba at the interface. This difference at the interface can provide an insight on interface effects, *e.g.*, charge transfer and compressibility on the surface dipoles (see Sec. 2.1). Moreover, the $BaZrO_3$ capping layer only changes the titanium with zirconium

Table 4.4: Room-temperature lattice constants and mismatches of the capping layers used in this work. Data from Ref. [89]. Lattice mismatch is calculated by $\frac{|a-a_{SrRuO_3}|}{a_{SrRuO_3}}$.

Material	Lattice constant (Å)	Lattice mismatch
$SrRuO_3$	3.93	-
$SrTiO_3$	3.90	0.6 %
$BaTiO_3$	4.01	1.7 %
$BaZrO_3$	4.19	6.6 %
$LaAlO_3$	3.77	4 %

on the last layer and provides a direct comparison to the $BaTiO_3$ capping layer. Finally, the effect of a polar capping layer is examined separately by one unit cell of $LaAlO_3$. This approach for work-function tuning is interesting as polar interfaces and materials demonstrate unanticipated phenomenons.

The deposition parameter window of the capping layers was kept as close to each other as possible (see table 4.1). The oxygen background pressure during the growth of $SrRuO_3$ thin films and all capping layers was kept the same due to the sensitivity of $SrRuO_3$ on the variation of this parameter. Besides, the deposition temperature of the capping layers was kept at 720 °C. Only the fluence of the ablation laser was tuned and optimized for their epitaxial growth. By this approach, the deposition of the capping layers is performed on nominally similar $SrRuO_3$ thin films to obtain qualitatively comparable results. The transmission electron microscopy (TEM) images of these capping layers show a sharp interface in these heterostructures (see Fig. 4.10). All capping layers are deposited on (001) $SrRuO_3$ thin films with a thickness of more than 20 unit cells. After the epitaxial growth of the heterostructures, a platinum stripe is evaporated on them *in-situ* for calibrating the measurements (see Sec. 2.2).

The results in this section are split into two parts, based on the effect of these monolayers on the work function of the $SrRuO_3$ thin films. First, result from the $SrTiO_3$ and $BaTiO_3$ capping layer are presented which reduce the work function. Afterward, the $LaAlO_3$ and $BaZrO_3$ monolayers are presented which increase it. These results are compared in the summary of this chapter.

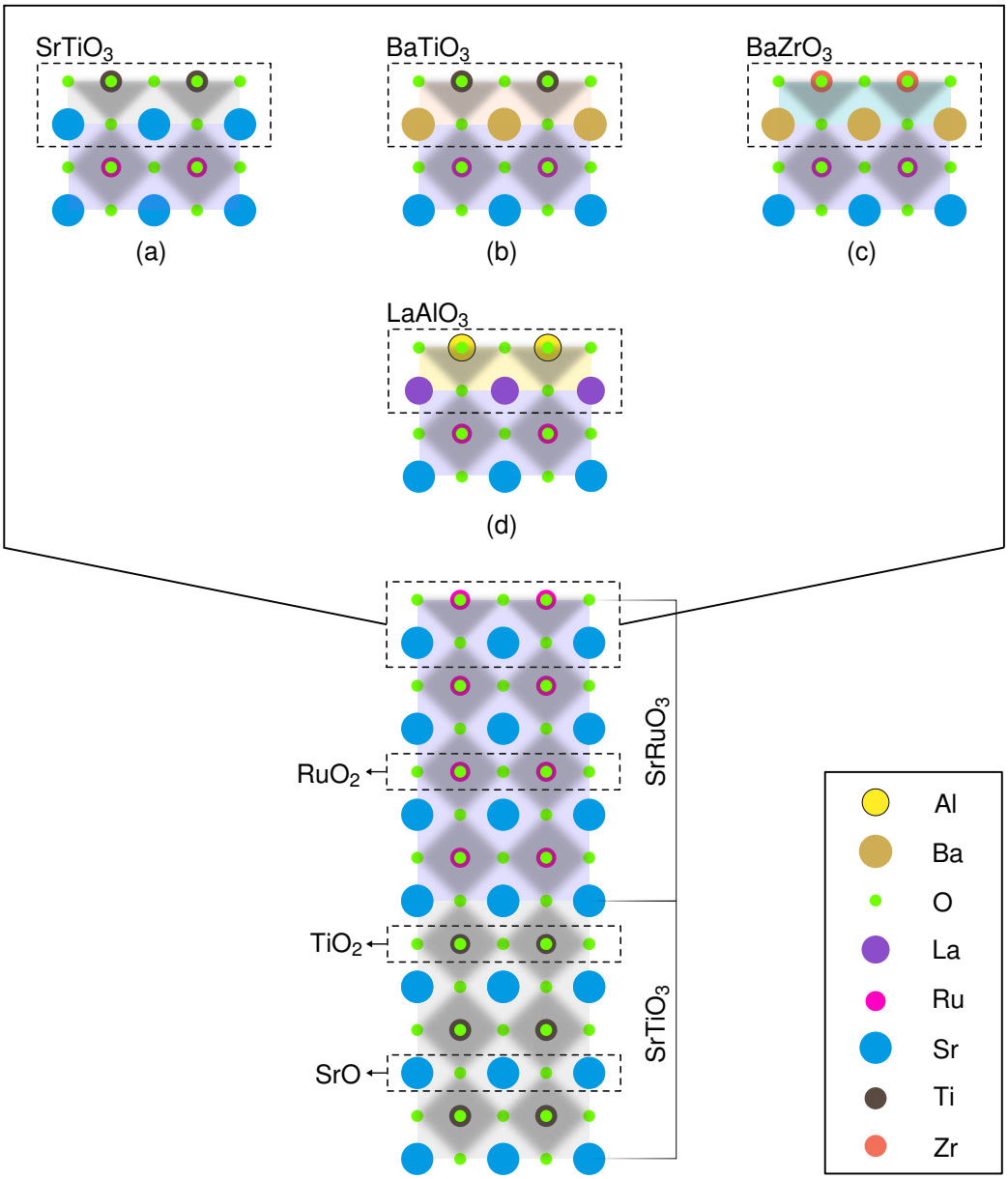

Figure 4.9: Sketch of the heterostructures investigated in this work. Bottom shows a $SrTiO_3$ substrate with a $SrRuO_3$ thin film on top. The various capping layers shown above were chosen to exchange the *A*- or *B*-atom of the last layer. The $SrTiO_3$ capping layer exchanges the *B*-atom from Ru to Ti, keeping the strontium unchanged. The $BaTiO_3$ capping layer swaps the *A*-atom from Sr to Ba as Ti is unchanged in (a) and (b). Additionally, the *B*-atom is again altered from Ti to Zr by the $BaZrO_3$ capping layer with Ba being the same *A*-atom in (b) and (c). The effect of a polar capping layer is investigated separately by a $LaAlO_3$ capping layer. The atomic sizes and distances are arbitrary and do not represent physical values.

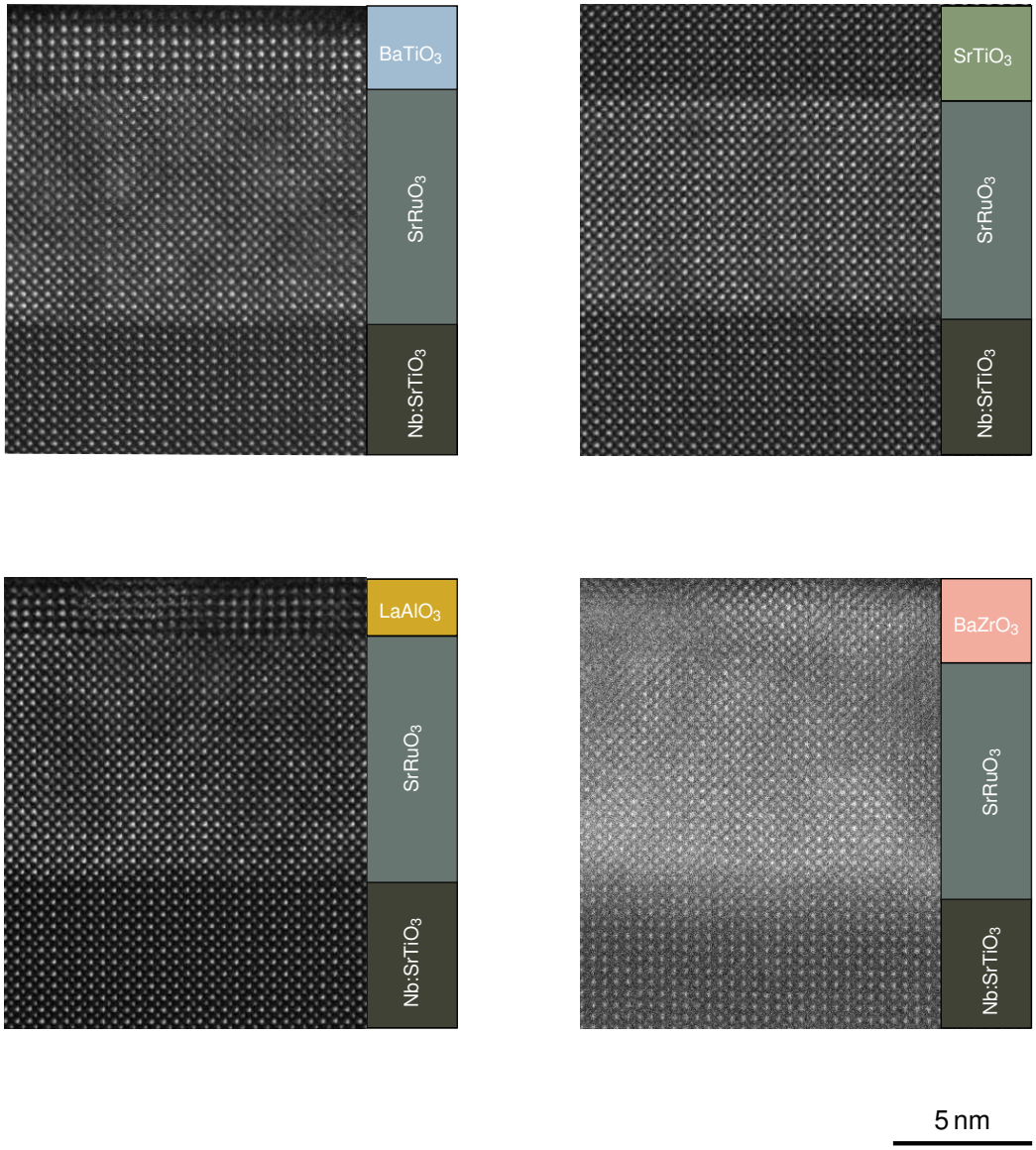

Figure 4.10: HAADF-STEM images of the heterostructures investigated in this work, illustrating sharp interfaces for the majority of the heterostructures. Preliminary EELS and EDX analyses suggest a BO_2 termination for these capping layers (not included here). Imaging performed by V. Srot form *Stuttgart Center for Electron Microscopy (StEM)* using an *JEOL* ARM200F [90] at 200 kV, equipped with a cold field-emission gun and a DCOR probe Cs-corrector from *CEOS* [91].

4.4.1 Results I: $BaTiO_3$ and $SrTiO_3$ monolayers

Example measurement curves of the $BaTiO_3$ and $SrTiO_3$ capping layers are shown in Fig. 4.11 and 4.12. The $I_{\mathrm{cl}}(V_{\mathrm{cl}})$ curves of these heterostructures exhibit a third current rise, in addition to those resulting from the reference platinum stripe and the primary sample. This additional feature results in a peak on the shoulder of the main peak in the $\mathrm{d}I_{\mathrm{cl}}/\mathrm{d}V_{\mathrm{cl}}$ curves. The origin of this peak is not understood, but their band-alignment voltages (eV_Φ) with respect to the reference platinum stripe (eV_Φ^{Pt}) suggests that they result from an incomplete surface coverage, *i.e.*, the $SrRuO_3$ thin film. This feature is surprising, as the TEM images suggest a sharp interface in these heterostructures (see Fig. 4.10).

The RHEED pattern obtained after deposition of these heterostructures is shown in Fig. 4.13. The pattern of the $BaTiO_3$ capping layer suggests smooth and homogeneous surface. However, the pattern of the $SrTiO_3$ capping layer hints to a 3-dimensional growth that could result in an incomplete surface coverage. Nevertheless, a correlation between the number of laser ablation pulses with the height of this shoulder-peak was observed. These results indicate that the work function measurements can provide unique information about the growth process in addition to RHEED monitoring.

Similar to the $SrRuO_3$ thin films, the band-alignment voltage corresponding to the heterostructures changed over time and with temperature, as shown in Fig. 4.14. This trend is also observed for the previously discussed shoulder peak in the $\mathrm{d}I_{\mathrm{cl}}/\mathrm{d}V_{\mathrm{cl}}$ curves (see Fig. 4.11c and 4.12c). The band-alignment voltage difference between the reference platinum stripe and the primary peak ($eV_{\Delta\Phi}^{\mathrm{Pt–Het}}$) increases from an initial value of 1.66 eV to 2.2 eV and from 1.9 eV to 2.1 eV for the $BaTiO_3$ and $SrTiO_3$ capping layer, respectively. The band-alignment voltages of the reference platinum stripe (eV_Φ^{Pt}) is at 3.10 ± 0.02 eV for the $BaTiO_3$, and at 3.40 ± 0.07 eV for the $SrTiO_3$ capping layer.

The effective work function of the emitter is found to be 2.83 ± 0.02 eV and 2.57 ± 0.03 eV referring to the measurements of the $BaTiO_3$ and the $SrTiO_3$ capping layer, respectively. The work functions of the reference platinum

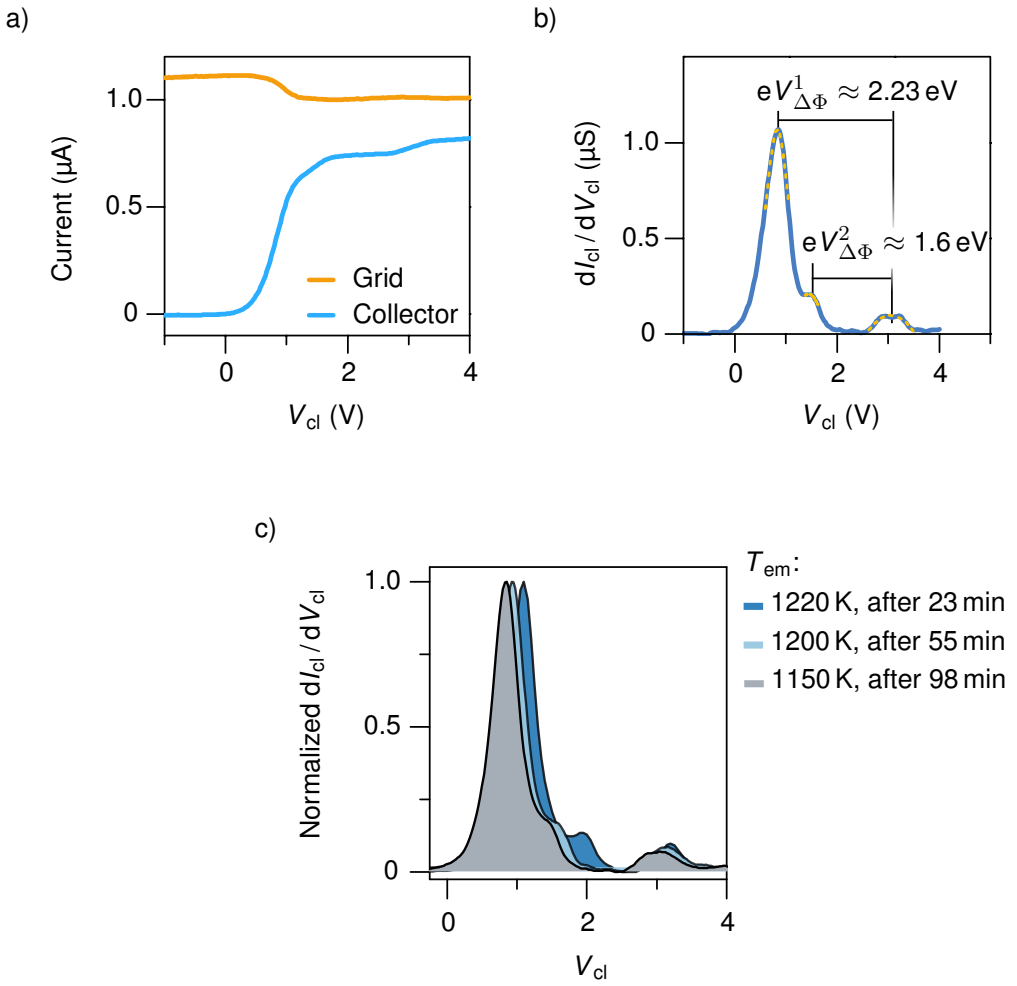

Figure 4.11: Panel a) shows an $I(V)$ curve of a $SrRuO_3$ thin film with a 1 uc $BaTiO_3$ capping layer after 115 min at $T_{em} = 1200$ K, and panel b) the corresponding dI_{cl}/dV_{cl} curve. The measurement curves exhibit an additional current rise that results in a peak on the shoulder of the dI_{cl}/dV_{cl} curves. Panel c) shows different dI_{cl}/dV_{cl} curves at different temperatures and time. The shoulder peak follows the same trend as $eV^{\text{Pt–BTO Het}}_{\Delta\Phi}$ and its band-alignment voltage changes over time with temperature. In all measurements $V_{gr} = 35$ V.

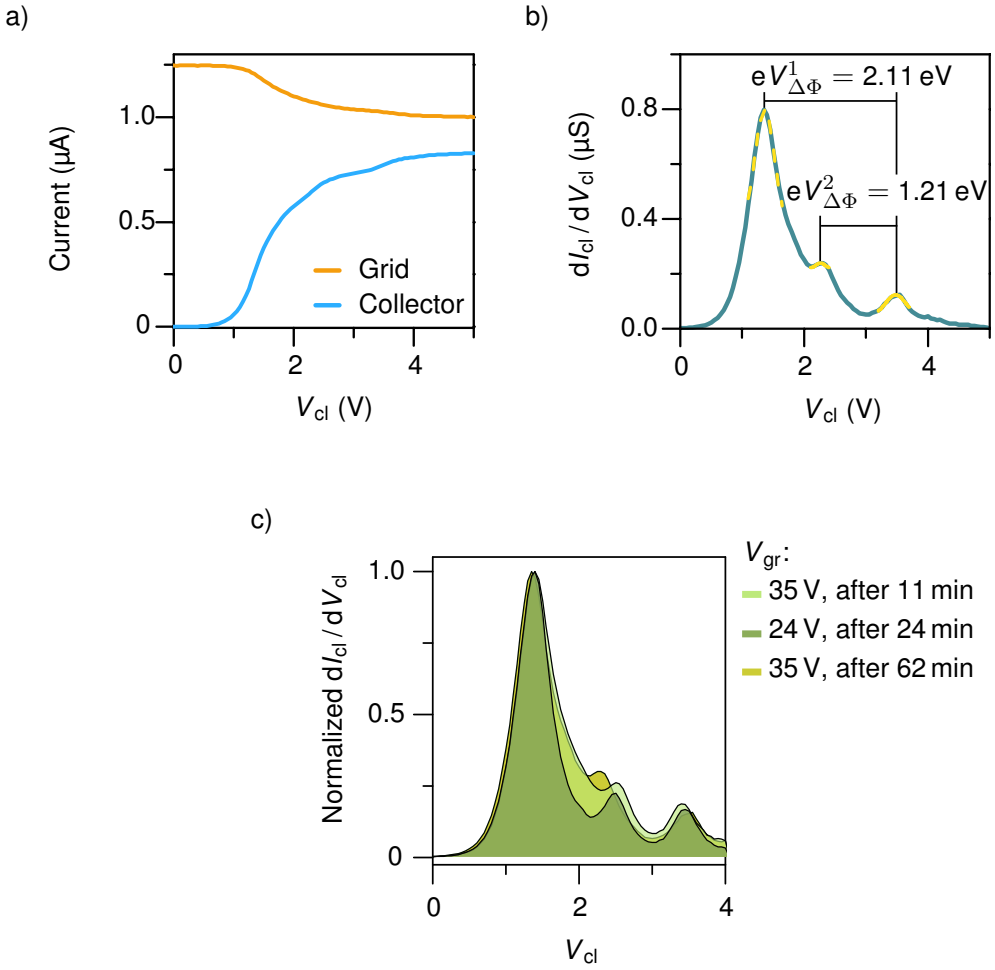

Figure 4.12: Panel a) shows an $I(V)$ curve of 1 uc $SrTiO_3$ monolayer on a $SrRuO_3$ thin film after 63 min at $V_{gr} = 35\,V$, and panel b) the corresponding dI_{cl}/dV_{cl} curve. The measurement curves exhibit an additional current rise that results in a peak on the shoulder of the dI_{cl}/dV_{cl} curves. Panel c) shows different dI_{cl}/dV_{cl} curves at different grid voltages and time. The shoulder peak follows the same trend as $eV^{\text{Pt–STO Het}}_{\Delta\Phi}$ and its band-alignment voltage changes over time. In all measurements $T_{em} = 1220\,K$.

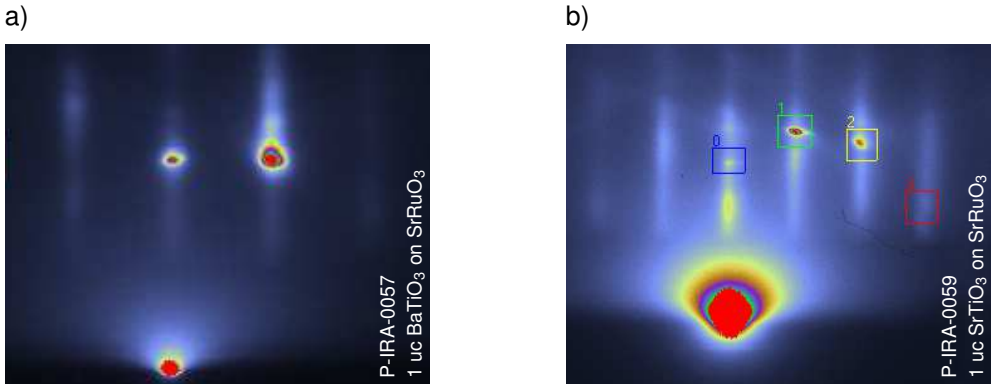

Figure 4.13: RHEED pattern after the deposition of a one unit cell thick layer of a) $BaTiO_3$ and b) $SrTiO_3$ on a $SrRuO_3$ thin film.

stripe therefore result as $5.93 \pm 0.04\,\mathrm{eV}$ and as $5.97 \pm 0.10\,\mathrm{eV}$ for the $BaTiO_3$ and $SrTiO_3$ measurements respectively. The large error margin results from the shift of the peak corresponding to the reference platinum stripe in the individual $\mathrm{d}I_{\mathrm{cl}} / \mathrm{d}V_{\mathrm{cl}}$ curves (See Fig. 4.14). The excellent agreement of $\Phi_{\mathrm{WF}}^{\mathrm{Pt}}$ in these heterostructures next-to its large value compared to the $SrRuO_3$ thin film further suggest similar surface chemistry that would be an indication for common BO_2 termination in these thin films.

The work function results of these heterostructures are abstracted in table 4.5. The work function measurements of the $SrTiO_3$ capping layer were obtained after an initial calibration procedure that took 20 min at $T_{\mathrm{em}} = 1220\,\mathrm{K}$. Considering the time and temperature dependence of these measurements, the upper value of its work function might be comparable to the one of the $BaTiO_3$ capping as the lower values are.

Table 4.5: Work function of a $SrRuO_3$ thin films coated with one unit cell of $SrTiO_3$ and $BaTiO_3$.

Capping layer	$\Phi_{\mathrm{WF}}^{\mathrm{Het}}$ (eV)	$\Phi_{\mathrm{WF}}^{\mathrm{Pt}}$ (eV)	Error margin (meV)
$BaTiO_3$	4.27 to 3.73	5.93	±40
$SrTiO_3$	4.07 to 3.87	5.97	±100

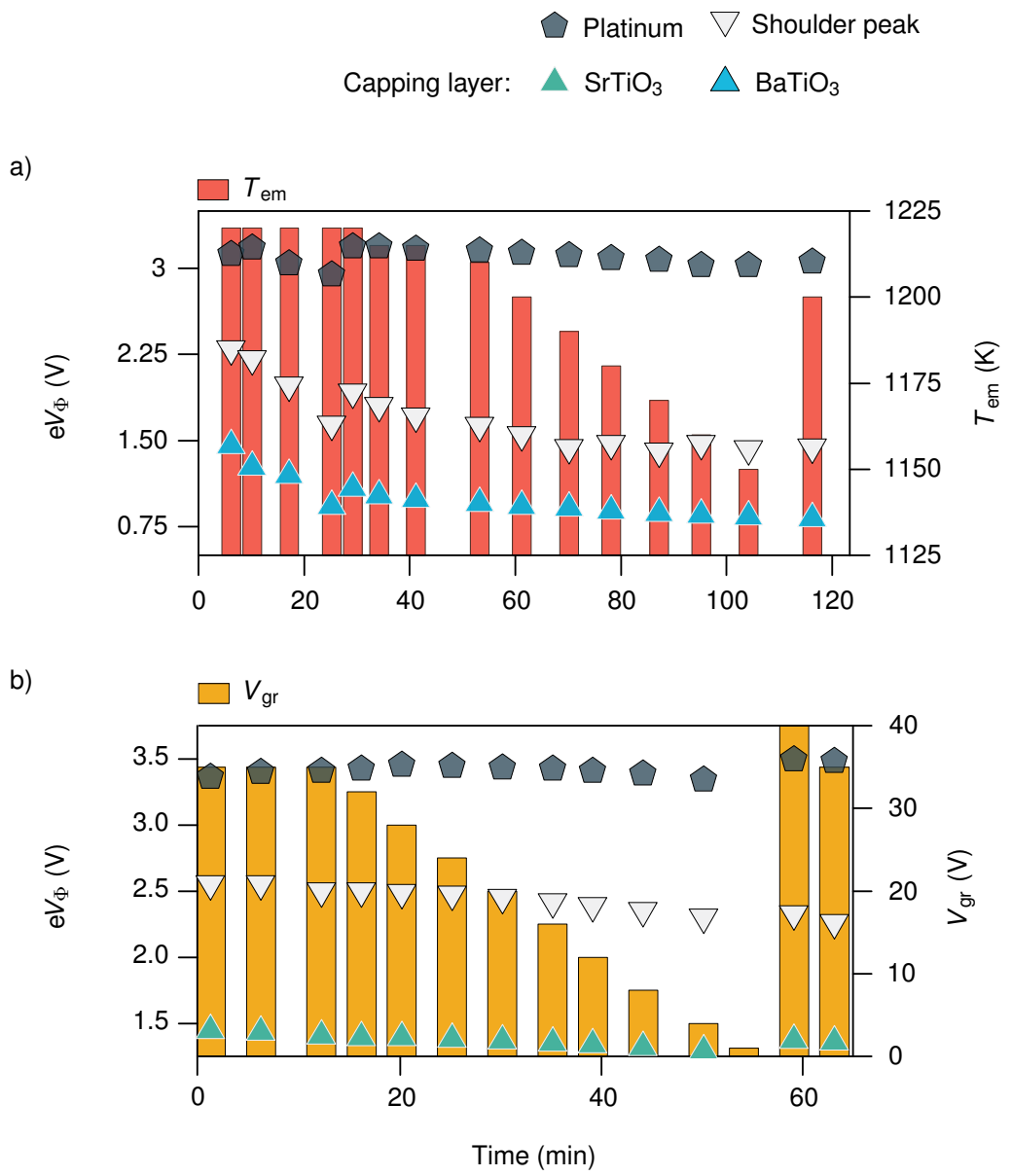

Figure 4.14: Band-alignment voltages of the reference platinum stripe, shoulder peak, and the heterostructure obtained from several measurement curves. Panel a) shows the result for a $BaTiO_3$ capping layer on a $SrRuO_3$ thin film at different temperatures and $V_{gr} = 35\,V$. Panel b) shows the results for a $SrTiO_3$ capping layer on a $SrRuO_3$ thin film at different grid voltages and $T_{em} = 1220\,K$. In panel a) the sharp drop of the eV_Φ values at $\approx$23 min is due to height adjustments of the collector that alter the eV_Φ values.

4.4.2 Results II: $LaAlO_3$ and $BaZrO_3$ monolayers

Example $I(V)$ curves of $SrRuO_3$ thin films coated with a monolayer of $LaAlO_3$ and $BaZrO_3$ are shown in Fig. 4.15. The $\mathrm{d}I_{\mathrm{cl}} / \mathrm{d}V_{\mathrm{cl}}$ curves of these heterostructures show only the occurrence of two band-alignments. No additional feature such as a shoulder-peak is observed in these experiments. This is surprising as the lattice mismatch of this capping layers with the $SrRuO_3$ thin film is much larger that the previously investigated monolayers (see table 4.4).

Similar to all previously investigated TMO thin films, the band-alignment voltages corresponding to the reference platinum stripe and these heterostructures are found to vary with time and temperature. Figure 4.16 and 4.17 show this variation for the $LaAlO_3$ and the $BaZrO_3$ capping layers on a $SrRuO_3$ thin film, respectively. However, for these two heterostructures the eV_Φ value corresponding to the reference platinum stripe (eV_Φ^{Pt}) increases drastically over time and with temperature. The reason for this increase is not understood, but the large lattice mismatch of these capping layers might have an effect on this behavior. Interestingly, it was found that by repeating the measurements on the same samples after several days and keeping them in UHV conditions, the variation of the eV_Φ^{Pt} follows a similar trend.

Figure 4.16 shows the eV_Φ values obtained for a $SrRuO_3$ thin film coated with a $LaAlO_3$ monolayer for two separate measurement series. These two measurement sets were obtained by repeating the measurement on the sample with a cooling period of several days in between. In the first set, the band-alignment voltage difference between the reference platinum stripe and the heterostructure ($eV_{\Delta\Phi}^{\mathrm{Pt–LAO\ Het}}$) increases over time and with temperature. However, the rise of eV_Φ^{Pt} is found to be larger than the reduction of $eV_\Phi^{\mathrm{LAO\ Het}}$. After a period of about 125 min and at $T_{\mathrm{em}} = 1150\,\mathrm{K}$ the eV_Φ values dropped suddenly and consequently the height of the collector had to be readjusted. So far, the reason for this sudden change in the eV_Φ values is not understood. By repeating the measurements eV_Φ^{Pt} and $eV_\Phi^{\mathrm{LAO\ Het}}$ follow a similar trend and their difference increases. Below we will determine the work function of this

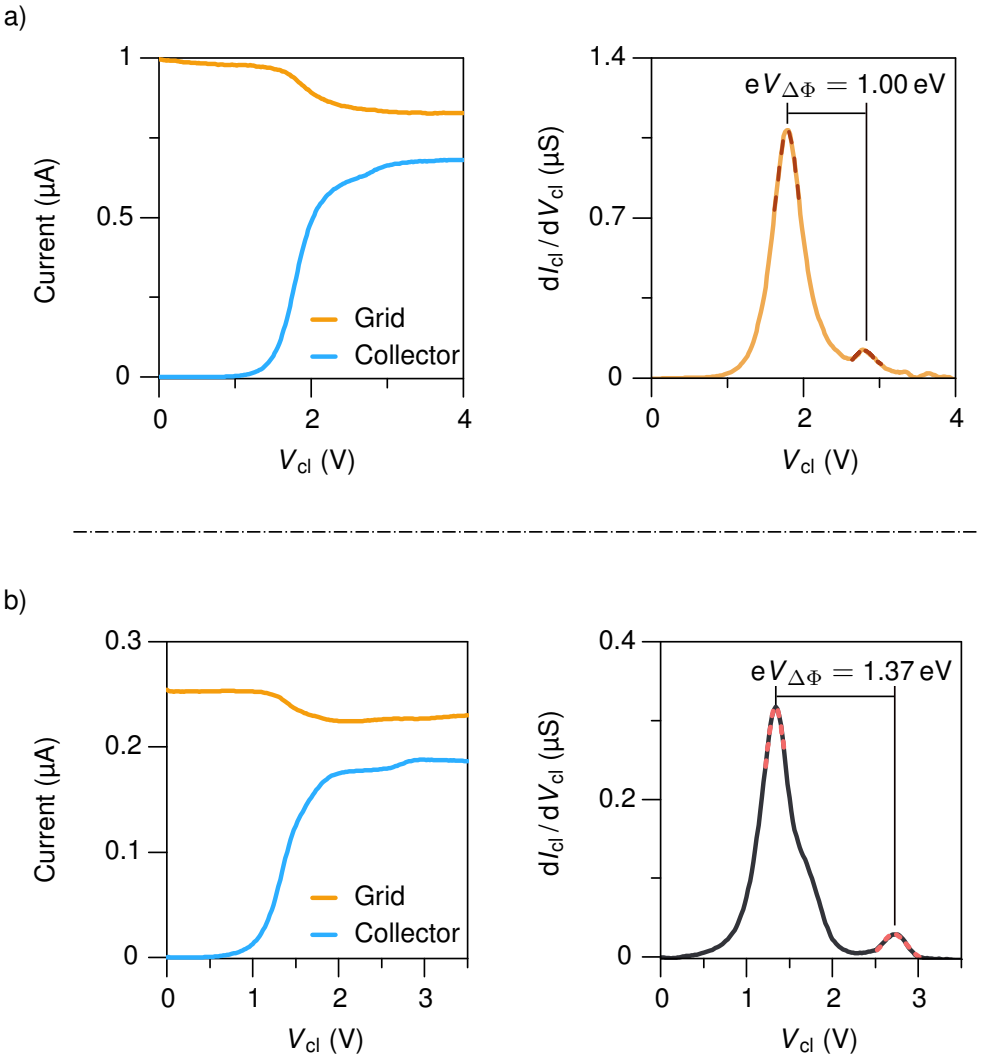

Figure 4.15: Example $I(V)$ curves of a) 1 uc thick $LaAlO_3$ coated $SrRuO_3$ thin film at $T_{em} = 1180\,K$, and b) 1 uc thick $BaZrO_3$ coated $SrRuO_3$ thin film at $T_{em} = 1140\,K$. Their dI_{cl}/dV_{cl} curves on the right show no indication of a shoulder peak. Both measurements are performed with $V_{gr} = 35\,V$.

heterostructure in the first measurement series after the height adjustment and consider a constant work function for the reference platinum stripe in all measurements.

Within the first set of the measurement and after the height adjustment, $eV_{\Delta\Phi}^{\text{Pt–LAO Het}}$ was found to increase from an initial value of 0.98 eV to 1.11 eV. The effective work function of the emitter ($\phi_{\text{em}}^{\text{eff}}$) is evaluated by the Richardson method and found to be $\phi_{\text{em}} = 3.25 \pm 0.03$ eV in this experiment. From this $\phi_{\text{em}}^{\text{eff}}$ and the eV_{Φ}^{Pt} at 2.79 ± 0.02 eV after the height adjustment (see Fig. 4.16a), $\Phi_{\text{WF}}^{\text{Pt}}$ results in 6.04 ± 0.05 eV. Consequently, the work function of this heterostructure ranges from $\Phi_{\text{WF}}^{\text{LAO Het}} = (5.06 \pm 0.05)$ eV to (4.93 ± 0.05) eV. If we further consider the same $\Phi_{\text{WF}}^{\text{Pt}}$ for the measurements before the height adjustment and all $eV_{\Delta\Phi}^{\text{Pt–LAO Het}}$ values that range from 0.81 eV to 1.11 eV, the $\Phi_{\text{WF}}^{\text{LAO Het}} = (5.23 \pm 0.05)$ eV to (4.93 ± 0.05) eV. Nevertheless, before the height adjustments the band-alignment voltages of the reference platinum stripe result in $\Phi_{\text{WF}}^{\text{Pt}} > 6.7$ eV that is very unlikely.

The results of the $BaZrO_3$ capping layer show a similar behavior to the $LaAlO_3$ capping layer, as illustrated in Fig. 4.17. The eV_{Φ}^{Pt} increases over time and temperature, and stabilizes after cooling. The band-alignment voltage for this capping layer significantly reduces however, after heating the emitter to $T_{\text{em}} = 1220$ K. By repeating the measurements on the same sample after keeping it in UHV conditions for several days, eV_{Φ}^{Pt} increases and stabilizes shortly and $eV_{\Phi}^{\text{BZO Het}}$ immediately reduces by a similar amount compared to its first measurement set (see Fig. 4.17b). Hence, the work function reduction of this heterostructure is also found to be reproducible, similar to the sample with a $LaAlO_3$ coating layer. Below, the work function of the $BaZrO_3$ capping layer is determined for both measurement sets.

In the first measurement set of the $BaZrO_3$ capping layer, eV_{Φ}^{Pt} varies from 2.46 eV to 3.11 eV and stabilizes afterwards at 2.85 ± 0.02 eV by cooling the emitter (see Fig. 4.17a). The band-alignment voltage of the heterostructure ($eV_{\Phi}^{\text{BZO Het}}$) varies in these measurements from 1.36 eV to 1.07 eV with time and temperature. Thus, the $eV_{\Delta\Phi}^{\text{Pt–BZO Het}}$ ranges from 0.81 eV to 1.77 eV during the entire measurement period. The effective work function of the emitter is determined by the Richardson method during the temperature rise

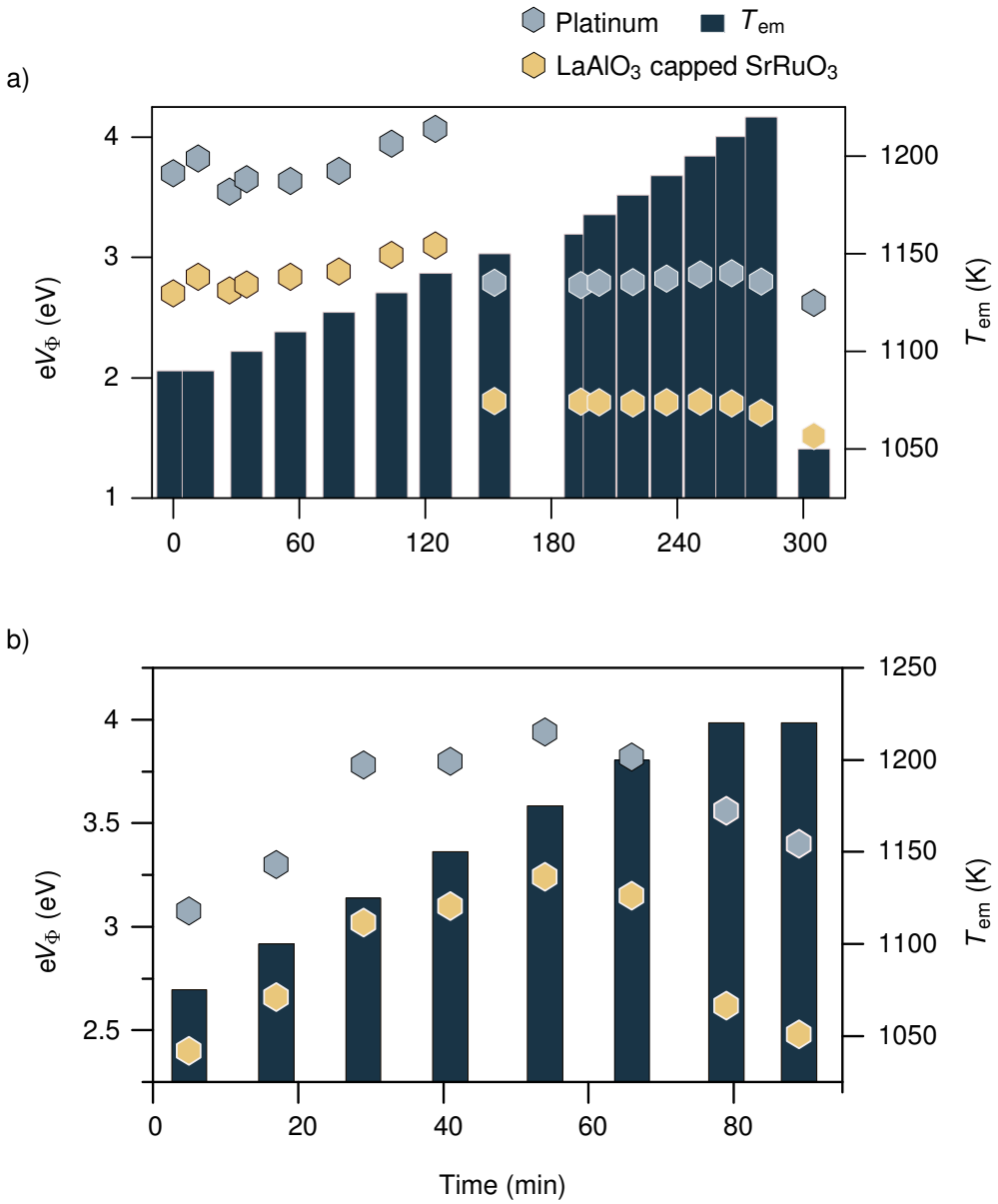

Figure 4.16: Band-alignment voltages (eV_Φ) corresponding to the reference platinum stripe and 1 uc $LaAlO_3$ capping layer on a $SrRuO_3$ thin film extracted from several measurements at different temperatures. Panel a) shows the *in-situ* results directly after the sample transport to the measurement system. The sharp drop of the eV_Φ values at ≈150 min is due to height adjustments that alters the effective work function of the emitter. Panel b) shows the results by repeating the experiments on the same sample after several days and keeping it in UHV condition. All measurement are conducted with $V_{gr} = 35$ V.

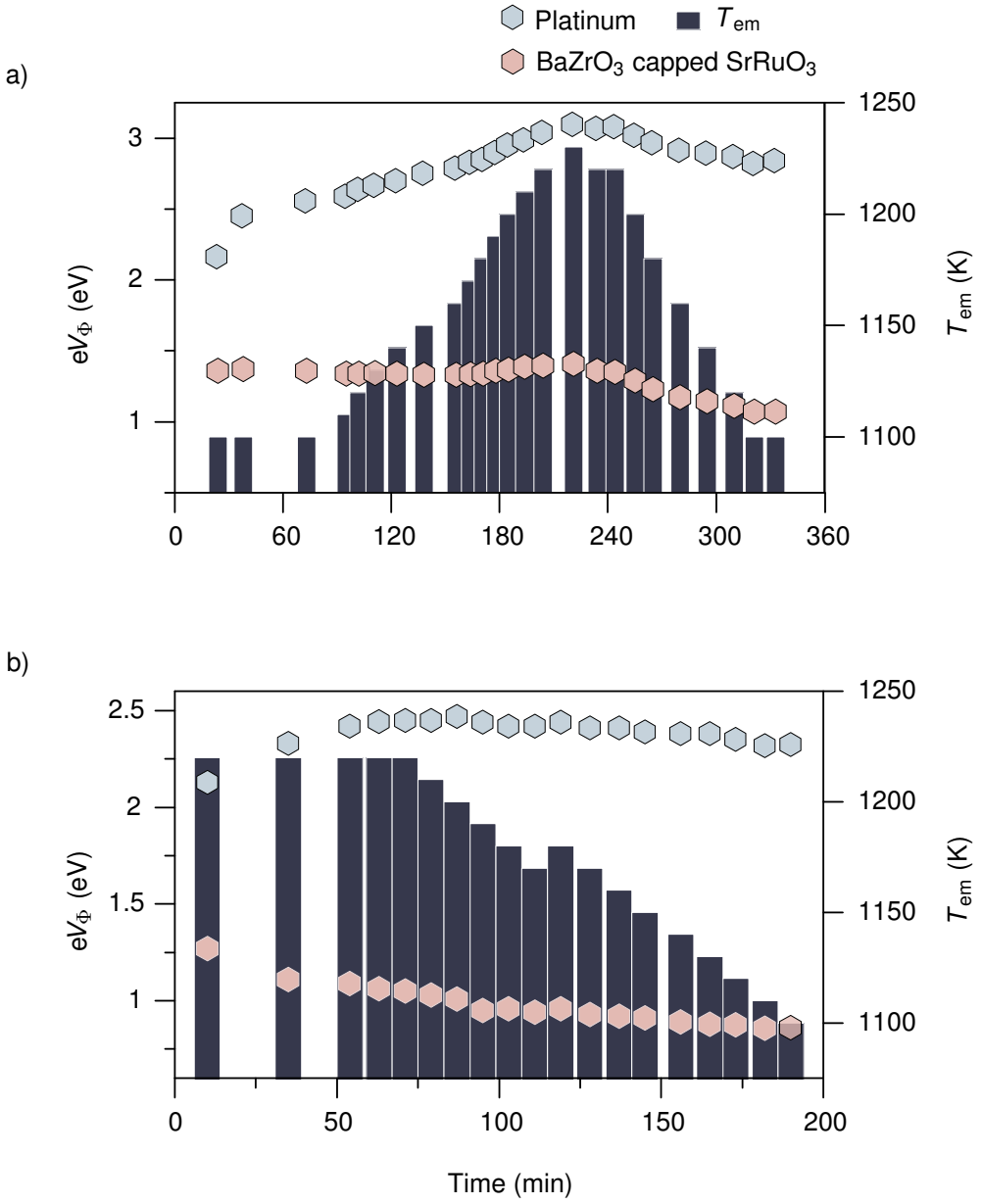

Figure 4.17: Summary of the band-alignment voltage change during the measurements of a $SrRuO_3$ thin film capped with 1 uc if $BaZrO_3$, in two sequential measurements. Panel a) shows the obtained eV_Φ values in the first set, and panel b) by repeating the measurements of the same sample after several days (*in-situ*). In all measurements $V_{gr} = 35\,V$.

to be $3.00 \pm 0.02\,\mathrm{eV}$, and in the temperature drop to be $2.89 \pm 0.02\,\mathrm{eV}$ in this set. Considering these values and the eV_{Φ}^{Pt} from the last measurements ($2.84 \pm 0.01\,\mathrm{eV}$, see Fig. 4.17a), $\Phi_{\mathrm{WF}}^{\mathrm{Pt}}$ is found to be $5.79 \pm 0.06\,\mathrm{eV}$ for this sample. Here, we have considered $\phi_{\mathrm{em}}^{\mathrm{eff}}$ to be $2.95 \pm 0.06\,\mathrm{eV}$ for the entire measurement period. Hence, the work function of this heterostructure ($\Phi_{\mathrm{WF}}^{\mathrm{BZO\ Het}}$) is found to vary from $(4.98 \pm 0.06)\,\mathrm{eV}$ to $(4.02 \pm 0.06)\,\mathrm{eV}$ over time and with temperature.

In the second measurement set, the $eV_{\Delta\Phi}^{\mathrm{Pt\text{–}BZO\ Het}}$ varies from $0.86\,\mathrm{eV}$ to $1.46\,\mathrm{eV}$ and eV_{Φ}^{Pt} stabilized after $T_{\mathrm{em}} = 1175\,\mathrm{K}$ at $2.39 \pm 0.01\,\mathrm{eV}$. The effective work function of the emitter is found to be $3.00 \pm 0.03\,\mathrm{eV}$, similar to the first measurement set. Hence, $\Phi_{\mathrm{WF}}^{\mathrm{Pt}} = 5.39 \pm 0.04\,\mathrm{eV}$ and $\Phi_{\mathrm{WF}}^{\mathrm{BZO\ Het}}$ varies from $4.53 \pm 0.04\,\mathrm{eV}$ to $3.93 \pm 0.04\,\mathrm{eV}$.

The results of the $LaAlO_3$ and $BaZrO_3$ capping layers on SRO thin films are tabulated in table 4.6. The comparison of the work function values of the two sets of the $BaZrO_3$ capping layer show a decrease of $\sim$0.45 eV for all work function values. The reproducibility of $\phi_{\mathrm{em}}^{\mathrm{eff}}$ in these sequential experiments suggests that this change is due to the collector material and not from the experimental alignment. Considering our experimental conditions and the extensive measurement time, such an drop can be caused by various effects, *e.g.*, loss of oxygen or distortion of the heterostructure. The drop of $eV_{\Delta\Phi}^{\mathrm{Pt\text{–}BZO\ Het}}$ at $\approx$197 min could result from such effects that was not observed in the second measurement set (see Fig 4.17). Similar observations are reported for the barrier height at the interface of $SrTiO_3$ and $BaTiO_3$ with platinum upon annealing in vacuum [92]. However, more investigations are required for a conclusive statement.

Table 4.6: Work function values obtained for $SrRuO_3$ thin films coated with a one-unit-cell thick layer of $LaAlO_3$ or $BaZrO_3$. The values in parentheses have been obtained from the second set of the $BaZrO_3$ measurements.

Capping layer	$\Phi_{\mathrm{WF}}^{\mathrm{Het}}$ (eV)	$\Phi_{\mathrm{WF}}^{\mathrm{Pt}}$ (eV)	Error margin (eV)
$LaAlO_3$	5.21 eV to 4.93 eV	6.04 eV	±0.05
$BaZrO_3$	4.98 eV to 4.02 eV	5.79	±0.06
	(4.53 eV to 3.93 eV)	(5.39)	(±0.04)

4.5 Summary

The results of the LaB_6 thin film and Nb:$SrTiO_3$ (0.1 wt. %) at the beginning of this chapter demonstrate the high accuracy of the experimental set-up and measurement concept established in this work. These results are in good agreement with both the experimental values and model calculations found in the literature. Thus, work function measurements by thermoelectronic converters are accurate and can in-addition provide information about the material properties at elevated temperatures.

The work function measurements of the investigated TMOs, *i.e.*, $SrRuO_3$ thin films and the fabricated heterostructures exhibit a unique characteristic. The results in this chapter illustrate that the work function of these thin films reduces by increasing temperature. This behavior is surprising as the work function of transition metals, *e.g.*, Mo and Ni [93] or pure silicon [94] is reported to increase with temperature. The results of the measurements suggest that surface relaxation mechanisms cause this reduction. This understanding is in agreement with the model calculation of Zhong *et al.* [37]. Moreover, the final work function of ≈4 eV obtained for the bare $SrRuO_3$ thin films suggests that this material is a good candidate for cathode technology that could also operate in poor vacuum conditions with an oxygen background pressure. For instance, cathodes made of $SrRuO_3$ could replace tungsten cathodes in RHEED devices.

The key investigation of this thesis is the tailoring of TMO work functions by epitaxial capping layers with a thickness of one-unit-cell. The results in this chapter demonstrated that the work function of TMOs is tunable, *i.e.*, it can be reduced or increased by an appropriate capping layer. This investigation was explored using $SrRuO_3$ thin films as a model material with several capping layers for tuning its work function. These results are summarized in table 4.7. For instance, the work function of $SrRuO_3$ (4.8 eV) can be tuned in a controlled manner to decrease to 4.3 eV or increase to 5 eV by the deposition of a single unit cell of $BaTiO_3$ and $BaZrO_3$, respectively. Such control of this essential material property enables the design of optimized materials and devices, *e.g.*, for the interfaces in oxide electrons or catalytic

Table 4.7: Modified work function values of $SrRuO_3$ thin films by depositing monolayer of a perovskite on their surfaces. The values in the parenthesis correspond to the lowest measured work function (unrelaxed).

Monolayer	$\Phi_{WF}^{Heterostructure}$ (eV)	$\Phi_{WF}^{Platinum}$ (eV)	Error (eV)	Φ_{WF} change
	4.85 (4.01)	5.63	±0.03	
$BaTiO_3$	4.27 (3.73)	5.93	±0.04	−12 (−7)%
$SrTiO_3$	4.07 (3.87)	5.97	±0.1	−16 (−3.5)%
$LaAlO_3$	5.21 (4.93)	6.04	±0.05	+7.4 (+23)%
$BaZrO_3$	4.98 (4.02)	5.79	±0.06	+2.7 (+0.2)%

processes at surfaces. Moreover, these selected monolayers provide insight into the electronic structure at the interface of TMO heterostructures and their surface dipoles.

The deposition of the $BaTiO_3$ and the $SrTiO_3$ monolayers both reduce the work function of $SrRuO_3$ similarly, while the $BaZrO_3$ increases it. Because $BaTiO_3$ and $SrTiO_3$ share the same transition metal on their B-site, and the $BaTiO_3$ and $BaZrO_3$ the same A-ion (see Fig. 4.9), the results suggest a BO_2 termination for these heterostructures. This observation is in agreement with the results of bare $SrRuO_3$ thin films that suggest a BO_2 termination for this thin film. Furthermore, the model calculations of Zhong *et al.* predict that the work function of $SrRuO_3$ will increase by deposition of a $LaAlO_3$ capping layer only for RuO_2 termination. Hence, the work function of BO_2 terminated perovskites is determined by the final atomic layer, *i.e.*, the TiO_2, RuO_2, or ZrO_2 layer. Up to now, the EELS and EDX analyses of the STEM images are pending to confirm this termination of these heterostructures.

The substitution of Ba with Sr at the interface only changes the work function by ≈200 meV. This difference may result from a variation of charge transfer at the interfaces, variation of the interface distance, or strain of the capping layer. These results provide unique information about the interface of TMO-heterostructures that in combination with model calculations can

provide a detailed description of these complex interfaces.

The change of the band-alignment voltage of the reference platinum stripe during the measurements is not understood. Schafraneck *et al.* [92] have investigated the interface between $SrTiO_3$ and $BaTiO_3$ with Pt and report on a change of the barrier height upon annealing in a controlled atmosphere. The effect of Schottky barriers on the work function measurements presented in this work is unlikely, due to the small currents used in these experiments and the relatively high voltages required for the band-alignment voltages [84]. More investigations are needed, however, to understand this behavior.

The work function of the evaporated reference platinum stripe is found to be larger on the heterostructures than on the bare $SrRuO_3$ thin film. This difference suggests that the 1 uc capping layer alters the growth dynamics of Pt and results in a crystal orientation that has work function >400 meV. This observation was confirmed by the X-ray analyses that indicate a different orientation for evaporated Pt on these heterostructures compared to the bare $SrRuO_3$ thin film. These results demonstrate the sensitivity of this material property for device fabrication processes, and once again illustrate the accuracy of the measurement system and concept developed in this work.

Another important aspect of this work is to explore the thermal stability of TMOs at elevated temperatures and in the operating conditions of a thermoelectronic converter. Figure 4.18 compares the surface morphology of two $SrRuO_3$ thin film samples after a relatively long measurement period at $T_{em} > 1475\,K$, and $T_{em} \leq 1250\,K$ under UHV conditions. The AFM image of the sample exposed to high temperatures shows deformations and damages on the surface. In this image no evidence of steps-and-terraces from the Nb:$SrTiO_3$ substrate is observed, and the surface indicates a unique grain formation (see Fig. 4.18a). Further investigations revealed that this change is mainly due to thermal radiations of the filament escaping through the BN spacers, rather than the radiation from the emitter's surface. To overcome this, major upgrades were performed on the measurement system to improve the thermal-radiation shielding of the filament. Furthermore, a low work function emitter was installed to reduce the operating temperature of the system. These upgrades improved the stability of the $SrRuO_3$ thin films and

consequently their surface morphology exhibited the typical structure of a $SrRuO_3$ thin film [87] after the measurements, as shown Fig. 4.18b. Indeed, all measurements of the bare $SrRuO_3$ thin films and the thin films coated with a monolayer presented in this chapter were performed after these upgrades. Figure 4.19 shows the AFM images of the monolayer heterostructures after their work function measurements.

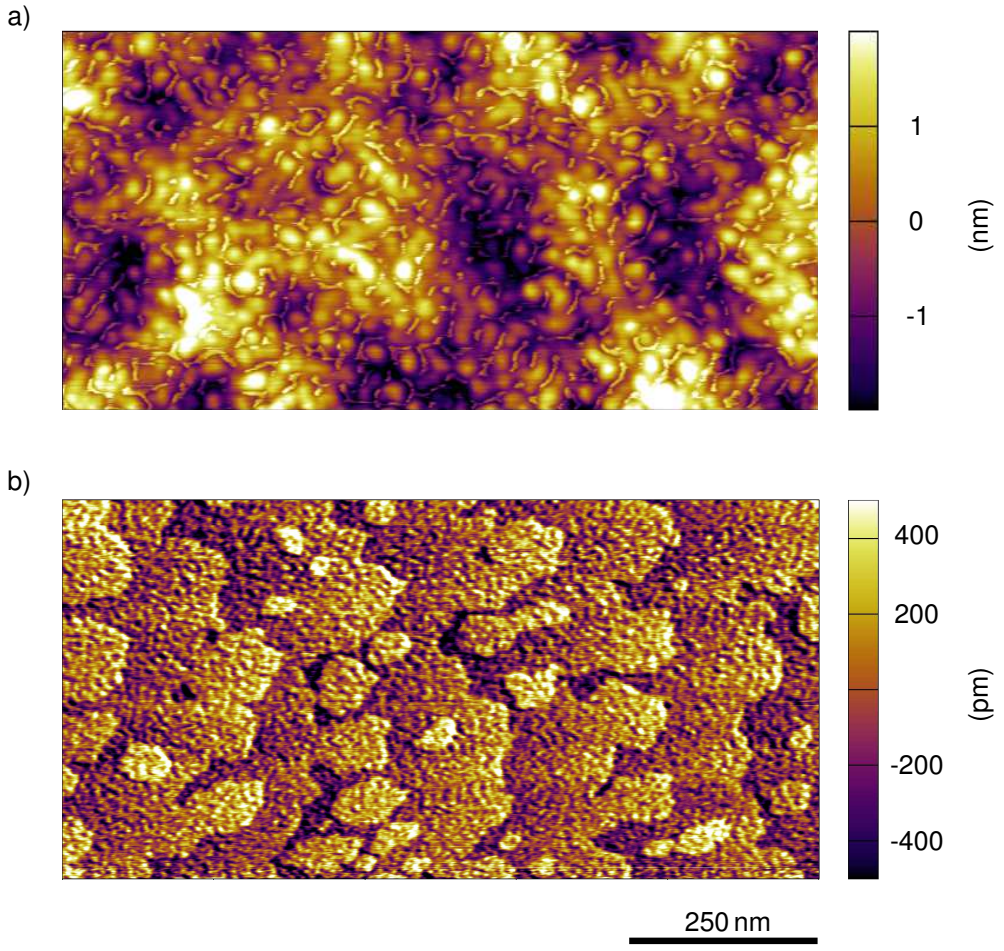

Figure 4.18: AFM images of $SrRuO_3$ thin films after work function measurements. Panel a) shows severe change of the morphology due to thermal radiation of the filament ($T_{\mathrm{em}}^{\mathrm{max}} = 1550\,\mathrm{K}$). Panel b) shows the preserved epitaxial structure of the sample after reducing the thermal radiations of the filament ($T_{\mathrm{em}}^{\mathrm{max}} = 1250\,\mathrm{K}$). The thickness of these films are $\sim$30 uc and $\sim$24 uc in panel a) and b), respectively.

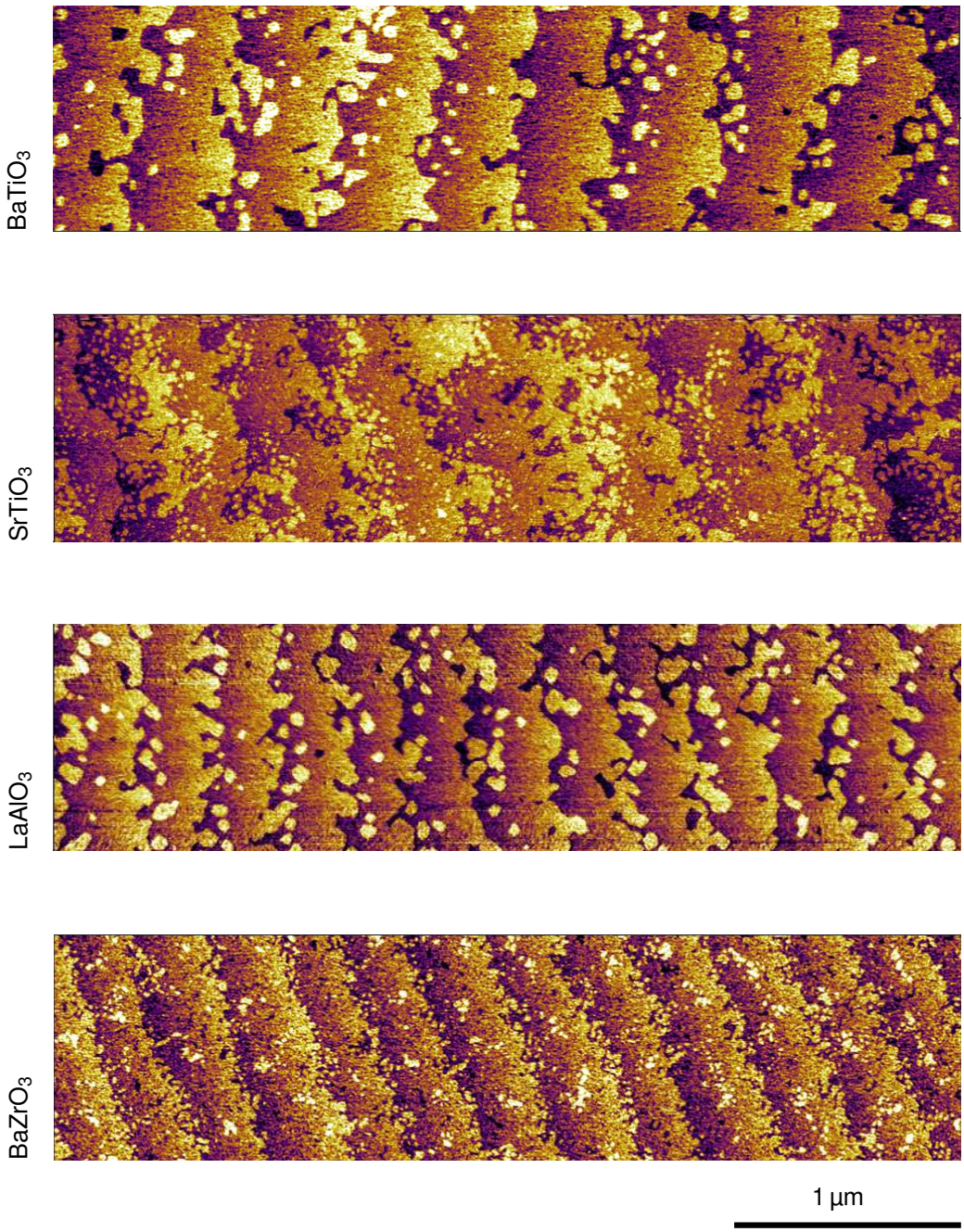

Figure 4.19: AFM images of $SrRuO_3$ thin films capped with 1 uc of a perovskite after their work function measurements. All investigated heterostructures well endured the temperatures used during the experiment ($T_{\mathrm{em}}^{\mathrm{max}} = 1250\,\mathrm{K}$).

The appearance of a shoulder peak in the measurements of the $BaTiO_3$ and $SrTiO_3$ capping layers suggest an incomplete surface coverage in these heterostructures. This result is surprising considering the small lattice mismatch of these capping layers with $SrRuO_3$, when compared to the $LaAlO_3$ and $BaZrO_3$ capping layers (see table 4.4). Besides, the STEM images show sharp interfaces in these heterostructures (see Fig. 4.10). Figure 4.20 shows an STEM image of several unit cells of $BaTiO_3$ deposited on a $SrRuO_3$ thin film. It appears that the growth of $BaTiO_3$ on $SrRuO_3$ follows an island growth mode, such as Stranski-Krastanov, that is in agreement with our results for a monolayer. This agreement between the work-function results and the STEM images illustrate that work function measurements can provide qualitative and detailed information about the surface structure that might be hardly achieved by other characterization methods such as RHEED.

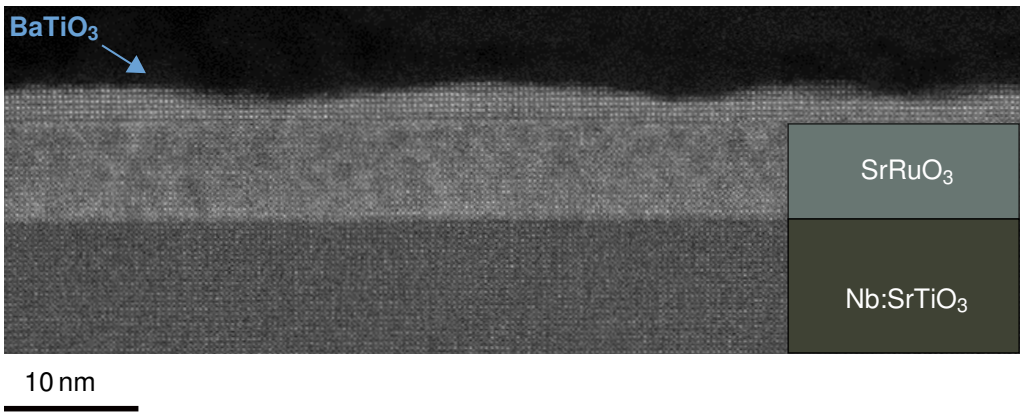

Figure 4.20: Zoomed-out HAADF-STEM image of a $BaTiO_3$-$SrRuO_3$ Nb:$SrTiO_3$ heterostucture. The surface morphology suggests an island growth mode for the $BaTiO_3$ capping layer on $SrRuO_3$ thin films (Stranski-Krastanov). Imaging performed by V. Srot form *Stuttgart Center for Electron Microscopy (StEM)*.

Chapter 5

Photon Induced Thermionic Emission of Carbon Nanotubes in a Thermoelectronic Setup

The measurement system described in chapter 3.2 is designed to be compatible with the latest developments, and state-of-the-art methods for thermionic emission. These include "*Photon Enhanced Thermionic Emission*" (PETE) [95], and "*Photon Induced Thermionic Emission*" (PITE) [96]. This chapter reports on Furthermore, it demonstrates the compatibility of PITE with the concept of thermoelectronic conversion for space-charge suppression. These investigations are essential for realizing solar energy converters based on PITE.

The work presented here is done in collaboration with the research group of Prof. A. Nojeh from the University of British Columbia (UBC) [97], who provided the samples and the optical components. The experiments were carried out along with one of their Ph.D. students at the time, Kevin Voon.

5.1 Introduction

Carbon-nanotube (CNT) forests demonstrate new opportunities for energy conversion by thermionic emission [98]. These highly dense packed and vertically aligned CNTs have unique electrical [99] and thermal properties [100, 101]. Additionally, these quantum materials demonstrate a "near perfect" absorption of light [102] that results in electron emission upon light irradiation [96]. Figure 5.1 shows an SEM image of a CNT-forest sample.

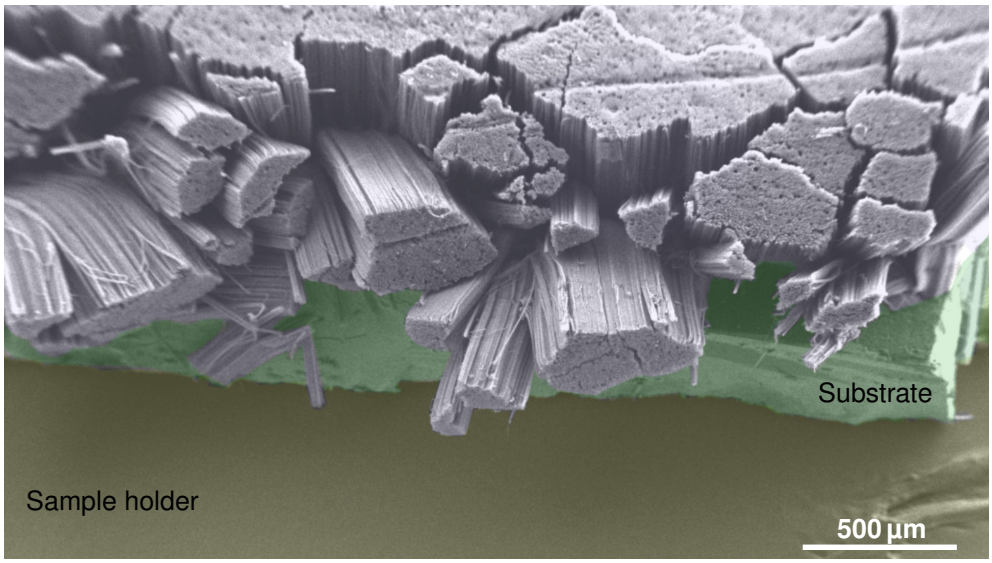

Figure 5.1: False colored SEM image of a CNT-forest sample. All samples are grown by chemical vapor deposition on doped silicon substrates and are nominally identical. The sample fabrication procedure is described in Ref. [103].

The radiation of focused light on these perfect absorbers results in the local heating of the CNTs that causes incandescence. The temperature of these so-called "Heat traps" [96] is so high that electron emission through thermionic emission occurs. Hence, this process is referred to as photon-induced thermionic emission. This effect is observed on the side-walls as well as on the surface of these materials. Figure 5.2 shows an incandescence spot on the surface of a CNT-forest sample.

This direct conversion of light into electric current is promising for energy conversion applications. Based on our observations, remarkably low light-

intensities are required for inducing incandescence spots. For instance, we have observed emission currents using a laser with a wavelength of 532 nm at intensities as low as 60 mW. However, to realize such devices, two critical issues need to be examined. These are the observed emission-current decay in these devices [104, 105], and the space-charge problem that is inherited from the thermionic process.

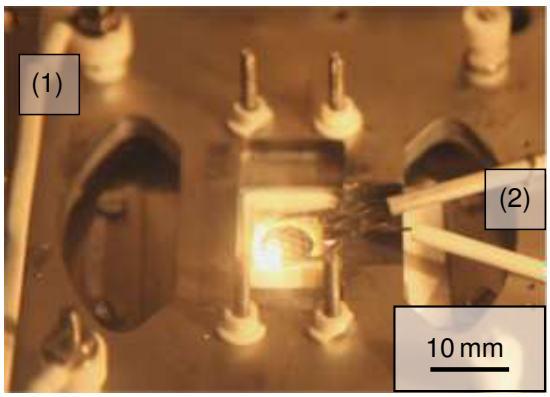

Figure 5.2: Photograph of an incandescence spot on a CNT-forest sample generated by a focused light source ($\lambda = 1064$ nm). The laser beam irradiates the surfaces after passing through a transparent conductive collector and the grid meshes. The electrical contacts for the grid and collector are labeled (1) and (2), respectively.

The results in this chapter are presented in two separate sections to address the problems mentioned above. First, the current decay of these devices is investigated in a standard vacuum tube configuration. For this, their PITE characteristics are studied by a positively charged grid and collector. Second, we will apply a magnetic field and moderate grid voltages to suppress the space-charge, similar to a thermoelectronic converter.

In the following measurements, all incandescence spots are induced on the surface of the CNT-forests. Such a configuration is essential for practical applications. For this purpose, the measurement system described in Sec. 3.2 is upgraded to be compatible with such measurements. These technical descriptions are discussed in the section below.

5.2 Experimental setup

A central part of the experiments is the magnetic yoke. This component is designed with holes, with a diameter of 7 mm at the center. By using commercially available NdFeB ring magnets [65] on one side, the laser could be aimed through their center to reach the surface of the CNTs. The magnetic field simulations in Fig. 5.3a show that the combination of ring magnets together with block magnets facing each other on opposite sides results in a homogeneous field. The strength of the field was measured using a Hall sensor to be ≈250 mT at the center of the grid, in good agreement with the simulation results.

As mentioned earlier, the experiments are designed such that light is perpendicular to the surface of the CNTs. For this, a tungsten grid with a mesh size larger than 1 mm (see Fig. 3.7c) is used as well as an indium-thin-oxide (ITO) coated quartz substrates which served as collector. This transparent and conductive coating [106] allows light to pass through and electrical measurements to be performed. A sketch of the experiments is shown in Fig. 5.3b.

The electrical contact to the ITO is established mechanically by pressing it

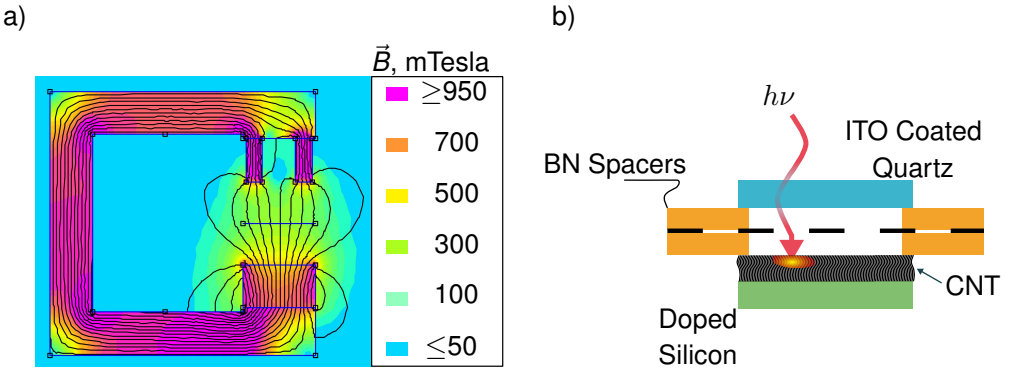

Figure 5.3: Panel a) shows the magnetic field simulations done by Femm [66]. The magnetic field at the center is fairly homogeneous. Panel b) shows a sketch of the designed experiments. Indium-tin-oxide coated quartz substrates are used as collectors due to their optical (transparent) and electrical (conductive) properties. In the sketch, the grid is represented by the dashed black line.

onto a tantalum foil with a nominal thickness of 5 µm. The CNT samples are loaded on the collector stage (see Fig. 3.5) and the sample holder establishes the electrical contact.

The optical setup is shown in Fig. 5.4. The heat traps are caused using two laser modules from *Laserglow* [107] with nominal wavelengths of 532 nm and 1064 nm. The maximum output power of the lasers is ≈150 mW and ≈600 mW, respectively. It was found that their output power depends highly on their battery level. Thus, the output power was measured before every measurement using a bolometer from Thorlabs [108]. A variable ND filter is positioned in front of the light source that adjusts the laser intensity (see Fig. 5.4). Afterwards, a lens with focal length of 30 cm and an optical stage is used to focus and to align the laser beam.

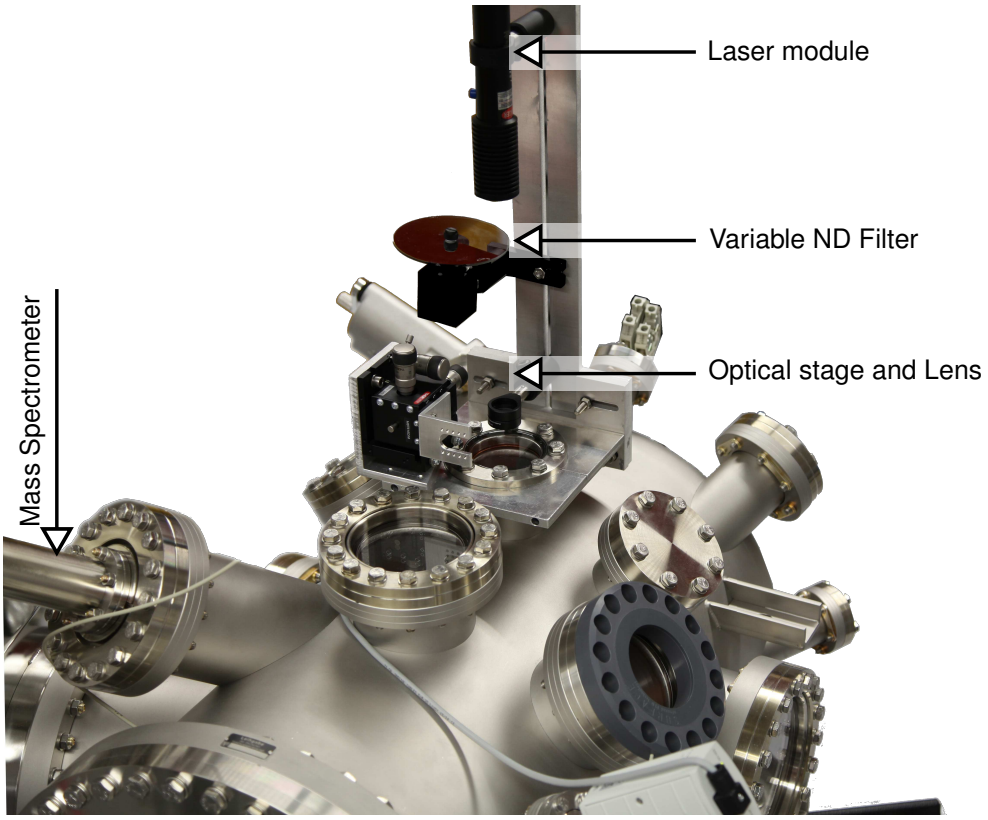

Figure 5.4: Photograph of the measurement system with the optical components for PITE. The components are installed on a DN63 CF flange, centered on the grid position. The measurement system is described in Sec. 3.2.

5.3 Results

5.3.1 PITE characteristics of CNT-forests

Emission behavior of incandescence spots at different laser intensities is shown in Fig. 5.5. By increasing the laser intensity the total emission current increases as a result of the higher temperatures of the heat traps. At all laser intensities, the emission current tends to decay over time to lower, but relatively more stable values. Similar behavior is reported in Ref. [96, 104, 105]. However, by increasing the laser intensity from 350 mW to 450 mW, the increase of the emission current is not as high as the rise from the previous increments of the laser intensity. Furthermore, the current decay becomes more abrupt over time.

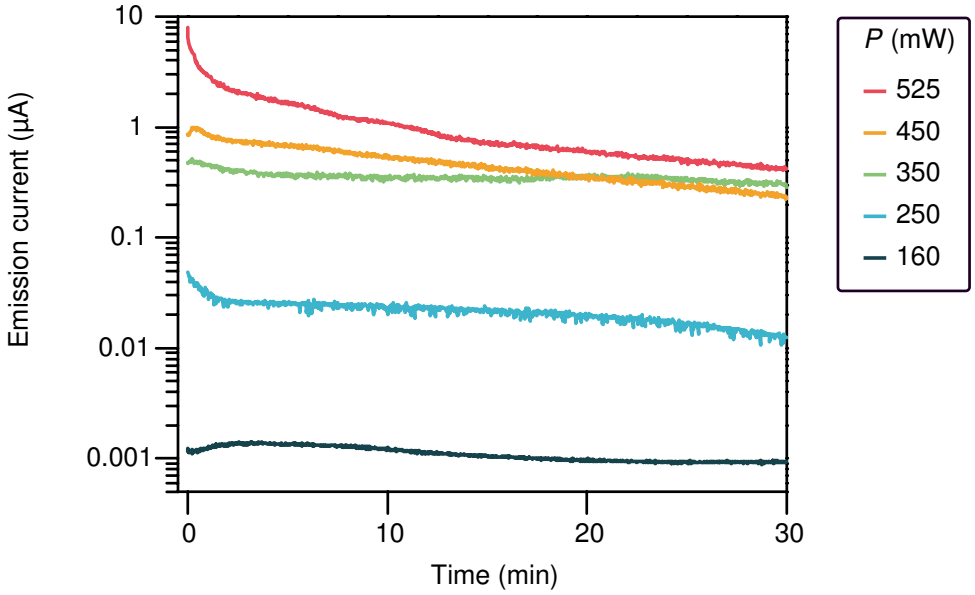

Figure 5.5: Electron emission current of CNTs induced by laser radiation of several intensities ($\lambda = 1064\,\mathrm{nm}$). For all investigated laser intensities the emission-current decays over time. A similar behavior was observed by using the second laser module ($\lambda = 532\,\mathrm{nm}$). All measurements have been conducted with $V_{\mathrm{gr}} = 40\,\mathrm{V}$ and $V_{\mathrm{cl}} = 30\,\mathrm{V}$. In each experiment, the focal point of the laser was adjusted to hit on the sample on the edges to obtain several reproducible measurements on the same sample.

A possible contributing factor to the current decay could be the evaporation and deformation of the nanotubes due to the high temperatures of the incandescence spots. At high laser intensities, currents up to 8 µA are recorded. Considering an effective heated area of 0.1 mm^2, the work function of CNTs (∼4.5 eV [109]), and the derived Richardson constant (120 $A\,K^{-2}\,cm^{-2}$), this current density corresponds to temperatures of >1900 K. Taking into account the vapor-pressure diagram of carbon [110], these elevated temperatures would cause damage to the CNTs.

The evaporation of the CNTs is observed in the residual mass spectrum (RMS) of the chamber, as shown in Fig. 5.6. The RMS shows an increase of

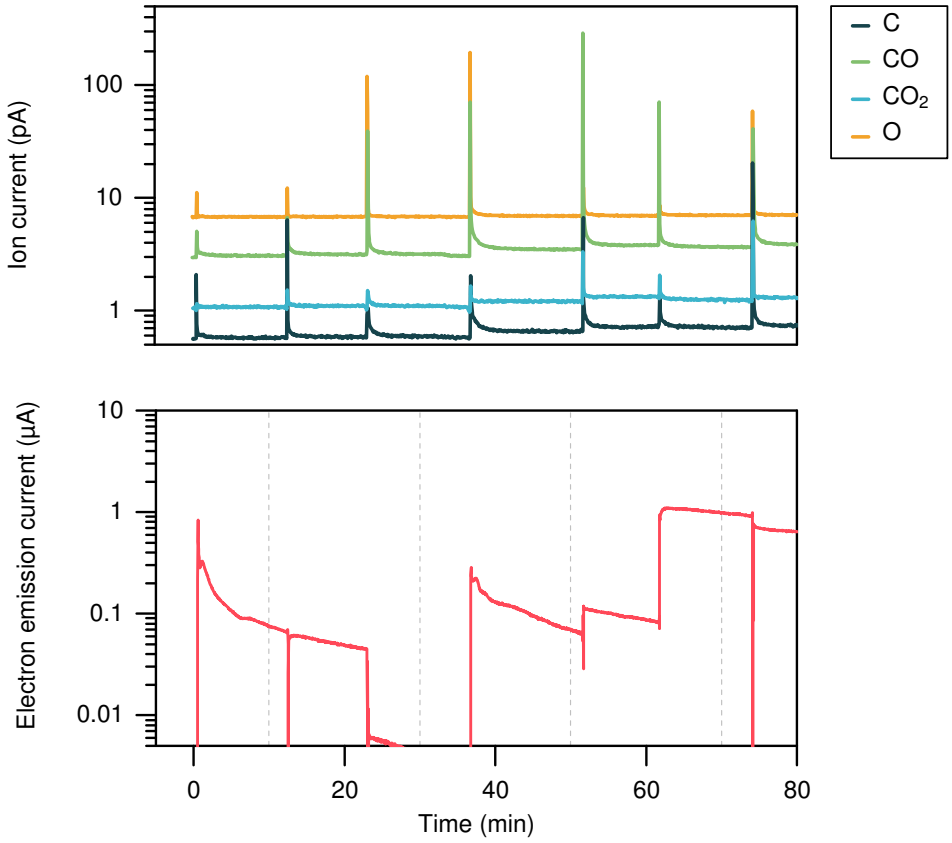

Figure 5.6: Simultaneous measurement of the decay of the emission current and the residual mass spectrum of the chamber. In the mass spectrum, ion currents from carbon and its compounds rise at the same time an incandescence spot is created. The infrared laser was operated with an output power of 500 mW.

carbon and carbon-related compounds at the same time an incandescence spot is created. During these measurements, the pressure of the chamber reached $>6 \times 10^{-8}$ mbar from an initial base pressure of $<2 \times 10^{-8}$ mbar.

Additionally, SEM images of irradiated samples show a deformation of the surface that could result from the high temperatures. This change of the surface morphology is shown in Fig. 5.7. The size of this area corresponds to the expected spot size resulting from the optical alignments and components. However, more investigations are required for a conclusive statement.

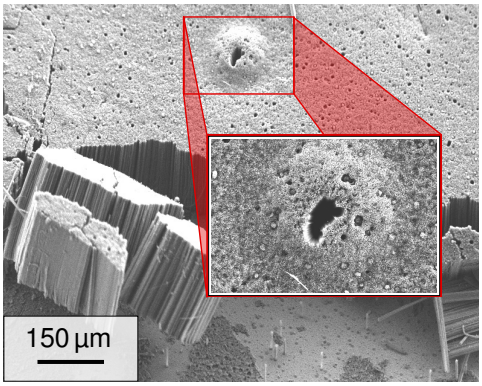

Figure 5.7: SEM image of a CNT-forest sample after laser irradiation ($\lambda = 532\,\text{nm}$ at $60\,\text{mW}$). The deformation highlighted in red may have resulted from the heat traps.

5.3.2 PITE of CNT-forests in a thermoelectronic setup

Figure 5.8 compares the emission current during collector voltage-sweeps with and without applying a magnetic field. Here, the grid voltage is kept constant at $V_{\text{gr}} = 20\,\text{V}$ for both cases. Without a magnetic field, the collector current follows *Child's Law*, demonstrating the space-charge reduction by the increase of the collector voltage. In this case, even at $V_{\text{cl}} = 40\,\text{V}$ the current is not saturated. However, after inserting the magnetic yoke, the current increases exponentially as eV_{Φ} is reached and saturates afterward. This kind of increase demonstrates the space-charge suppression to a large extent, as discussed in section 2.2.

The results shown in Fig. 5.8 demonstrate the compatibility of PITE with the concept of the thermoelectronic converter. However, the voltages required for band alignments (eV_Φ) is found to be unexpectedly large and the reason for it not understood. From the emitter side, a possible explanation might be the Schottky barrier formed between the doped silicon substrate and the nanotubes, next to the barrier between the substrate and sample holder. From the collector side, the mechanical contact to the surface of the ITO coating might be unstable, or may even have been damaged during the installation of its electrical contacts.

Moreover, the thermal radiation of the heat traps (see Fig. 5.2) could damage the ITO coating on the quartz substrate. The optical absorption coefficient of ITO is reported to be at its highest in the near infrared regime [106].

Figure 5.9 compares the emission currents during voltage-sweeps of the collector at different grid voltages. By increasing the grid voltage, the collector

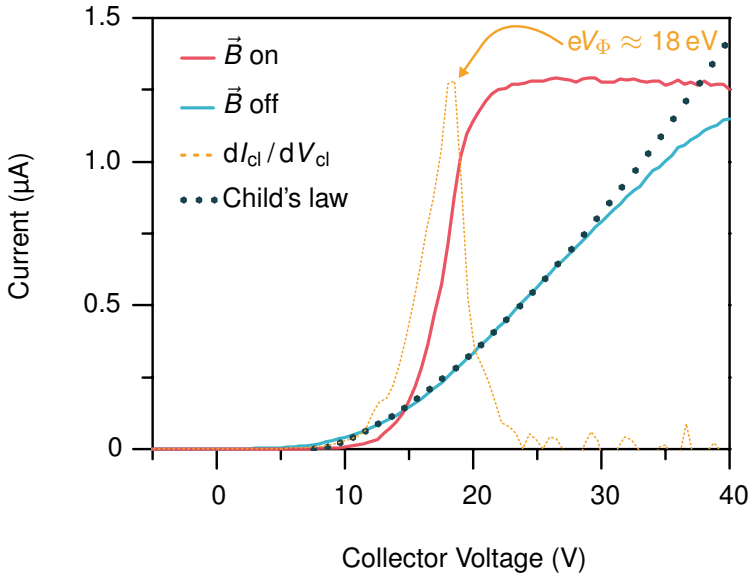

Figure 5.8: Proof of concept of the compatibility of the thermoelectronic converter with PITE. Without a magnetic field and due to the space charge, I_{cl} follows *Childs Law*. By applying the magnetic field, the current increases exponentially as the bands align (see text). The grid voltage has been set to $V_{\mathrm{gr}} = 20\,\mathrm{V}$ for both cases. The FWHM of the $\mathrm{d}I_{\mathrm{cl}}\,/\,\mathrm{d}V_{\mathrm{cl}}$ curve is $\approx$3.5 V, possibly reflecting damages of the collector and emitter.

current (I_{cl}) increases as a result of space-charge suppression. For $V_{\mathrm{gr}} \geq 27.5\,\mathrm{V}$, I_{cl} decreases because the potential of the grid is then large enough to absorb the electrons. This behavior is illustrated in Fig. 5.9b and also observed for thermoelectronic converters [23]. The shift of the band-alignment position (eV_{Φ}) in every measurement supports the previous assumption of the change or damage to the ITO coating on the collector surface. Furthermore, even at $V_{\mathrm{gr}} = 35\,\mathrm{V}$ the band-alignment voltage is not significantly altered that rules-out space-charge effects for the observed eV_{Φ} values. However, more investigations are required for a conclusive statement.

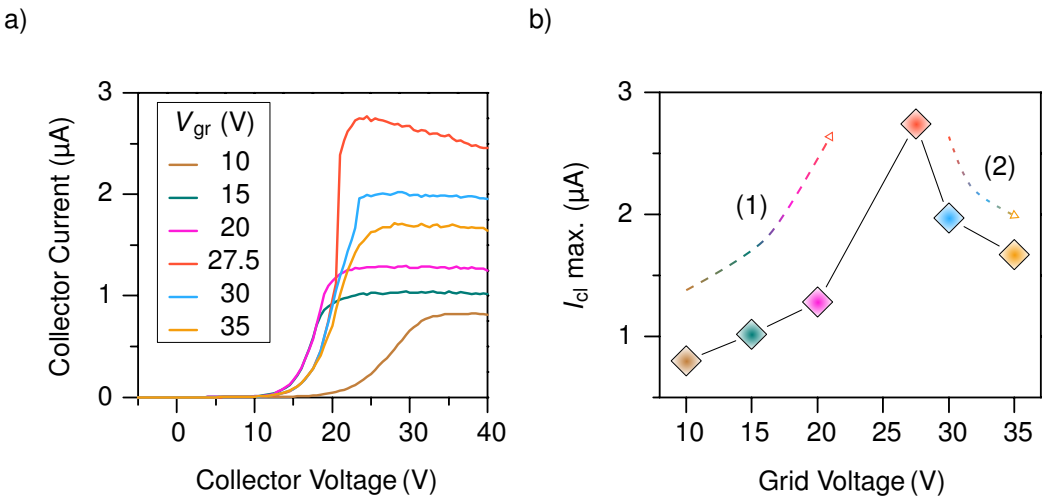

Figure 5.9: Panel a) shows the collector current as function of the collector voltage at different grid voltages in a thermoelectronic configuration ($\vec{B}$ on). Each measurement curve is obtained from a different incandescence spot on the same sample. The large value of eV_{Φ} and its shift in the different measurements is not understood. Panel b) shows how the saturation current of the collector ($I_{\mathrm{cl}}^{\mathrm{max}}$) varies with V_{gr}. At first, the grid voltage suppresses the space-charge and consequently I_{cl} increases with increasing V_{gr} (1). After $V_{\mathrm{gr}} > 27.5\,\mathrm{V}$, the collector current decreases as the grid current tends to dominate (2). The laser used in these experiments has a wavelength of $\lambda = 1064\,\mathrm{nm}$ and used at 500 mW.

5.4 Summary and Outlook

While novel materials make new methods for electron emission feasible, the space-charge remains the major problem for energy conversion applications by thermionic emission. The results in this chapter demonstrate that the concept of thermoelectronic converters is applicable to PITE, which could solve the space-charge problem in these devices to a large extent. This compatibility is realized by the combination of ring magnets and block magnets on the magnetic yoke, together with a grid that has a large mesh size. The application of a transparent and conductive substrate allows the incident laser light to be perpendicular to the surface. Such a configuration is technologically important for practical applications, as in this geometry the complete surface area is available. Given the high current densities and the low light powers required, these converters may be a good candidate for stand-alone solar energy converters. In principle, these converters have the potential to compete with photovoltaic solar cells. However, several issues need to be solved to realize such converters.

The results in Sec. 5.3.2 suggest that the high temperatures of the heat traps damage the CNTs that contributes to the current decay in these devices. This could be improved by the evaporation of nanoparticles of a low work function material on the CNT-forests. Such a coating would allow the emission to start even at lower light power densities that could prevent the damage of the samples. LaB_6 ($\Phi_{WF}^{LaB_6} = 2.4\,eV$ to $3\,eV$) is a good candidate for this purpose. Besides, some reports suggest that the adhesion of LaB_6 on carbon-based materials tends to be stronger than on refractory metal substrates [111]. However, the effect of such coatings on the optical properties of the CNTs needs to be examined.

Another unresolved issue is the large voltage required for the band alignment in the conducted experiments. For this purpose, the electrical contacts between the nanotubes and the silicon substrate need to be studied. The Schottky barrier resulting at the interface of the native oxide layer of the Si substrate and the CNTs might affect the overall performance of these devices. Options like *in-situ* deposition of the CNTs on an etched silicon substrate,

or the *in-situ* deposition of silicon on a metallic substrate before the CVD growth could improve the device performance.

However, even by solving the issues mentioned above, a low work function collector material is still required to realize such energy converters. Assuming the literature values for the work functions of carbon nanotubes ($\Phi_{\mathrm{WF}}^{\mathrm{CNT}} \approx 4.5\,\mathrm{eV}$ [109]) and ITO ($\Phi_{\mathrm{WF}}^{\mathrm{ITO}} \approx 4.5\,\mathrm{eV}$ [112]), the output voltage of these devices is not sufficient for practical applications. As the results in Sec. 4.4 show, the deposition of oxide monolayers (*e.g.*, Y_2O_3 or BaO) on ITO could be used to tune its work function and to improve the overall device performance. Tuning the work function of ITO could have drastic impacts on the performance of photovoltaic devices in addition to PITE devices.

Alternatively, novel transparent conductive materials with a low work function could be employed as a collector. Recent reports suggest $SrVO_3$ and $CaVO_3$ outperforming the electrical properties of ITO and are transparent for a wide range of wavelengths [113]. Moreover, model calculations predict a work function of $<2\,\mathrm{eV}$ for a SrO terminated $SrVO_3$ [37]. Such properties are essential for realizing efficient energy converters.

Chapter 6

Summary

This thesis examines the work-function of novel material systems and illustrates how this essential material property can be tuned, and enhanced by atomically thin layers. These investigations are carried out *in-situ* by using state-of-the-art deposition techniques for heteroepitaxy and a custom-designed ultra-high vacuum measurement system, presented in Ch. 3.

The designed measurement system is based on the concept of thermoelectronic converters [3] that realize a space-charge free transport of thermally emitted electrons in a vacuum triode. The $I(V)$ characteristics of these devices are described here based on an ideal vacuum diode, formulated in Sec. 2.2. This formulation together with the employed data-analysis method illustrates a measurement accuracy of $<$100 meV. This precision is confirmed by the results of the "blind-tests" next to those of the LaB_6 thin films and the single crystal Nb:$SrTiO_3$ (0.1 wt. %) with a TiO_2 termination. The major advantage of such measurements is that they are conducted over large surface areas and provide unique qualitative information about the surface composition, in addition to the temperature behavior of materials.

The focus of this thesis is the work function of the cubic ABO_3 perovskites and their heterostructures. These materials offer a broad range of functionalities, but their work functions are relatively unexplored up to this point according to the literature. In Ch. 4 the work functions of the

ABO_3 perovskites are examined using epitaxial $SrRuO_3$ thin films as a model material, grown on Nb:$SrTiO_3$ substrates. The results show that the work function of $SrRuO_3$ thin films reduces by >17 % at elevated temperatures over time. These results suggest that surface relaxations and distortions cause this change of the work function. This understanding is in agreement with the model calculations performed by our collaborators Z. Zhong and P. Hansmann [37].

The key question that this thesis investigates is the tunability of the work function of materials by heteroepitaxy. This tunability is explored using one-unit-cell thick epitaxial monolayers of four different perovskites, deposited on $SrRuO_3$ thin films. These monolayers are $BaTiO_3$, $SrTiO_3$, $LaAlO_3$, and $BaZrO_3$. The deposition parameters of these capping layers were kept similar as possible in order to obtain qualitatively comparable results. The oxygen background pressure during the deposition of $SrRuO_3$ thin films and all capping layers was kept the same due to the sensitivity of $SrRuO_3$ on the variation of this parameter. The substrate temperature for the deposition of the capping layers was also set the same, and only the fluence of the ablation laser was optimized for their epitaxial growth. Hence, the deposition of the capping layers was performed on nominally similar $SrRuO_3$ thin films.

The results obtained for the heterostructures show that the work function of $SrRuO_3$ is tunable, *i.e.*, it decreases if $BaTiO_3$ and $SrTiO_3$ monolayers are grown on its surface, and increases with $BaZrO_3$ and $LaAlO_3$ monolayers. The most significant change is observed for the $LaAlO_3$ monolayer, which increases the work function of $SrRuO_3$ by +7.4 % for a relaxed surface, and by +23 % for an unrelaxed surface. This outcome shows that heterostructures with a tailored work function can be obtained in order to tune interfaces for desired functionalities, as required in photovoltaics or surfaces for catalytic purposes.

Furthermore, the results of the $BaTiO_3$, $SrTiO_3$, and $BaZrO_3$ monolayers on $SrRuO_3$ suggest a BO_2 termination in these heterostructures. $BaTiO_3$ and $SrTiO_3$ share the same transition metal on their B-site and both reduce the work function of $SrRuO_3$. However, $BaZrO_3$ shares the same A-ion with

$BaTiO_3$, but increases the work function of $SrRuO_3$. This observation is in agreement with the results of bare $SrRuO_3$ thin films, which suggests a BO_2 termination for these thin films. Therefore, the work function of ABO_3 perovskites and the modification of it strongly depends on the transition metal of the last layer. So far, the STEM analyses of interfaces in these heterostructures are ongoing to confirm this termination.

The measurements of the $BaTiO_3$ and $SrTiO_3$ monolayers on $SrRuO_3$ thin films show an additional work function value that seems to result from an incomplete surface coverage. This result is surprising as the obtained RHEED pattern after the deposition of these materials suggests a relatively smooth and homogeneous surface. Furthermore, the lattice mismatch of these capping layers with $SrRuO_3$ is smaller than the $LaAlO_3$ or $BaZrO_3$ capping layers, which did not show any additional work function. The STEM images of several unit cells of $BaTiO_3$ on $SrRuO_3$ suggest an island growth mode, *i.e.*, Stranski-Krastanov. Such a growth mode would result in an incomplete surface coverage for a one-unit-cell thick capping layer. This agreement between the work-function results and the STEM images illustrates that work function measurements can provide qualitative and detailed information about the surface structure, which may not be achieved by other characterization methods such as RHEED.

The photon-induced thermionic emission (PITE) characteristics of carbon-nanotube forests are investigated in Ch. 5. The correlation between the residual mass spectrum and the emission current suggests that the high temperatures of the "heat-traps" cause the current decay problem in these devices. These elevated temperatures result in the sublimation and degradation of carbon-nanotubes and consequently result in the decay of the emission current. Moreover, this chapter reports on the compatibility of PITE with the concept of thermoelectronic converters for space-charge suppression. This investigation is essential as the space-charge in conventional PITE devices is a major obstacle for realizing efficient energy converters.

In conclusion, the work function of perovskites are investigated in this thesis, and it is demonstrated how this essential material property can be

tailored using heteroepitaxy. The good agreement between the obtained results and the recent model calculations in the literature shows that the combination of atomically precise heteroepitaxy, in combination with the computational capabilities available today, opens new opportunities for materials and compounds with a "*tuned*" or an "*engineered*" work function. Still, more investigation is required to fully understand the characteristics of the work function of transition metal oxides, such as their reduction at elevated temperatures. Based on these results, surface-relaxation mechanisms significantly alter the work function of perovskites; thus, it is intriguing to investigate the effect of strain on the work function of these materials and thin films.

Behind the progress which has here been briefly pointed out, lies the work of many men. But we have seen that they all have one thing in common. A "red thread" connects them - the glowing filament.

O. W. Richardson, 1929 [114].

Bibliography

[1] J. C. Rivière, *Solid State Surface Science*, volume 1, chapter 4, p. 179, Dekker (New York) (1969)

[2] H. H. Lester, *The determination of the work function when an electron escapes from the surface of a hot body*, Phil. Mag., **31**, pp. 197 (1916)

[3] S. Meir, C. Stephanos, T. H. Geballe, and J. Mannhart, *Highly-efficient thermoelectronic conversion of solar energy and heat into electric power*, J. Renewable Sustainable Energy, **5**, 043127 (2013), DOI:10.1063/1.4817730

[4] A. Wehnelt, *Über den Austritt negativer Ionen aus glühenden Metallverbindungen und damit zusammenhängende Erscheinungen*, Ann. Phys., **319**, pp. 425 (1904), DOI:10.1002/andp.19043190802

[5] G. Gaertner and D. den Engelsen, *Hundred years anniversary of the oxide cathode–A historical review*, Appl. Surf. Sci., **251**, pp. 24 (2005), DOI:https://doi.org/10.1016/j.apsusc.2005.03.214

[6] D. S. Barratt, N. Filkin, and I. Bakker, *12.3: Oxide Plus - A Newly Developed Cathode for CRT Applications*, SID Symposium Digest of Technical Papers, **34**, pp. 162 (2003), DOI:10.1889/1.1832229

[7] N. D. Lang and W. Kohn, *Theory of Metal Surfaces: Work Function*, Phys. Rev. B, **3**, pp. 1215 (1971), DOI:10.1103/PhysRevB.3.1215

[8] N. D. Lang and W. Kohn, *Theory of Metal Surfaces: Charge Density and Surface Energy*, Phys. Rev. B, **1**, pp. 4555 (1970), DOI:10.1103/PhysRevB.1.4555

[9] L. Giordano, F. Cinquini, and G. Pacchioni, *Tuning the surface metal work function by deposition of ultrathin oxide films: Density functional calculations*, Phys. Rev. B, **73**, p. 045414 (2006), DOI:10.1103/PhysRevB.73.045414

[10] S. Prada, U. Martinez, and G. Pacchioni, *Work function changes induced by deposition of ultrathin dielectric films on metals: A theoretical analysis*, Phys. Rev. B, **78**, p. 235423 (2008), DOI:10.1103/PhysRevB.78.235423

[11] V. Vlahos, Y.-L. Lee, J. H. Booske, D. Morgan, L. Turek, M. Kirshner, R. Kowalczyk, and C. Wilsen, *Ab initio investigation of the surface properties of dispenser B-type and scandate thermionic emission cathodes*, Appl. Phys. Lett., **94**, 184102 (2009), DOI:10.1063/1.3129193

[12] C. G. Vayenas, S. Bebelis, and S. Ladas, *Dependence of catalytic rates on catalyst work function*, Nature, **343**, p. 625 (1990)

[13] S. M. Sze and K. K. Ng, *Physics of Semiconductor Devices, 3rd Edition*, Wiley-Interscience (2006), ISBN 978-0-471-14323-9

[14] G. N. Hatsopoulos and E. P. Gyftopoulos, *Thermionic Energy Conversion, Vol. 1*, The MIT Press (1973), ISBN 0262080591

[15] G. N. Hatsopoulos and E. P. Gyftopoulos, *Thermionic Energy Conversion, Vol. 2*, The MIT Press (1979), ISBN 0262080591

[16] R. Wanke, W. Voesch, I. Rastegar, A. Kyriazis, W. Braun, and J. Mannhart, *Thermoelectronic energy conversion: Concepts and materials*, MRS Bull., **42**, p. 518–524 (2017), DOI:10.1557/mrs.2017.140

[17] T. Susaki, A. Makishima, and H. Hosono, *Tunable work function in MgO/Nb:SrTiO₃ surfaces studied by Kelvin probe technique*, Phys. Rev. B, **83**, p. 115435 (2011), DOI:10.1103/PhysRevB.83.115435

[18] T. Tachikawa, H. Y. Hwang, and Y. Hikita, *Enhancing the barrier height in oxide Schottky junctions using interface dipoles*, Appl. Phys. Lett., **111**, p. 091602 (2017), DOI:10.1063/1.4991691

[19] C. Woltmann, *Oxidische FETs mit sub-100 nm Gatelänge*, Ph.D. thesis, Universität Stuttgart (2016), DOI:http://dx.doi.org/10.18419/opus-8881

[20] C. Woltmann, T. Harada, H. Boschker, V. Srot, P. A. van Aken, H. Klauk, and J. Mannhart, *Field-Effect Transistors with Submicrometer Gate Lengths Fabricated from LaAlO₃-SrTiO₃-Based Heterostructures*, Phys. Rev. Applied, **4**, p. 064003 (2015), DOI:10.1103/PhysRevApplied.4.064003

[21] R. W. G. Berktold, *Kapazitätsmessungen an Feldeffekttransistoren auf LaAlO₃-SrTiO₃-Basis*, Ph.D. thesis, University of Stuttgart (2017)

[22] H. J. Kim, U. Kim, T. H. Kim, J. Kim, H. M. Kim, B.-G. Jeon, W.-J. Lee, H. S. Mun, K. T. Hong, J. Yu, K. Char, and K. H. Kim, *Physical properties of transparent perovskite oxides (Ba,La)SnO₃ with high electrical mobility at room temperature*, Phys. Rev. B, **86**, p. 165205 (2012), DOI:10.1103/PhysRevB.86.165205

[23] S. Meir, *Highly-Efficient Thermoelectronic Conversion of Heat and Solar Radiation to Electric Power*, Ph.D. thesis, Universität Augsburg (2012)

[24] J. Hölzl, F. K. Schulte, and H. Wagner, *Solid Surface Physics*, volume 85 of *ISBN: 978-3-540-09266-7*, Springer Berlin Heidelberg (1979), DOI:10.1007/BFb0048918

[25] N. W. Ashcroft and N. D. Mermin, *Solid State Physics*, Brooks Cole (1976), ISBN 0030839939

[26] R. Smoluchowski, *Anisotropy of the Electronic Work Function of Metals*, Phys. Rev., **60**, pp. 661 (1941), DOI:10.1103/PhysRev.60.661

[27] B. Nieuwenhuys and W. Sachtler, *Crystal face specificity of nitrogen adsorption on a platium field emission tip*, Surf. Sci., **34**, pp. 317 (1973), DOI:10.1016/0039-6028(73)90121-0

[28] E. G. Derouane and A. A. Lucas, *Electronic Structure and Reactivity of Metal Surfaces*, Springer (1976), ISBN 0-306-35716-X, DOI:10.1007/978-1-4684-2796-7

[29] M. Salmerón, S. Ferrer, M. Jazzar, and G. A. Somorjai, *Photoelectron-spectroscopy study of the electronic structure of Au and Ag overlayers on Pt(100), Pt(111), and Pt(997) surfaces*, Phys. Rev. B, **28**, pp. 6758 (1983), DOI:10.1103/PhysRevB.28.6758

[30] N. E. Singh-Miller and N. Marzari, *Surface energies, work functions, and surface relaxations of low-index metallic surfaces from first principles*, Phys. Rev. B, **80**, p. 235407 (2009), DOI:10.1103/PhysRevB.80.235407

[31] R. Vanselow and X. Li, *The work function of kinked areas on clean, thermally rounded Pt and Rh crystallites: its dependence on the structure of terraces and edges*, Surf. Sci., **264**, pp. L200 (1992), DOI:10.1016/0039-6028(92)90154-X

[32] P. Franken and V. Ponec, *Ethylene adsorption on thin films of Ni, Pd, Pt, Cu, Au and Al; Work function measurements*, Surf. Sci., **53**, pp. 341 (1975), DOI:10.1016/0039-6028(75)90134-X

[33] H. B. Michaelson, *The work function of the elements and its periodicity*, J. Appl. Phys., **48**, pp. 4729 (1977), DOI:10.1063/1.323539

[34] R. G. Wilson, *Vacuum Thermionic Work Functions of Polycrystalline Be, Ti, Cr, Fe, Ni, Cu, Pt, and Type 304 Stainless Steel*, J. Appl. Phys., **37**, pp. 3170 (1966), DOI:10.1063/1.1703180

[35] J. P. Blewett, *The Properties of Oxide-Coated Cathodes. I*, J. Appl. Phys., **10**, pp. 668 (1939), DOI:10.1063/1.1707247

[36] J. M. Vaughn, C. Wan, K. D. Jamison, and M. E. Kordesch, *Thermionic electron emission microscopy of metal-oxide multilayers on tungsten*, IBM J. Res. Dev., **55**, pp. 14:1 (2011), DOI:10.1147/JRD.2011.2159423

[37] Z. Zhong and P. Hansmann, *Tuning the work function in transition metal oxides and their heterostructures*, Phys. Rev. B, **93**, p. 235116 (2016), DOI:10.1103/PhysRevB.93.235116

[38] R. Jacobs, J. Booske, and D. Morgan, *Understanding and Controlling the Work Function of Perovskite Oxides Using Density Functional Theory*, Adv. Funct. Mater., **26**, pp. 5471 (2016), DOI:10.1002/adfm.201600243

[39] A. Ohtomo and H. Y. Hwang, *A high-mobility electron gas at the LaAlO3/SrTiO3 heterointerface*, Nature, p. 423 (2004), DOI:10.1038/nature02308

[40] C. Herring and M. H. Nichols, *Thermionic Emission*, Rev. Mod. Phys., **21**, pp. 185 (1949), DOI:10.1103/RevModPhys.21.185

[41] A. Knapp, *Surface potentials and their measurement by the diode method*, Surf. Sci., **34**, pp. 289 (1973), DOI:10.1016/0039-6028(73)90120-9

[42] O. Richardson, *LI. Some applications of the electron theory of matter*, The London, Edinburgh, and Dublin Philosophical Magazine and Journal of Science, **23**, pp. 594 (1912), DOI:10.1080/14786440408637250

[43] S. Dushman, *Electron Emission from Metals as a Function of Temperature*, Phys. Rev., **21**, pp. 623 (1923), DOI:10.1103/PhysRev.21.623

[44] H. Shelton, *Thermionic Emission from a Planar Tantalum Crystal*, Phys. Rev., **107**, pp. 1553 (1957), DOI:10.1103/PhysRev.107.1553

[45] M. Chelvayohan and C. H. B. Mee, *Work function measurements on (110), (100) and (111) surfaces of silver*, J. Phys. C: Solid State Phys., **15**, p. 2305 (1982)

[46] K. A. Littau, K. Sahasrabuddhe, D. Barfield, H. Yuan, Z.-X. Shen, R. T. Howe, and N. A. Melosh, *Microbead-separated thermionic energy converter with enhanced emission current*, Phys. Chem. Chem. Phys., **15**, pp. 14442 (2013), DOI:10.1039/C3CP52895B

[47] H. Yuan, D. C. Riley, Z.-X. Shen, P. A. Pianetta, N. A. Melosh, and R. T. Howe, *Back-gated graphene anode for more efficient thermionic energy converters*, Nano Energy, **32**, pp. 67 (2017), DOI:10.1016/j.nanoen.2016.12.027

[48] Agilent Technologies, 5301 Stevens Creek Blvd., Santa Clara, CA 95051, United States

[49] W. Braun, *Applied RHEED-Reflection High-Energy Electron Diffraction During Crystal Growth*, Springer-Verlag Berlin Heidelberg (1999), ISBN 978-3-540-49485-0, DOI:10.1007/BFb0109548

[50] D. Holmes, J. Sudijono, C. McConville, T. Jones, and B. Joyce, *Direct evidence for the step density model in the initial stages of the layer-by-layer homoepitaxial growth of GaAs(111)A*, Surf. Sci., **370**, pp. L173 (1997), DOI:10.1016/S0039-6028(96)01173-9

[51] S. Clarke and D. D. Vvedensky, *Origin of Reflection High-Energy Electron-Diffraction Intensity Oscillations during Molecular-Beam Epitaxy: A Computational Modeling Approach*, Phys. Rev. Lett., **58**, pp. 2235 (1987), DOI:10.1103/PhysRevLett.58.2235

[52] G. J. H. M. Rijnders, G. Koster, D. H. A. Blank, and H. Rogalla, *In situ monitoring during pulsed laser deposition of complex oxides using reflection high energy electron diffraction under high oxygen pressure*, Appl. Phys. Lett., **70**, pp. 1888 (1997), DOI:10.1063/1.118687

[53] Parametric Technology GmbH, Edisonstraße 8, 85716 Unterschleißheim, Germany

[54] VAb Vakuum-Anlagenbau GmbH, Marie-Curie-Straße, 11 25337 Elmshorn, Germany

[55] WHS Sondermetalle e.K., Industriepark ob der Tauber, 97947 Grünsfeld, Germany

[56] Schneider Electric Systems Germany GmbH, Ottostraße 1, 65549 Limburg an der Lahn, Germany

[57] CVT GmbH & Co. KG, Romantische Straße 18, 87642 Halblech, Germany

[58] M. Hirayama and K. Shohno, *CVD-BN for Boron Diffusion in Si and Its Application to Si Devices*, J. Electrochem. Soc., **122**, pp. 1671 (1975), DOI:10.1149/1.2134107

[59] S. S. Dana and J. R. Maldonado, *Low pressure chemical vapor deposition boro-hydro-nitride films and their use in x-ray masks*, Journal of Vacuum Science & Technology B: Microelectronics Processing and Phenomena, **4**, pp. 235 (1986), DOI:10.1116/1.583447

[60] A. W. Moore, *Characterization of pyrolytic boron nitride for semiconductor materials processing*, J. Cryst. Growth, **106**, pp. 6 (1990), DOI:10.1016/0022-0248(90)90281-O

[61] D. M. Hoffman, G. L. Doll, and P. C. Eklund, *Optical properties of pyrolytic boron nitride in the energy range 0.05-10 eV*, Phys. Rev. B, **30**, pp. 6051 (1984), DOI:10.1103/PhysRevB.30.6051

[62] T. Takahashi, H. Itoh, and A. Takeuchi, *Chemical vapor deposition of hexagonal boron nitride thick film on iron*, J. Cryst. Growth, **47**, pp. 245 (1979), DOI:10.1016/0022-0248(79)90248-3

[63] Haynes International, Inc., Global Heaquarters, 1020 West Park Avenue, P.O. Box 9013, Kokomo, Indiana 46904-9013, USA

[64] L. C. Hale and A. H. Slocum, *Optimal design techniques for kinematic couplings*, Precis. Eng., **25**, pp. 114 (2001), DOI:10.1016/S0141-6359(00)00066-0

[65] IBS Magnet, Kurfürstenstraße 92D, 12105 Berlin (Mariendorf), Germany

[66] D. C. Meeker, Finite Element Method Magnetics, Version 4.2. url: http://www.femm.info

[67] Tektronix Inc., 14150 SW Karl Braun Drive, P.O. Box 500 Beaverton, OR 97077, USA

[68] W. Dobrygin, *Ion-Radical Synergism during Etching in an Ar/O_2 Inductively Coupled Plasma: Consequences for Biological Decontamination Applications*, Master's thesis, University of Bochum (2009)

[69] R. S. John R. Howell, M. Pinar Menguc, *Thermal radiation heat transfer*, CRC Press, Taylor & Francis Group (2015), ISBN 9781466593268

[70] R. Finn, D. Nicholson, and J. Trischka, *Thermionic constants and electron reflection for Ta (100) by the shelton retarding field method*, Surf. Sci., **34**, pp. 522 (1973), DOI:10.1016/0039-6028(73)90023-X

[71] D. J. Kim, J. Xia, and Z. Fisk, *Topological surface state in the Kondo insulator samarium hexaboride*, Nat. Mater., **13**, p. 466 (2014), DOI:10.1038/nmat3913

[72] Z. Wu, D. J. Singh, and R. E. Cohen, *Electronic structure of calcium hexaboride within the weighted density approximation*, Phys. Rev. B, **69**, p. 193105 (2004), DOI:10.1103/PhysRevB.69.193105

[73] H. J. Tromp, P. van Gelderen, P. J. Kelly, G. Brocks, and P. A. Bobbert, *CaB_6: A New Semiconducting Material for Spin Electronics*, Phys. Rev. Lett., **87**, p. 016401 (2001), DOI:10.1103/PhysRevLett.87.016401

[74] M. Futamoto, M. Nakazawa, and U. Kawabe, *Thermionic emission properties of hexaborides*, Surf. Sci., **100**, p. 470 (1980), DOI:10.1016/0039-6028(80)90416-1

[75] S. Zhou, J. Zhang, D. Liu, Q. Hu, and Q. Huang, *The effect of samarium doping on structure and enhanced thermionic emission properties of lanthanum hexaboride fabricated by spark plasma sintering*, physica status solidi (a), **211**, pp. 555 (2014), DOI:10.1002/pssa.201330152

[76] M. M. Hasan, *Synthesis and Thermionic Properties of Oxide-Tungsten Composites and Boride Materials for Solar Thermionic Energy Conversion*, Ph.D. thesis, The University of Newcastle-Australia (2015)

[77] M. Hasan, D. Cuskelly, H. Sugo, and E. Kisi, *Low temperature synthesis of low thermionic work function ($La_xBa_{1-x}B_6$)*, J. Alloys Compd., **636**, p. 67 (2015), DOI:10.1016/j.jallcom.2015.02.105

[78] H. Liu, X. Zhang, S. Ning, Y. Xiao, and J. Zhang, *The electronic structure and work functions of single crystal LaB_6 typical crystal surfaces*, Vacuum, **143**, pp. 245 (2017), DOI:10.1016/j.vacuum.2017.06.029

[79] V. Craciun and D. Craciun, *Pulsed laser deposition of crystalline LaB_6 thin films*, Appl. Surf. Sci., **247**, p. 384 (2005), DOI:10.1016/j.apsusc.2005.01.071 , proceedings of the European Materials Research Society 2004

[80] C. Oshima, E. Bannai, T. Tanaka, and S. Kawai, *Thermionic work function of LaB_6 single crystals and their surfaces*, J. Appl. Phys., **48**, pp. 3925 (1977), DOI:10.1063/1.324266

[81] R. Nishitani, M. Aono, T. Tanaka, C. Oshima, S. Kawai, H. Iwasaki, and S. Nakamura, *Surface structures and work functions of the LaB_6 (100), (110) and (111) clean surfaces*, Surf. Sci., **93**, p. 535 (1980), DOI:10.1016/0039-6028(80)90281-2

[82] M. A. Uijttewaal, G. A. de Wijs, and R. A. de Groot, *Ab Initio and Work Function and Surface Energy Anisotropy of LaB_6*, The Journal of

Physical Chemistry B, **110**, pp. 18459 (2006), DOI:10.1021/jp063347i

[83] J. F. Schooley, W. R. Hosler, and M. L. Cohen, *Superconductivity in Semiconducting $SrTiO_3$*, Phys. Rev. Lett., **12**, pp. 474 (1964), DOI:10.1103/PhysRevLett.12.474

[84] Y. Hikita, Y. Kozuka, T. Susaki, H. Takagi, and H. Y. Hwang, *Characterization of the Schottky barrier in $SrRuO_3$/Nb:$SrTiO_3$ junctions*, Appl. Phys. Lett., **90**, p. 143507 (2007), DOI:10.1063/1.2719157

[85] M. Kawasaki, K. Takahashi, T. Maeda, R. Tsuchiya, M. Shinohara, O. Ishiyama, T. Yonezawa, M. Yoshimoto, and H. Koinuma, *Atomic Control of the SrTiO3 Crystal Surface*, Science, **266**, pp. 1540 (1994), DOI:10.1126/science.266.5190.1540

[86] H. Schraknepper, C. Bäumer, F. Gunkel, R. Dittmann, and R. A. D. Souza, *Pulsed laser deposition of $SrRuO_3$ thin-films: The role of the pulse repetition rate*, APL Mater., **4**, p. 126109 (2016), DOI:10.1063/1.4972996

[87] G. Rijnders, D. H. A. Blank, J. Choi, and C.-B. Eom, *Enhanced surface diffusion through termination conversion during epitaxial $SrRuO_3$ growth*, Appl. Phys. Lett., **84**, pp. 505 (2004), DOI:10.1063/1.1640472

[88] C. Ares Fang and C. Maloney, *The effect of substrate work function on work function reduction of Re/W alloy-coated impregnated cathodes*, Appl. Phys. A, **50**, pp. 603 (1990), DOI:10.1007/BF00323454

[89] A. Verma and V. Jindal, *Lattice constant of cubic perovskites*, J. Alloys Compd., **485**, pp. 514 (2009), DOI:10.1016/j.jallcom.2009.06.001

[90] JEOL Ltd., 3-1-2 Musashino, Akishima, Tokyo 196-8558, Japan.

[91] CEOS GmbH Englerstr. 28 D-69126 Heidelberg,

[92] R. Schafranek, S. Payan, M. Maglione, and A. Klein, *Barrier height at (Ba,Sr)TiO_3/Pt interfaces studied by photoemission*, Phys. Rev. B, **77**, p. 195310 (2008), DOI:10.1103/PhysRevB.77.195310

[93] G. Comsa, A. Gelberg, and B. Iosifescu, *Temperature Dependence of the Work Function of Metals (Mo,Ni)*, Phys. Rev., **122**, pp. 1091 (1961), DOI:10.1103/PhysRev.122.1091

[94] L. C. Burton, *Temperature dependence of the silicon work function by means of a retarding potential technique*, J. Appl. Phys., **47**, pp. 1189 (1976), DOI:10.1063/1.322703

[95] J. W. Schwede, I. Bargatin, D. C. Riley, B. E. Hardin, S. J. Rosenthal, Y. Sun, F. Schmitt, P. Pianetta, R. T. Howe, Z.-X. Shen, and N. A. Melosh, *Photon-enhanced thermionic emission for solar concentrator systems*, Nat. Mater., **9**, pp. 762 (2010), DOI:10.1038/nmat2814

[96] P. Yaghoobi, M. V. Moghaddam, and A. Nojeh, *"Heat-trap": Light-induced localized heating and thermionic electron emission from carbon nanotube arrays*, Solid State Commun., **151**, pp. 1105 (2011), DOI:10.1016/j.ssc.2011.05.024

[97] Department of Electrical and Computer Engineering, The University of British Columbia, Vancouver, BC Canada. url: http://nanostructure.ece.ubc.ca

[98] A. H. Khoshaman, H. D. E. Fan, A. T. Koch, G. A. Sawatzky, and A. Nojeh, *Thermionics, Thermoelectrics, and Nanotechnology: New Possibilities for Old Ideas*, IEEE Nanotechnol. Mag., **8**, pp. 4 (2014), DOI:10.1109/MNANO.2014.2313172

[99] A. Lekawa-Raus, J. Patmore, L. Kurzepa, J. Bulmer, and K. Koziol, *Electrical Properties of Carbon Nanotube Based Fibers and Their Future Use in Electrical Wiring*, Adv. Funct. Mater., **24**, pp. 3661 (2014), DOI:10.1002/adfm.201303716

[100] J. Hone, M. Llaguno, M. Biercuk, A. Johnson, B. Batlogg, Z. Benes, and J. Fischer, *Thermal properties of carbon nanotubes and nanotube-based materials*, Appl. Phys. A, **74**, pp. 339 (2002), DOI:10.1007/s003390201277

[101] V. Lee, C.-H. Wu, Z.-X. Lou, W.-L. Lee, and C.-W. Chang, *Divergent and Ultrahigh Thermal Conductivity in Millimeter-Long Nanotubes*, Phys. Rev. Lett., **118**, p. 135901 (2017), DOI:10.1103/PhysRevLett.118.135901

[102] H. Shi, J. G. Ok, H. W. Baac, and L. J. Guo, *Low density carbon nanotube forest as an index-matched and near perfect absorption coating*, Appl. Phys. Lett., **99**, p. 211103 (2011), DOI:10.1063/1.3663873

[103] T. Saleh, M. V. Moghaddam, M. S. M. Ali, M. Dahmardeh, C. A. Foell, A. Nojeh, and K. Takahata, *Transforming carbon nanotube forest from darkest absorber to reflective mirror*, Appl. Phys. Lett., **101**, p. 061913 (2012), DOI:10.1063/1.4744429

[104] P. Yaghoobi, M. V. Moghaddam, and A. Nojeh, *Increasing the current density of light-induced thermionic electron emission from carbon nanotube arrays*, in *24th International Vacuum Nanoelectronics Conference* (2011)

[105] K. Voon, K. Dridi, M. Chowdhury, M. Chang, and A. Nojeh, *The role of carbon nanotube forest density in thermionic emission*, in *2016 29th International Vacuum Nanoelectronics Conference (IVNC)*, pp. 1–2 (2016), DOI:10.1109/IVNC.2016.7551493

[106] H. Kim, C. M. Gilmore, A. Piqué, J. S. Horwitz, H. Mattoussi, H. Murata, Z. H. Kafafi, and D. B. Chrisey, *Electrical, optical, and structural properties of indium-tin-oxide thin films for organic light-emitting devices*, J. Appl. Phys., **86**, pp. 6451 (1999), DOI:10.1063/1.371708

[107] Laserglow Technologies, 873 St. Clair Ave. West, Toronto, Canada.

[108] Thorlabs Inc., 56 Sparta Avenue Newton, New Jersey 07860, USA.

[109] H. Ago, T. Kugler, F. Cacialli, W. R. Salaneck, M. S. P. Shaffer, A. H. Windle, and R. H. Friend, *Work Functions and Surface Functional Groups of Multiwall Carbon Nanotubes*, The Journal of Physical Chemistry B, **103**, pp. 8116 (1999), DOI:10.1021/jp991659y

[110] R. E. Honig, *Vapor Pressure Data for the More Common Elements*, RCA Review, **18**, pp. 195 (1957)

[111] C. M. Zimmer, *Nanostrukturierter Photoelektronenemitter auf LaB_6-Basis für atmosphärische Ionisations-Gassensorik*, Ph.D. thesis, Ruhr-Universität Bochum, Germany (2011)

[112] Y. Park, V. Choong, Y. Gao, B. R. Hsieh, and C. W. Tang, *Work function of indium tin oxide transparent conductor measured by photoelectron spectroscopy*, Appl. Phys. Lett., **68**, pp. 2699 (1996), DOI:10.1063/1.116313

[113] L. Zhang, Y. Zhou, L. Guo, W. Zhao, A. Barnes, H.-T. Zhang, C. Eaton, Y. Zheng, M. Brahlek, H. F. Haneef, N. J. Podraza, M. W. Chan, V. Gopalan, K. M. Rabe, and R. Engel-Herbert, *Correlated metals as transparent conductors*, Nat. Mater., **15**, p. 204 (2015), DOI:10.1038/nmat4493

[114] "The Nobel Prize in Physics 1928". Nobelprize.org. Nobel Media AB 2014. Web. 7 Feb 2018. http://www.nobelprize.org/nobel_prizes/physics/laureates/1928/

Acknowledgments

The work presented in this thesis could only be accomplished by the friendly atmosphere and the support of the entire staff of the Max Planck Institute in Stuttgart. The hard work of the mechanical workshop (Thomas Frey), the precision in making the sapphire components by the glass workshop (Helmut Kammerlander), the support of the electrical workshop (Alex Kunschikow), and many others who made it possible to realize this work. This list is indeed endless, so thank you all!

I would like to thank Prof. Dr. Mannhart for allowing me to be part of his group and for trusting me with this project. During this time, I have been continuously inspired by you.

I thank Prof. Dr. Jörg Wrachtrup and Prof. Hans P. Büchler for accepting to be part of my examination committee. The straightforward process and great communications made the final step much relaxed and comfortable.

Lieber Manfred, Ingo, Konrad, Sabine! Vielen Dank für eure ehrliche und unkomplizierte zusammen Arbeit. Eure Unterstützungen und Verständnis werde ich nie vergessen.

Philipp Hansmann and Zhicheng Zhong, thank you for the great discussions and the valuable inputs. Your friendly attitude made our collaboration just great!

Dear Prof. Nojeh, thank you for the inspiring collaboration, fruitful discussions and the motivation you gave me.

Prof. Mydosh! Thank you so much for your scientific input and the exciting discussions. These have widened my vision and kept me motivated the entire time!

I thank Dr. K. Kreuer for his efforts and his caring attitude as my external supervisor.

A special thanks goes to my "Thermo-Kollegen". Dr. Wolfgang Braun, Robin Wanke and Wolfgang III.
I hope your filaments are always glowing ;).

My friends, Carsten Woltmann, and René Berktold thank you very much for all the good times. You have always been there for me and believed in me. Angellos, thank you for the countless beer sessions mate `#Maulwurf`. Robin, you are truly the best guy of Swabia `#Käsespätzle`. Ali, die frische luft ruft! Pascal, `#Lavashak`, `#Fesenjan`. Prosper! Thank you for the daily smile `#HappyPeople`. Kevin V., `#Ducks #Milan`. Alex, `#TheLightIsNotBroken`. `#Cheers All!`

Rotraut, I have learned so much from you during my master thesis.
Thank you for preparing me!

I would like to thank the University of Stuttgart, for giving me the admission and chance to participate in international M. Sc. Program.
Eva Rose thank you for fantastically coordinating the program.

In the end, I want to thank Wolfgang Winter for helping me out on numerous occasions, Sarah Parks for her helpful attitude and all other members of the Mannhart group. Especially Renate Zimmermann for her great support and suggestions.

Declaration

I certify that the work presented in this thesis is, to the best of my knowledge and belief, original and contains no material previously published or written by another person, except where due references are made. The reprinted, and/or replotted figures are done with the permission of the corresponding journal.

Ich bestätige, dass die in dieser Dissertation vorgestellte Arbeit nach bestem Wissen und Gewissen original und authentisch ist und kein Material enthält, das zuvor von einer anderen Person veröffentlicht oder geschrieben wurde, es sei denn, es wurden entsprechende Referenzen gemacht. Die nachgedruckten Figuren wurden mit der Genehmigung der entsprechenden Zeitschrift erstellt.

Iman Rastegar Alam
Stuttgart, Germany